universität wien

DIPLOMARBEIT / DIPLOMA THESIS

Titel der Diplomarbeit / Title of the Diploma Thesis

„Towards Single-Site Photocatalysis: Design of Non-Noble-Metal-Based Systems for Water Splitting Reactions“

verfasst von / submitted by

Pablo Rony Alberto Ayala Leiva, BSc

angestrebter akademischer Grad / in partial fulfilment of the requirements for the degree of

Diplom-Ingenieur (Dipl.-Ing.)

Wien, 2020 / Vienna, 2020

Studienkennzahl lt. Studienblatt / degree programme code as it appears on the student record sheet:	A 066 658
Studienrichtung lt. Studienblatt / degree programme as it appears on the student record sheet:	Masterstudium Chemie und Technologie der Materialien UG2002
Betreut von / Supervisor:	Univ.Prof. Mag.rer.nat. Dr.rer.nat. Dominik Eder
Mitbetreut von / Co-Supervisor:	Univ.Ass. Dr.rer.nat. Alexey Cherevan

Dedicated to my loving parents

Abstract

Due to the world's current energy crisis and the inevitable depletion of fossil fuels, finding alternative energy sources has become ever more important. Photocatalysis, also known as artificial photosynthesis, allows the transformation of solar to chemical energy by facilitating non-spontaneous chemical reactions with the aid of light irradiation and a photocatalyst. Through photocatalysis, the sun's energy – an inexhaustible energy source – can be stored in the chemical bonds of so-called "solar fuels" (e.g. hydrogen or hydrocarbons) by means of water splitting or CO_2 reduction reactions, respectively. However, after 60 years of targeted research, real-world applications of heterogeneous photocatalysis are still limited by the insufficient efficiency and predictability of contemporary catalytic systems.

Heterogenous single-metal-site catalysts (HSMSCs) feature many advantages over their bulkier counterparts as a result of their ability to bridge the qualities of homo- and heterogeneous catalysis. When relying on the concept of HSMSCs, maximized atom utilization efficiency and accessibility of the active sites renders excellent catalytic performances (homogeneous trait), while stability and recyclability stay preserved (heterogeneous trait).

Applying HSMSCs in photocatalysis is a rather novel approach, especially considering earth-abundant co-catalysts, which are still underexplored. Besides, the use of HSMSCs allows to construct more unique and selective co-catalysts to address the challenges of complex multielectron catalytic reactions. Moreover, applying the single-site concept to noble metals – which show superior catalytic activities but are scarce in the earth's crust – could make their implementation more feasible for large-scale applications.

In this Thesis we synthesize heterogeneous single-metal-site photocatalysts following the "isolation strategy" through an adsorption-limited wet impregnation process by using TiO_2 as model support and earth-abundant (Cu and Ni) and noble (Pt and Au) metals as co-catalysts. The catalysts are characterized by IR and UV-vis spectroscopy for qualitative analysis, TXRF for determination of the real loadings of the active species, and TEM for resolving the atomic structure and morphology of the samples. We investigate the different adsorption/deposition behaviors of the precursor species on the support and the influence of light during synthesis. Noble metals undergo photodeposition to form nanoparticles under ambient-light, whereas earth-abundant metals rather stay as complexed species on the substrate's surface. To further promote the formation and stabilization of single-site species, we modify the support's surface with PO_4 groups. The resulting PO_4/TiO_2 shows enhanced adsorption of metal precursors and stronger structural changes in the co-catalyst species thus confirming a crucial role of the surface charge and chemistry on the single-site stabilization.

Furthermore, we evaluate the performance of our photocatalysts through photocatalytic hydrogen evolution reaction (HER) experiments and discuss the obtained activity trends (in terms of H_2 evolution rates and turnover frequency values) in light of different mathematical models. All investigated photocatalysts consistently follow our non-linear model upon decreasing the loadings, which speaks for an alteration in the co-catalyst's size/morphology towards smaller, perhaps even single-site-like species. When using the modified PO_4/TiO_2 substrate, the activity trend of Pt > Au > Cu > Ni gets less pronounced, and the best-performing earth-abundant systems based on Cu become comparable to the Au-based samples. Finally, we demonstrate that the activity trend – when normalized per cost of precursor – gets inverted, hence, suggesting that earth-abundant co-catalysts could open up new frontiers for practical applications.

Table of Content

1. Abbreviations

Ac…… Acetate
AcAc……..……Acetylacetonate
ALD…… Atomic layer deposition
ATR-FTIR…….…... Attenuated total reflection Fourier-transformed infrared spectroscopy
CB……Conduction band
CO…… Carbon monoxide
CO_2…….... Carbon dioxide
DFT…… Density functional theory
DI water…… Distilled water
DRS……..…Diffuse reflectance spectroscopy
e^-……..……..……. Electron
E_g……..…….. Bandgap Energy
g-C_3N_4…… Graphitic carbon nitride
GHG……... Greenhouse gas
GO…… Graphene oxide
h^+……... Hole
H_2……..…. Hydrogen
HER…….. Hydrogen Evolution Reaction
HSMSC…….. Heterogeneous single-metal-site catalyst
MeOH……..…… Methanol
MOF…….. Metal organic framework
NP…….. Nanoparticle
OER…… Oxygen evolution reaction
PC……..…... Photocatalysis
PD……..……... Photodeposition
PO_4…… Phosphate
PV……... Photovoltaic
RT……..…. Room temperature
SA…….. Surface area
SAC……..… Single-atom catalyst
SMR……... Steam methane reforming
SPR……..… Surface plasmon resonance
SS…….. Single-site
TEM……...Transmission electron microscopy
TiO_2……..…….. Titania (anatase)
TOF……Turnover frequency
TON……Turnover number
TXRF……..……..Total reflection X-ray fluorescence spectroscopy
VB…… Valence band
wt.% …….. Weight percent

2. Introduction

2.1. Energy and Environment

Humankind is facing one of the greatest challenges of its modern age: meeting the world´s growing energy needs through clean, affordable and renewable sources.[1,2] Currently, over 80 % of the world's primary energy sources are derived from non-renewable fossil fuels, including oil (32 %), coal (27 %) and natural gas (22 %), which are the by-products of eons of photosynthesis and are being depleted at an unsustainable pace. Their combustion results in increased carbon dioxide (CO_2) concentrations in the atmosphere, which is the main greenhouse gas (GHG) and contributes greatly to global warming and ocean acidification.[3,4] In 2018, the global primary energy demand rose by 2.9 %, while CO_2 emissions from energy use incremented by 2.0 %. These accelerated growth-rates have been the fastest since 2010, with an alarming and contradictory pace, considering the transition towards low-carbon energy systems envisioned by the Paris Agreement climate goals signed in 2016.[2,5–7]

In this regard, hydrogen (H_2) has brought the attention of the scientific community as a potential solution for replacing fossil fuels and developing future, environmentally friendly and sustainable energy systems. H_2 is considered to be the cleanest and most effective energy fuel, as it has an energy density of 142 MJ kg^{-1} (the largest amount of energy per unit weight) and renders solely heat and water upon combustion in air, avoiding undesired GHGs. Moreover, H_2 – with developed storage and delivery technologies – could serve as an alternative energy-carrier molecule for renewable technologies based on intermittent resources including wind, solar or bioenergy. However, H_2 is still largely generated through methods that rely on fossil fuels (steam-reforming) or high amounts of electricity (electrolysis) which ultimately is detrimental to the environment. In order to break this vicious cycle, novel methods for H_2 generation need to be further developed and implemented worldwide.[7,8]

2.2. Hydrogen economy

Due to hydrogen's potential of becoming the next generation energy carrier, the term "hydrogen economy" has arisen. It describes an integral system, which comprises the production of H_2 through different and renewable sources, its efficient storage/distribution and, ultimately, its end-use applications and recycling.[9–11]

2.2.1. H_2 production from fossil fuels

About 96 % of global hydrogen production relies on fossil fuels. The main industrial processes are steam and oil reforming – based on natural gas and lighter oils (e.g. naphtha), respectively – as well as coal gasification. The most commonly used among these is steam methane reforming (SMR), a two-step catalytic process, in which methane and water steam react to a mixture of hydrogen, carbon dioxide and carbon monoxide (CO), following the reactions:

$$CH_4 + H_2O \rightarrow CO + 3H_2 \qquad \Delta H_{298} = 206\ kJ\ mol^{-1} \quad \textbf{(1)}$$

$$CO + H_2O \rightarrow CO_2 + H_2 \qquad \Delta H_{298} = -41\ kJ\ mol^{-1} \quad \textbf{(2)}$$

The endothermic reaction **(1)** requires elevated temperatures, pressure, and nickel-based catalysts to overcome the energy barrier. The second step **(2)**, known as the water-gas shift

reaction (WGSR), requires a deliberate temperature regulation. Finally, high-purity H_2 is obtained by separating considerable amounts of CO and CO_2.[7–11]

Oil reforming works similarly, but uses higher hydrocarbons than methane, like naphtha, containing a mixture of compounds having 5 to 12 carbon atoms in the backbone. The last-mentioned process uses coal as a feedstock, a cheap and abundant fossil fuel that plays an important role in the H_2 industry. This process converts coal, oxygen and steam at elevated temperatures into CO, H_2 and, in smaller amounts, CO_2, methane and other compounds. The equilibrium of the WGSR plays an important role as well, defining the concentrations of the gas phase constituents in the gasifier.[12,13] The process can be represented as follows:

$$C + \frac{1}{2}O_2 \rightarrow CO \quad \textbf{(3)}$$

$$C + H_2O \rightarrow CO + H_2 \quad \textbf{(4)}$$

All these methods show major drawbacks, as they use finite and non-renewable sources, which also need to be purified beforehand to avoid catalyst poisoning. Complex engineering techniques for controlling the WGSR as well as the synthesis gas (CO + H_2) composition are needed as well. On top, considerable emissions of CO_2 controvert a sustainable H_2 economy, which is why alternative green solutions are being looked for.

2.2.2. H_2 production from renewable sources

It is of little environmental benefit to shift towards a hydrogen economy without the decarbonization of its sources. The potential in H_2 relies on a cycle in which renewable energy is implemented for its production. Renewable energies are defined as the ones derived from inexhaustible resources that are able to be constantly replenished on a human timescale, e.g. wind, geothermal, biomass, solar energy, etc.[14] Each of these primary energy sources has further routes towards H_2 production.

Biomass, such as plants or animal wastes, are very versatile sources in nature that are used for H_2 generation through thermochemical or biological processes. The most promising processes are pyrolysis and gasification, which work similarly to coal gasification. Using elevated temperatures, biomass is converted into liquid oils, charcoal or gaseous compounds, which are subsequently steam-reformed or further processed to obtain H_2, as previously described in **Section 2.2.1**. It must be noted, that H_2 purification from other produced gases and CO_2 fixation technologies have to be considered as well. Biomass-derived techniques are economically viable and will become competitive with the conventional steam-reforming for H_2 production in the near future.[15]

Wind energy is able to generate electricity without using any fuel by transforming mechanical energy from a rotating turbine into electrical power. Electrolysis of water via wind energy, or any other renewable electricity source, has a high economic potential for the water splitting reaction. In this important process, a high voltage is applied to an electrochemical cell containing water and an electrolyte, liberating hydrogen and oxygen (O_2), described by the following endothermic reaction:

$$H_2O \rightarrow H_2 + \frac{1}{2}O_2 \qquad \Delta H_{298} = 286\ kJ\ mol^{-1} \quad \textbf{(5)}$$

This thermodynamically non-spontaneous reaction is performed when enough energy is supplied to the cell in the form of electricity. The main advantage of electrolysis is that H_2 and O_2 can be obtained individually and without reacting with each other since the half-reactions take place on the anode and cathode that can be spatially separated. In acidic conditions, water is oxidized to O_2 at the anode and protons are reduced to H_2 at the cathode.[16] Similarly, any renewable source of energy which can be converted to electricity can be coupled with the electrolysis process.

(+) Anode: $$H_2O \rightarrow \frac{1}{2}O_2 + 2H^+ + 2e^- \quad \textbf{(6)}$$

(-) Cathode: $$2H^+ + 2e^- \rightarrow H_2 \quad \textbf{(7)}$$

In this regard, solar energy presents an inexhaustible, free and clean energy source, which is employed to generate hydrogen through three main pathways: photovoltaic (PV) cells, thermochemical routes and artificial photosynthesis.

Firstly, PV cells, commonly known as solar cells, are designed to convert the sun's energy directly into electricity. A light-absorbing material in the PV cell, often high purity silicon, is able to absorb light and create free charge carriers. The photo-generated electrons and holes are then separated at a p-n junction and further driven by other cell components resulting in the creation of a certain voltage (i.e. photovoltaic effect), which is then used to drive an electrical current through an external circuit. This electricity can subsequently be coupled with electrolysis cells, thus creating hybrid energy-producing and storing systems.[17] Although simple in design, rather low-maintenance and efficient, the market of PV cells is still restrained due to the expensive materials and complex manufacturing processes.[18]

Secondly, solar water thermolysis to produce H_2 bases its principles on concentrating the sun's heat and using it to make the thermal decomposition of water possible. To increase the dissociation degree of this endothermic reaction **(5)**, very high temperatures, low pressures and eventually a catalyst are employed. This one-step process usually results in a mixture of H_2 and O_2, which needs to be separated using complex techniques. Further drawbacks of this technology are the need for sophisticated solar components and heat-resistant materials, as well as the fundamental limitations posed by the process thermodynamics.[19]

Lastly, artificial photosynthesis, also known as photocatalysis (PC), is an important and direct method for H_2 production aided by light and a catalyst. Being central to this work, the term will be described in the following section in detail.

2.3. Photocatalysis and its challenges

Photocatalysis is defined as a chemical reaction aided by light irradiation in the presence of a special kind of catalyst, a photocatalyst, which allows the direct transformation of light to chemical energy, eventually stored in the form of chemical bonds of the so-called solar fuels and commodity chemicals. A similar process is well-known in plants: they transform water and CO_2 into carbohydrates using the sun's irradiation energy and the assistance of chlorophyll – the natural photocatalyst employed in this case. Inspired by the natural photosynthesis, the term "artificial photosynthesis" has arisen, in which man-made, semiconductor-based photocatalysts are employed to drive a plethora of chemical reactions. To date, PC has successfully been applied for H_2 production from water splitting, CO_2 reduction and pollutant degradation.[13,20,21]

The working principle of heterogeneous photocatalysis can be summarized in three steps: *i)* a semiconductor absorbs light of an energy greater than the semiconductor's bandgap, thus exciting electrons from the valence band (VB) to the conduction band (CB) and producing an electron (e^-)-hole (h^+) pair, *ii)* these charge carriers get separated and migrate to the surface of the semiconductor, and *iii)* they reduce (e^-) or oxidize (h^+) a chemical species at the surface of the catalyst. In the case of water splitting, water gets oxidized by the holes to generate O_2 and protons (H^+) get reduced by the electrons to produce H_2, as shown in **Figure 1**. First reported in 1972, water splitting through photo(electro-)catalysis became an attractive topic of research: sunlight is an abundant, clean and renewable energy resource; water is available at vast amounts. However, the design and development of efficient photocatalysts face many challenges still today. These difficulties stem from two main factors: fundamental thermodynamics and reaction kinetics. [7,22,23]

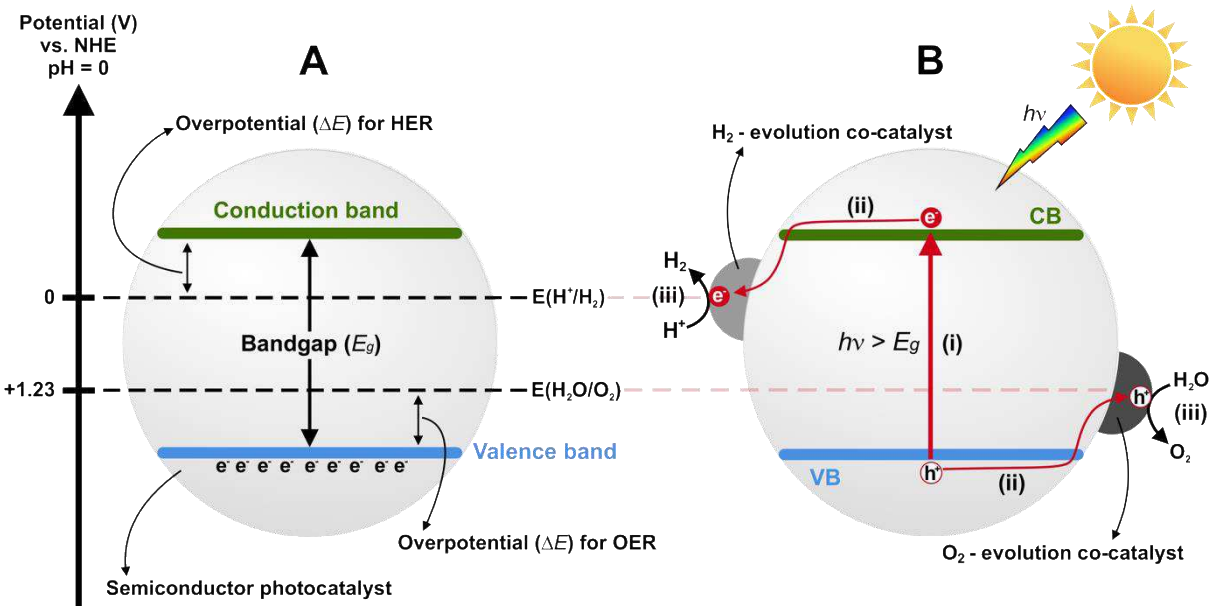

Figure 1 | **A,** Principle of photocatalytic water splitting over a semiconductor photocatalyst, adapted from Li et al.[24] **B,** Schematic illustration of photocatalytic water splitting over a semiconductor photocatalyst loaded with H_2- and O_2-evolution co-catalysts with steps *i)* – *iii)*, adapted from Ran et al.[25]

From the thermodynamics point of view, the generation of e^-/h^+ pairs capable of taking part in a redox reaction at the surface of a photocatalyst can only take place, if the incident light's energy is equal or greater than its bandgap. Wide-bandgap semiconductors demand light of shorter wavelengths (greater energies), which limits the use of the entire spectrum of the sun's light. Moreover, VB and CB potentials of the catalyst dictate if a target redox process can take place or not: reduction potentials must be less negative than the CB potential and oxidation potentials must be less positive than the VB potential. This translates to very specific potential positions of the material for a specific redox reaction. Considering overall photocatalytic water splitting, only a limited group of materials could be taken into account.[26,27] Hence, modification strategies have been adopted to address or circumvent these thermodynamic limitations. As such, bandgap engineering and sensitization of the surface of the semiconductor can extend its visible-light absorption. Another promising strategy here involves constructing artificial Z-scheme photocatalysis in which two semiconductors with smaller bandgaps are linked directly or via shuttle redox mediators, while each of them has been optimized specifically for only one of the water splitting half-reactions.[28] In this case, this optimization can be made separately

for each photocatalyst by utilizing the so-called sacrificial water splitting tests. To facilitate the reduction half-reaction, known as the hydrogen evolution reaction (HER), hole-sacrificial agents e.g. MeOH or TEOA can be used. For the water oxidation half-reaction, i.e. the oxygen evolution reaction (OER), electron sacrificial agents e.g. $AgNO_3$ are employed.

Granting proper thermodynamic conditions does not necessarily assure an efficient photocatalyst: The reaction kinetics have a great influence on the overall photo-catalytical performance. Charge carrier dynamics are crucial: they describe how charges are generated through photon absorption, then migrate to the surface and finally get interfacially transferred to the adsorbed reaction partners that subsequently get reduced or oxidized. A major challenge during any of these steps is avoiding e^-/h^+ recombination or trapping. Moreover, surface reaction kinetics should also be considered, i.e. diffusion of the reactant to the catalytically active site, adsorption, charge transfer and consequent product desorption – each may become a limiting process.[20,27] To minimize these performance-lowering effects, strategies including heterojunction implementation, pore tailoring, quantum size effects, surface modifications and co-catalysts loading have been employed. It is widely accepted that heterojunction, i.e. the interface that occurs when contacting two different semiconductors, is one of the most efficient ways to enhance charge separation and transport.[24] Creating macro/mesopores or using high surface area materials not only enhances light-harvesting qualities, but also enhances adsorption/diffusion dynamics. Moreover, using nanostructured, defect-free and high crystallinity semiconductors can result in short charge diffusion lengths, accelerating the charge transfer process. Lastly, loading co-catalysts can have a major effect on the improvement of the reaction kinetics, improving the activity and stability of the photocatalyst.[20,25,28]

2.3. The role of co-catalyst

As shown in **Figure 1B**, the photocatalytic water splitting reaction involves three main steps. The success of an efficient photocatalyst relies on balancing the thermodynamics and kinetics of these steps altogether. Some of the strategies to improve steps *i)* and *ii)* have already been discussed in the previous section. Step *iii)*, that is, the surface reduction/oxidation reactions, often stays the limiting factor and can be substantially optimized through loading the light-harvesting semiconductors with co-catalysts.[23,25]

The surface redox reactions are oftentimes too slow to efficiently utilize the generated charges at the surface, decreasing the overall performance. Co-catalysts provide catalytically active sites for the HER or OER, reducing the activation energy for these reactions. Trasatti reported the relationship between exchange current for H_2 evolution and M-H bond strength, where M is a transitional metal.[29] The resulting volcano-curves show that an optimal metal catalyst should not bind intermediate products too weakly (adsorption of educts suffers) nor too strongly (release of products suffers). Such an ideal co-catalyst, as in the case of metallic Pt, would show the lowest activation energy for the surface reaction and hence increase the catalytic conversion rates.[23]

The aforementioned bandgap engineering, though successful in matching redox levels of the water reduction and oxidation reactions, still lacks the ability to avoid recombination of the charge carriers if these are not extracted efficiently by the reactants. Here, seen as another advantage, some co-catalysts possess the ability to extract electrons if their work functions are greater than those of the semiconductor. The work function (Φ) of a metal describes the energy with which the electrons near the Fermi level are bound to the interior of the solid. These electrons usually take part in electrochemical processes, thus making Φ an important

parameter when describing the behavior of a metal and a metal-semiconductor junction.[29] When a co-catalyst is loaded onto a semiconductor, a semiconductor/co-catalyst interface is built, which is able to assist the e^-/h^+ separation process. This interface is also known as a Schottky barrier, in the case of TiO_2/metal. The Schottky barrier is a kind of hetero-junction, which facilitates the charge carrier separation due to the relative energy levels of the interface. Given a proper junction, charges can be transported in the right direction, due to the built-in electric field at the interface, avoiding recombination and enhancing the overall efficiency.[25,30] As an added benefit here, the loading of co-catalysts can also enhance the stability and robustness of the photocatalyst. Semiconductors often suffer from photo-corrosion under light irradiation, since the generated electrons and holes can take part in decomposition processes. By timely consuming the charge carriers in the desired surface redox reaction, suitable co-catalysts are capable of effectively increasing photostability.[31]

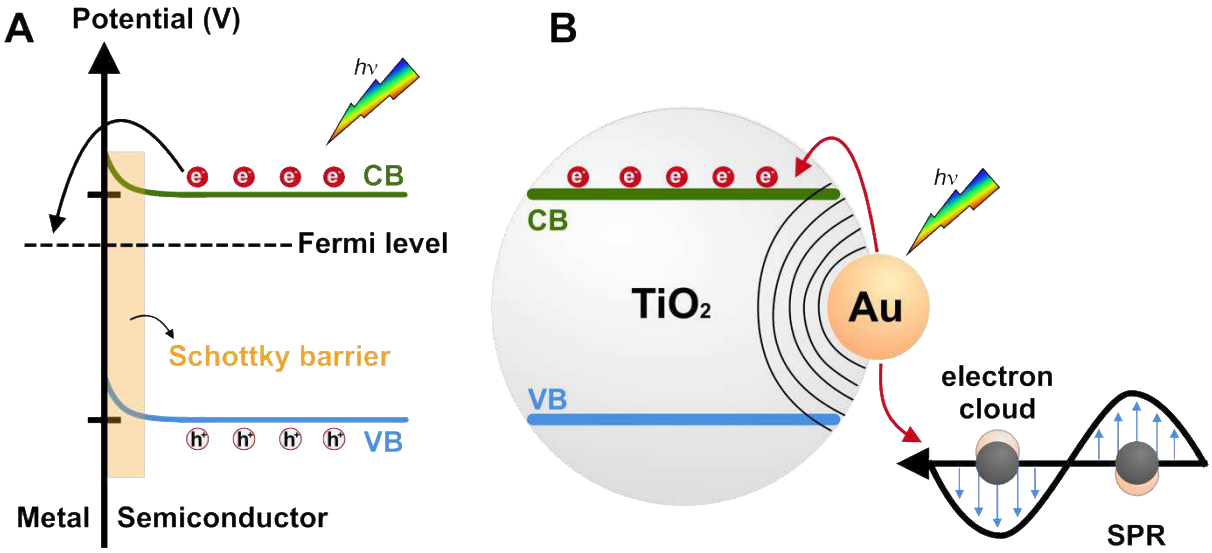

Figure 2 | **A,** Schematic of Schottky junction, adapted from Xiao et al.[30] **B,** Enhancement mechanisms of plasmonic Au NPs on TiO_2, adapted from Li et al.[24]

Lastly, the light-harvesting properties of wide bandgap semiconductors can also be improved by loading co-catalysts that additionally exhibit plasmonic response, like Au or Cu. The localized surface plasmon resonance (LSPR) effect of such metals allows them to be excited by visible light. The generated hot electrons can be injected into the conduction band of the semiconductor, resulting in the extension of its light absorption properties, while maintaining its redox abilities.[30,32]

Important factors to be considered when using co-catalysts are their loading amount, size and structure. Optimal loadings will boost the overall catalytic activity, but overloading the semiconductor might be disadvantageous. Incident light can be blocked by too much co-catalyst, deteriorating the light-harvesting properties of the semiconductor. Moreover, too large co-catalyst particles will show major drawbacks: the proportion of surface-to-bulk metal atoms will decrease lowering the number of surface-active sites and the bulk recombination will be promoted. Hence, charge carriers are less likely to recombine in smaller and highly dispersed particles. Some core-shell structures are also known for suppressing the reverse reaction, achieving higher activities.[25]

2.3.1. Noble and earth-abundant co-catalysts

Recognized as an effective strategy to boost the photocatalyst's activity, noble-metal-based co-catalysts have been widely employed to deliver the highest performances for photocatalytic water splitting. These include Pt, Pd, Rh, Au and Ag which have been vastly investigated, especially for the H_2 evolution reaction. They do not only provide great electron sinks, but also are found at the peak of the volcano curves thus providing most suitable HER catalytical sites.[23,25,29,30]

Unfortunately, noble metals are scarce and therefore costly, which limits their implementation for large scale energy production, as shown in **Figure 3**. Over the past 2 decades, the demand on precious metals has steadily increased, due to investor and speculator interests, as well as their implementation in industry sectors, especially for autocatalysts (as for Pt, Pd and Rh). Being amongst the rarest metals on the earth's crust and the main deposits localized in a handful of nations, unavoidable geopolitics have an enormous impact on their price volatility, also hindering a secure large scale market.[25,33]

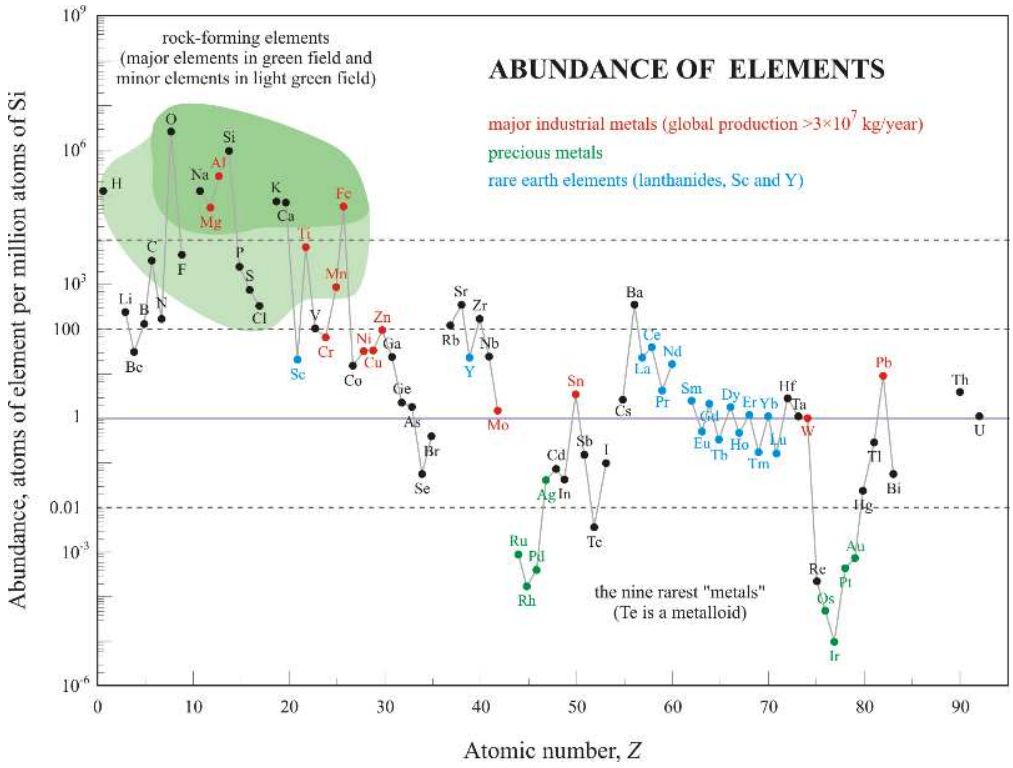

Figure 3 | Abundance of the elements: major industrial metals, precious metals and rare earth elements. Courtesy of E. Generalic, https://www.periodni.com/rare_earth_elements.html, retrieved on May 19th, 2020.

Not only in the realm of photocatalysis, but for many of our modern life technologies, solutions need to be found to gradually shift towards more reliable and continuous supply materials.[34,35] This is why low-cost and earth-abundant transition metals have gained attention as co-catalysts in the last decade. Earth-abundant co-catalysts have been widely investigated for both the HER (Co, Ni and Cu) and the OER (Co, Mn, Ni and Fe). These transition metals are also able to build Shottky barriers and provide catalytic sites for the gas evolution reactions at the surface. Although their overpotential (equivalent to the activation energy) towards H_2 evolution is well known to be less suitable than that of noble metals in the bulk, reducing their

size to the nanoscale has proven to enhance the activities of the employed photocatalyst notoriously.[23,25,29] The extended surface area of nanoparticles or small clusters grants an increased amount of catalytic sites, which makes their activities comparable to the ones of Pt-based co-catalysts, for example.[36] Earth-abundant-based co-catalysts have successfully been prepared by Lee et al.[37] and Takata et al.[38] using Cu and Co, respectively. These contributions have shown extraordinary performances for photocatalytic water splitting.

Earth-abundant metals, being three orders of magnitude cheaper than Pt, become especially appealing for large scale and practical applications, in which costly and scarce noble metals should be ideally replaced.[25,39] Given the superior catalytic properties of noble metals, another strategy to address their high prices would be to maximize their atom utilization in a catalytic reaction. This can be accomplished through the preparation of heterogeneous single-metal-site catalysts (HSMSCs). The design of such systems reduces the amount of employed co-catalysts and hence their cost, while catalytic performance can be preserved or even increased.

2.4. Heterogeneous single-metal-site catalysts (HSMSCs)

2.4.1. Origin and concept

Homogeneous catalysis that mostly relies on organometallic molecular species plays a major role in the synthesis of simple and complex molecules, drug compounds, natural products and many more biomolecules. Due to the well-defined coordinative structure of the molecular catalysts, composed of a catalytically active center and ligands, they have helped to unravel our understanding of the mechanisms of many catalytic reactions. However, these catalysts show major drawbacks, especially when it comes to their separation from the final products and recyclability. These limitations have been tackled by immobilizing them onto a substrate, "heterogenizing" the organometallic structures.[40,41]

The concept of bridging heterogeneous and homogenous catalysis can also be addressed from the heterogeneous side. Here, downsizing a (co-)catalyst nanoparticle would often generally result in greater (photo-)catalytic activities due to the increased amount of atoms that are exposed at the surface, which correspond to a relatively larger number of adsorption and – possibly – active sites. In this regard, the concept of metal atom utilization arises and is referred to as the ratio of the surface and catalytically active atoms to the whole amount of atoms in the volume of the (co-)catalyst nanoparticle. Homogeneous catalysts can reach up to 100% atom utilization, since they are molecular species and every central atom can act as an available catalytic site. In heterogeneous catalysis, where we deal with (co-)catalysts in the form of nano- or even microparticles, a great fraction of the atoms is "not utilized". Taking the downsizing strategy to the extreme would result, ideally, in single atoms at the surface of a support. This would result in a massive increase in the atom utilization efficiency and can be seen as another way to bridge the heterogeneous and homogeneous fields.[42,43]

Such systems are known as single-atom catalysts (SACs). An isolated single atom at a surface cannot be imaginable, since it would always be stabilized by some sort of bonding with the neighboring atoms or functional groups at the surface. Hence, the term heterogeneous single-metal-site catalysts (HSMSCs) seems more appropriate for this work's approach. The "single-site" definition that is used in this Thesis will follow a broad description given by Zecchina et al. as "*a metal atom, ion or small cluster of atoms held by surface ligands to a rigid framework.*" Usual NPs are composed of hundreds or even thousands of atoms, depending on their size and composition. The proposed small clusters of atoms are subnanometer-sized and the atom's number is substantially lower than that for common nanoparticles. This atom number

reduction can change the behavior of the (co-)catalyst drastically not only in terms of activity, but also other phenomena appear, e.g. quantum size effects, metal-support interactions and cluster re-configurations which altogether influence the resulting physicochemical and catalytic properties of the HSMSC. Upon decreasing the number of atoms of such a metal cluster, its "size" will also become less well-defined and thus less important at describing the cluster's properties.[42–45]

Following the concept of HSMSCs, such isolated and active metal centers are located on a support, which will play a crucial role in the stabilization of the single-sites. Usually, high-surface-area and robust supports are implemented, like oxides or (nano)carbon-based networks. The substrate provides, ideally, a unique and selective geometric environment for the single-sites to be stabilized while leaving open reaction sites at the same time.[46] The single-sites are generally stabilized by surface atoms, like oxygen, nitrogen or sulfur, which usually coordinate the metal center. Further stabilizing moieties can be electronic defects, given their high reactivity, including unsaturated sites, defects or vacancies. Additionally, single-sites have been reported to be encapsulated in confined space, like nano- or micropores. Hence, some of the main interactions between the substrate and the single-sites are coordinative and electrostatic, but also covalent in some cases.[42,43,45] As reported by Wang et al., the key for synthesizing single-sites is to disperse the target isolated metal atoms (by reducing concentrations) and suppress the movement and aggregation of these species at the surface (by filtering and washing, only allowing the defect-stabilized species to stay).[46]

It is important to notice that the loadings of single-sites are limited, in theory, by the maximum number of matching sites at the support. The better defined the support is, the more predictable the system will be.[46] However, heterogenous single-sites' supports oftentimes are less well defined than their homogenous counterparts, showing different facets and more random anchoring situations. Therefore, the design process of HSMSCs is often the result of *"an empirical approach with trial-and-error character substantially based on chemical intuition"*.[44]

2.4.2. Advantages of HSMSCs

HSMSCs bridge homo- and heterogeneous catalysis, combining the best of both worlds. On the homogeneous side, the tunability of the systems allows for excellent catalytic performances, especially in terms of activity but also selectivity. The inherent high activity of HSMSCs is especially attractive for industrial processes since they can be improved in selectivity. The maximum atom utilization, which can come close to 100%, is another homogeneous trait that makes these catalysts very attractive, not only economically, but also environmentally.[42]

On the heterogeneous side, stability, separation from starting materials and recyclability are some of the major advantages. Heterogeneous catalysts oftentimes owe their high activities to their high-temperature stability. Using oxides as supports allows to stabilize the metal centers at the surface's metal or oxygen vacancies, which can be heated to higher temperatures, maintaining their integrity over many catalytic cycles.[42,43] Furthermore, many preparation methods for HSMSCs are rather straightforward and scalable, which becomes relevant considering large-scale industrial applications.[45]

2.4.3. State of the art – strategies, materials and reactions

Single-sites have been well-studied in the wide field of heterogeneous (thermal and electro-) catalysis and many systems have been reported to date, showing successful catalytic conversions for CO oxidation, hydrogenation, water-gas shift and hydrogen evolution reactions. However, single-site photocatalysis is a rather new but promising field. The catalytic centers can be tailored selectively to enhance their performances for specific target reactions. Also, the maximum atom utilization efficiency permits the implementation of noble-metal-based (Pt, Au, Rh, Pd) co-catalysts from an economic point of view. The most frequent substrates implemented in single-site photocatalysis are based on titania (TiO_2), ceria, iron oxide, graphene or carbon nitride. Examples of advancements and strategies used in this field, being central to this work, will be emphasized in this subchapter, especially focusing on HER, CO_2 reduction, pollutant degradation and OER.

Improving the efficiency of the HER by using the concept of single-sites has been widely studied. Li et al.[47] loaded PtO-clusters of different sizes onto TiO_2 nanosheets by a ligand-assisted loading method, to correlate cluster size and catalytic performance. The smallest clusters (0.2 nm) were found to have the maximum hydrogen production rate. Xing et al.[48] were able to stabilize single noble metal atoms (Pt, Pd, Rh and Ru) onto TiO_2 by a facile co-precipitation method and indicated their superior performance compared to metal NPs or clusters. Further studies on novel supports have shown the possibility of embedding single Pt-atoms in the subnanopores of 2D graphitic carbon nitride (g-C_3N_4) or well-defined porphyrinic cavities of an aluminum-based metal-organic framework (MOF). The unique tri-s-triazine structure of g-C_3N_4 allows the intercalation of metal atoms with the e-rich N/C Lewis centers of the substrate. Similarly, the porphyrinic moieties of some MOFs are able to strongly coordinate single metal atoms, (see **Figure 4A**). In both cases, the wet impregnation process of the Pt single-sites resulted in enhanced H_2 evolution rates, compared to the Pt nanoparticles analogous.[49,50]

Fewer studies on earth-abundant single-site photocatalysts have been reported for the H_2 evolution reaction. Lee et al.[37] synthesized hollow TiO_2 NPs with well-dispersed atomic Cu-species in their most stable Ti-vacancies, as shown in **Figure 4B**. The atomic Cu acts as a redox-active metal cofactor, which activates the local TiO_2 lattice reversibly during the photocatalytic reaction and enhances the HER's performance. Furthermore, atomic layer deposition (ALD) has also been employed for single-site photocatalysts' preparation based on earth-abundant materials. Peters et al.[51] loaded small nickel sulfide clusters onto a Zr-based MOF, which showed excellent H_2 evolution activities. This study sets the foundation for further investigations on ALD of mixed metal sulfides, which could potentially mimic the cofactors of complex enzymes. In another contribution, Cao et al.[52] used ALD to graft Co-atoms onto g-C_3N_4, resulting in an 11-fold increase of the H_2 production activity, compared to the unmodified support.

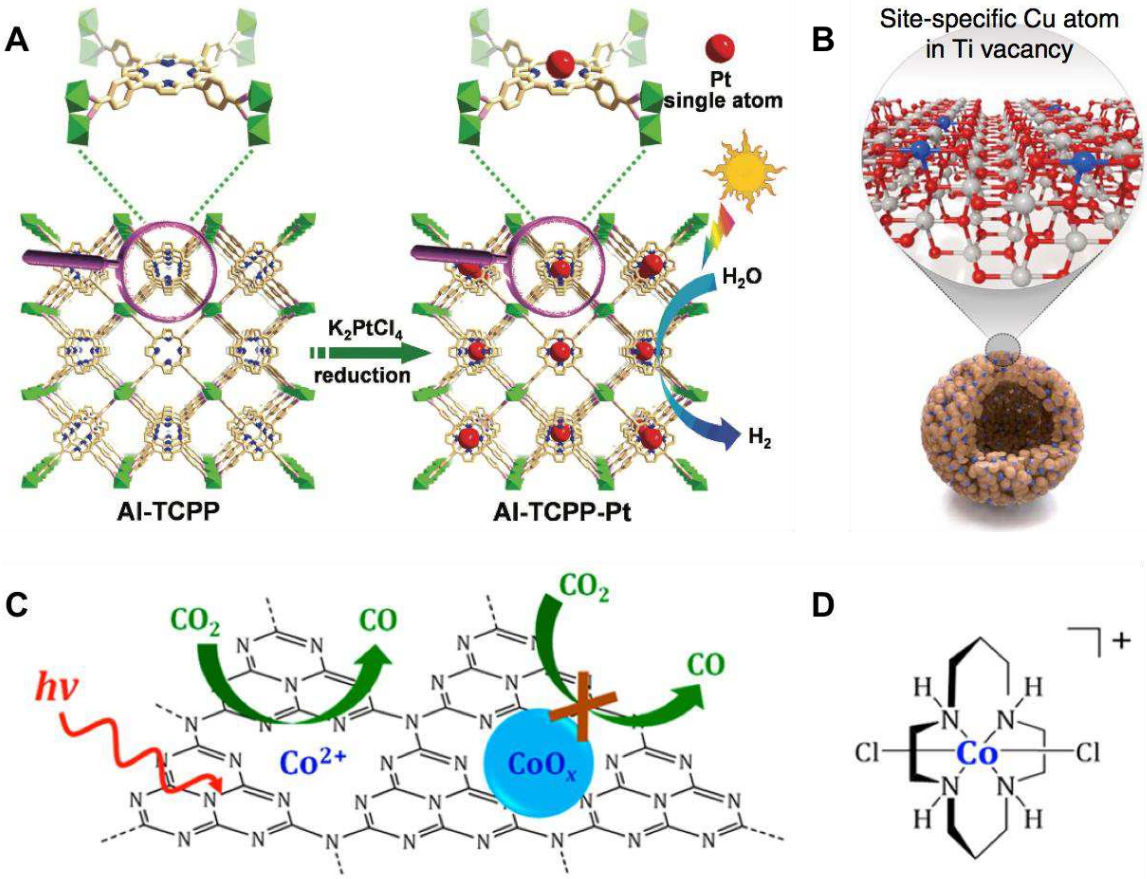

Figure 4 | **A,** Schematic illustration showing the synthesis of Al-TCPP-Pt for photocatalytic hydrogen production taken from Fang et al.[50] **B,** Single-atom Cu/TiO_2 photocatalysts synthesized through the wrap-bake-peel process of Lee et al.[37] **C,** Schematic representation of photocatalytic CO_2 reduction mediated by a single Co^{2+} site on C_3N_4 and **D,** Molecular structure of a macrocyclic cobalt catalyst, "Co-cyclam", both taken from Huang et al.[53]

CO_2 reduction is another important reaction that has attracted attention in single-site photocatalysis due to the importance of generating hydrocarbon fuels from the problematic CO_2. Gao et al.[54] reported the potential of isolated Pt/Pd atoms supported on g-C_3N_4 for CO_2 reduction through DFT calculations. Experimental work from Huang et al.[53] later showed the coordination of Co^{2+} centers on C_3N_4 by a simple deposition method, which selectively reduced CO_2 under visible-light irradiation, as shown in **Figure 4C**. The single-site Co-N coordination structures formed in this photocatalyst when using low Co-loadings resembles the well-studied molecular catalyst Co-cyclam (**Figure 4D**), while excessive Co loadings resulted in the formation of Co NPs, which were photocatalytically inactive. Similarly, Gao et al.[55] then coupled the heterogeneous single-atom Co catalyst with the homogeneous light absorber $[Ru(bpy)_3]Cl_2$ through graphene oxide (GO). Their thermal treatment to stabilize isolated Co-atoms on GO rendered high activities for CO_2 conversion while maintaining the robustness of the system. In another contribution, single Co-atoms were also trapped in the porphyrinic structure of a novel Zr-based MOF, which possesses excellent performances in CO_2 capture and visible-light absorption. The composite showed not only an increase in catalytic activity, but also in CH_4-production selectivity, compared to the pristine MOF.[56]

Organic pollutant degradation, relevant for wastewater treatment processes, has also been successfully addressed by using single-site-based photocatalysis. Wang et al.[57] loaded

single-atom Ag species onto ultrathin g-C_3N_4 through a co-polymerization method. The enhanced photocatalytic activity was ascribed, amongst other factors, to the SPR-effect of Ag together with the high surface area of the substrate. An et al.[58] also used g-C_3N_4 to stabilize highly dispersed small clusters and single atoms of Fe through a pyrolysis process. The high Fe-loadings (up to 18 wt.%) and low iron leaching, confirmed this design to be promising for the removal of organic pollutants.

To the best of our knowledge, only one study on the more challenging half-reaction of the water splitting process, i.e. the OER, has been reported using single-site photocatalysis to date. Liu et al.[59] achieved an exceptional overall water-splitting activity under simulated solar irradiation without using any sacrificial agents or noble metals. Herein, Co_1-phosphide was anchored to phosphorous-doped g-C_3N_4 through a phosphidation method. P-doping enhances the electric conductivity of g-C_3N_4, due to the more delocalized p bonds that promote an increased charge transfer. At the same time, the Co_1-P_4 inhibits charge recombination but also serves as the catalytically active site for the OER. Other groups have reported advancements in the water oxidation or CO oxidation reactions through single-sites, however, in the realm of photoelectro- or thermal catalysis. These systems are often based on noble metals (Ru, Pt, Au) supported on transition metal oxides.[60–62]

To summarize, the various examples of prepared single-site photocatalysts for different catalytic reactions generally utilize synthesis strategies based on wet chemistry, e.g. co-precipitation and impregnation, but also more specialized approaches in the case of ALD. Much research has been devoted to noble-metal-based systems, although earth-abundant metals, e.g. Cu, Ni, Fe and especially Co have gained a lot of attention recently. The most common supports are TiO_2, MOFs with porphyrinic struts and g-C_3N_4.

2.4.4. Challenges for HSMSCs

Working in the realm of single-sites which are built of few atoms to small clusters becomes remarkably challenging. Reproducible synthesis of nanoclusters with the same configuration and number of atoms dispersed on a high-surface-area substrate is extremely difficult. The supported species often coexist as single-atoms, small clusters and even NPs. Having a very small amount of atoms in the cluster also limits the implementation of widely accepted thermodynamic concepts, which are based on the statistical behavior of many events caused by many atoms. The aforementioned quantum effects arise, which might reset the energy levels of the cluster by adding/removing one “extra” or “foreign” atom to the cluster. Slight changes in the number of atoms cause sudden fluctuations in the cluster’s structural, electronic, optical, magnetic and chemical properties, which makes the correlation of any of these parameters to the observed catalytic performance a formidable task.[45,63–67]

Moreover, the differently exposed facets of commonly used heterogeneous supports provide difficulties to elucidate the precise bonding situation between support and single-site. This can be addressed by producing well-defined supports with specific facets of interest exposed. However, theoretical DFT calculations need to be usually undertaken before realizing actual experiments. Such efforts may result as complicated and pricey for large-scale implementation.[44,68,69]

Undoubtedly, the greatest challenge when investigating HSMSC concept is the ubiquity of complex and sophisticated characterization techniques that need to be implemented for their

study.[42,43,45,46] The most intuitive approach to confirm the existence and distribution of single-sites on high-surface-area support is to image them. The required atomic-resolution for imaging such small clusters is only reached through special techniques, i.e. high-angle annular dark-field scanning transmission electron microscopy (HAADF-STEM). Although this technique has provided invaluable images to understand and optimize HSMSCs more in detail, it is limited by its local focus, required high contrast between the matrix and the single-sites and does not provide structural information of the whole sample.

Also, powerful X-ray spectroscopy techniques are being used to provide average information about all the species bonding situation in the catalyst and their oxidation states. These include extended X-ray absorption fine structure (EXAFS) and X-ray absorption near edge structure (XANES), respectively. Both techniques require synchrotrons, which makes their access rather limiting. X-ray photoelectron spectroscopy (XPS) could also help elucidate the present species and their neighboring environment on the surface, but sensitivity may become a limiting factor.

Special *in-situ* or *operando* IR-spectroscopy techniques have provided complementary information in the field of single-site catalysis. Although they usually require complex experimental setups, they have helped to confirm the existence of single-sites and also elucidating the catalytic reaction mechanisms and their dynamics. Lastly, the implementation of theoretical modeling and simulations of HSMSCs has also played a major role in their understanding and development.

3. Motivation and Aims

It is clear from the introduction section, that earth-abundant semiconductors and co-catalysts are of great interest for the production of solar fuels through photocatalysis. However, for earth-abundant materials to compete with noble metals, further developments on enhanced light-harvesting and stabilization of single-sites are necessary. On the other hand, creating noble metal systems with a single-site nature could potentially reduce the cost of these photocatalysts by maximizing the atom utilization.

In this project, we aim to relate the amounts of different co-catalysts immobilized on a model support (TiO_2) to their photocatalytic activities, which will help to expand our understanding of eventual single-site formation. To further enhance light-harvesting properties and promote the formation of single-sites, the support's surface will be modified with phosphate groups that can provide anchoring sites with stronger adsorption capacity.

Motivation:

- The single-site concept in photocatalysis can yield more unique and selective co-catalysts to address the challenges of water splitting and CO_2 reduction.
- Phosphate groups can enhance light-harvesting properties at the support's surface, while simultaneously stabilizing single-sites more strongly than bare TiO_2.
- Earth-abundant systems have been proven to be promising but are still underexplored in literature.
- Noble metal systems show superior activities but are expensive. A better atom utilization of such systems could make their implementation more feasible.
- Single-site photocatalysis is a rather new topic and our understanding of the design of such systems needs to be expanded.

Aims:

- Develop reliable protocols for reproducible synthesis towards single-site photocatalysts based on the wet-impregnation process.
- Investigate the formation of co-catalysts' single-sites and their stability by using the isolation strategy and substrate modification of TiO_2 with PO_4 groups.
- Understand the commonalities and differences between earth-abundant and noble metal co-catalyst systems.
- Evaluate photocatalytic activity trends for the hydrogen evolution reaction for a series of different co-catalysts.
- Develop structural models to explain and understand the catalytic performance in relation to the amount of co-catalyst used.

4. Materials and Methods

4.1. List of chemicals

All materials used for the syntheses were obtained from commercial suppliers. The following table contains information on the identification and purity of the used chemicals. All of them were used without further purification.

Table 1 | Information on the used chemicals.

Chemical formula	Name	CAS number	Purity	State
CH_3OH	Methanol	67-56-1	absolute	-
TiO_2	Anatase	1317-70-0	99.7 %	-
H_3PO_4	Phosphoric acid	7664-38-2	extra pure	85 % solution in water
$Mn(Ac)_2{\cdot}4H_2O$	Manganese(II) acetate tetrahydrate	6156-78-1	99.99 %	-
$Fe(Ac)_2$	Iron(II) acetate	3094-87-9	99.99 %	-
$Co(Ac)_2{\cdot}4H_2O$	Cobalt(II) acetate tetrahydrate	6147-53-1	99 %	-
$Ni(Ac)_2{\cdot}4H_2O$	Nickel(II) acetate tetrahydrate	6018-89-9	99 %	-
$Ni(AcAc)_2$	Nickel(II) acetylacetonate	3264-82-2	96 %	-
$Cu(Ac)_2{\cdot}H_2O$	Copper(II) acetate monohydrate	6046-93-1	99 %	-
H_2PtCl_6	Hexachloroplatinic(IV) acid solution	16941-12-1	-	8 wt.% solution in water
$HAuCl_4{\cdot}3H_2O$	Tetrachloroauric(III) acid trihydrate	16961-25-4	99.99 %	-
$AgNO_3$	Silber nitrate	7761-88-8	99 %	-

4.2. Characterization methods

Different methods were used to characterize the prepared catalysts. The absorption spectrum, chemical identity, real loading amounts, oxidation states, morphology as well as size and distribution on the supporting material was of interest. Below is a list of all used methods, a short description of each, and the reason why the method was applied.

4.2.1. Attenuated total reflection Fourier-transformed infrared spectroscopy (ATR-FTIR)

ATR-FTIR is a reliable spectroscopic method for fingerprint recognition of IR-absorbing materials. This method enables the recognition of characteristic functional groups in solid, liquid or gaseous samples.[70] To qualitatively confirm the phosphate-modification of TiO_2, an ATR-FTIR spectrometer (Perkin Elmer, Spectrum Two) was used with a Single Reflection Diamond accessory. The sample was measured in the solid-state.

4.2.2. Diffuse reflectance spectroscopy (DRS)

DRS is referred to as UV-Vis spectroscopy in solid-state and can be used to evaluate the absorption properties of supported thin films and free-standing powders. Construction of Tauc plots further enables the determination of the bandgap characteristics.[71] In a single measurement, a thin film of the powdered sample was formed using a designated sample holder and its reflectance profile was recorded in the range between 200 and 800 nm relative to $MgSO_4$ reference using Jasco 670 spectrometer and 2 mm sample holder.

4.2.3. Total reflection X-ray fluorescence spectroscopy (TXRF)

TXRF is a powerful qualitative and quantitative technique for chemical multi-elemental analysis. Mainly liquid samples but also solids can be analyzed with detection limits in the ppb range.[72] Functionalization of TiO_2 with PO_4 groups, concentrations of co-catalysts in washing solutions and co-catalyst loading amounts can be determined through this method.
Quantitative chemical analysis to determine the metal loadings (wt.%) of solid nanocomposites was performed with Total Reflection X-ray Fluorescence (TXRF) using an ATOMIKA 8030C X-ray fluorescence analyzer. A Mo X-ray tube was used for sample excitation (monochromatized Kα-line) at 50 kV and 47 mA for 100 s, using the total reflection geometry and an energy-dispersive Si(Li)-detector. 1 mg of the samples were fixated at the center of quartz reflectors by pipetting 5 µL of a 1% polyvinyl alcohol (PVA) solution and drying for 5 min on a hot plate. Unloaded reflectors were measured beforehand to account for true blanks and after every set of measurements to rule out contaminations in the analyzer. Ti was set as the matrix with 100% and relative amounts of the loaded element of interest were acquired (wt.%).

For liquid samples, a Wobistrax TXRF analyzer was employed. The source was a Rh X-ray tube (monochromatized Kα-line), at V = 50 kV and I = 0.7 mA. Measuring time was also 200 s, total reflection geometry and a Si detector were implemented. The liquid samples were added a Ga/Y internal standard (10 ppm) for quantification. They were pipetted (5 µL) on the quartz reflectors and dried on a hot plate.

4.2.5. Transmission electron microscopy (TEM)

TEM is an important technique for nanomaterials characterization. It allows the imaging and (chemical) characterization of materials on a nanometer scale. Hereby, an electron beam goes through a thin sample, causing elastic and inelastic scattering interactions which get magnified through electromagnetic lenses.[73] Transmission electron microscope (TEM) images were recorded on a Fei Tecnai F20 transmission electron microscope operating at 200 kV.

4.3. Photocatalytic tests

To test the photocatalytic activity of the prepared composites hydrogen evolution reaction (HER) experiments were conducted. In a single experiment, a sample of interest (10 mg) was sonicated in a 40 mL 1:1 mixture of water and methanol (used here as a sacrificial electron donor) for 60 seconds. The suspension was then transferred to the water-cooled reactor (see **Figure 5**) and it was purged with argon (100 mL min^{-1}) for 5 minutes to deaerate the reactor volume and remove dissolved gases (O_2, CO_2) under stirring at 300 rpm. Subsequently, the reactor was closed with a quartz glass window held by a metal lid. Argon was flushed for a further 5 minutes and then the flow was changed to 30 mL/min, at which point the data acquisition started. After approximately 30 min of flow stabilization, the UV-lamp (365 nm) was turned on. For most experiments, the illumination time was set to 30 minutes, after which the light was shut off, data acquisition stopped and the experiment terminated.

The reactor was placed in a dark-box to avoid interaction with any other light source. Argon flows were regulated by a mass flow controller and the hydrogen evolution was detected in real-time using an Emerson X-Stream gas analyzer capable of detecting H_2 concentrations in the gas phase (in ppm) by a thermal conductivity detector. Besides H_2, the X-Stream analyzer is also capable of detecting CO_2, Cl_2 and O_2 with IR-, UV- and paramagnetic detectors, respectively.

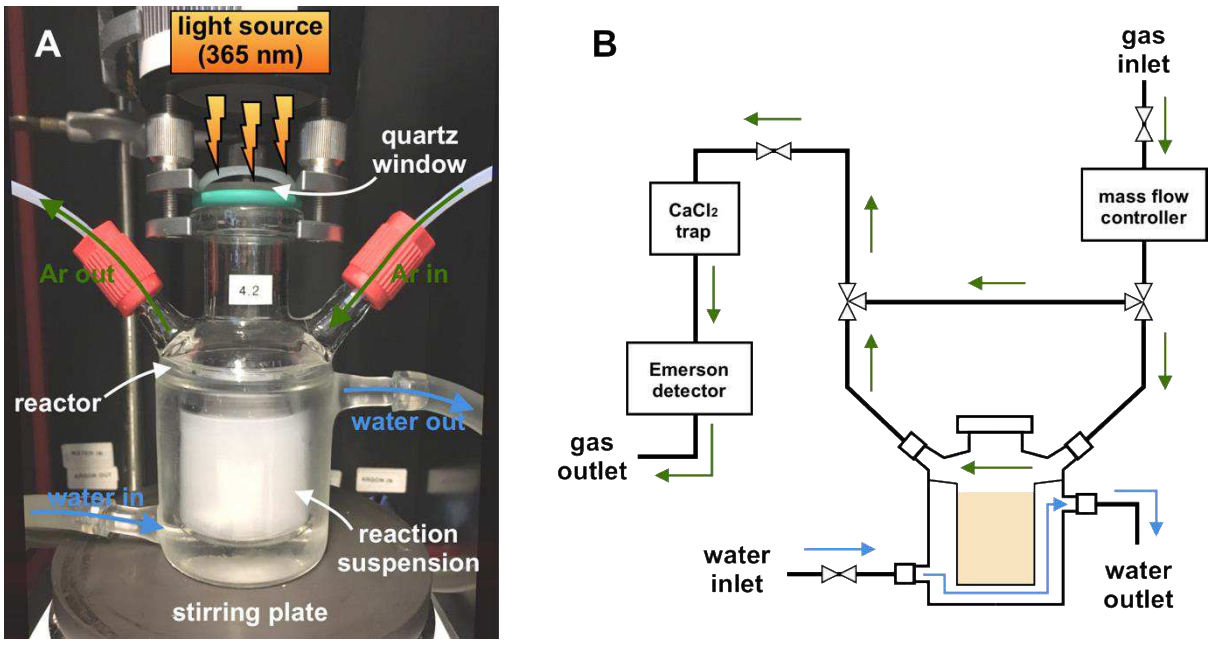

Figure 5 | **A**, A photograph of the photocatalytic flow reactor used for HER measurements. **B**, Scheme of the experiment including water and gas lines.

4.3.1. Efficiency of a photocatalyst

The HER-activity recorded by the X-Stream analyzer was given in ppm and was transformed with the aid of the ideal gas equation **(8)** and the argon flow rate (in mL min^{-1}) to mols of H_2 that were produced per time unit. This activity will be further referred to as "H_2 evolution rate" and is given in µmol h^{-1}. Our following conversions used the resulting equation **(9)**. The value at the denominator arises from the standard conditions used: T = 298 K, p = 101.33 kPa and R = 8.314 m^3 Pa mol^{-1} K^{-1}.

$$pV = nRT \tag{8}$$

$$H_2\ evolution\ rate\ (\mu mol\ h^{-1}) = \frac{activity\ (ppm) \cdot flowrate\ (mL\ min^{-1})}{407.5} \tag{9}$$

This H_2 evolution rate, while useful for describing the overall activity of the composite catalyst, does not account for the catalytically active sites. To be able to qualify the efficiency of a specific and catalytically active co-catalyst species, further parameters need to be taken into consideration. The turnover frequency (TOF), which made its first appearance in hetero- and homogeneous catalysis at first as borrowed term from enzymatic kinetics, is still a term of debate, which is why a precise definition is very important.[74] We adopt a similar TOF definition to the one that Ye et al. have proposed: *"the ratio of the number of the molecules produced per unit time at a single active site."* [75] The TOF of our catalysts is calculated as in equation **(10)**:

$$TOF\ (h^{-1}) = \frac{number\ of\ produced\ H_2\ molecules\ (mol)}{number\ of\ active\ co-catalyst\ sites\ (mol) \cdot time\ (h^{-1})} \tag{10}$$

TOF values are convenient to be estimated in homogeneous catalytic systems. Calculating the TOF value of a heterogeneous catalyst is rather difficult, because the actual number of catalytically active sites is not usually defined accurately. However, since HSMSCs are bridging homo- and heterogeneous catalysis, our number of active co-catalyst sites will be equal to the amount of co-catalyst estimated on the respective composite material. For high loadings of co-catalyst species, which will likely form nanoparticles, the actual number of active sites will be less, since only the atoms at the surface of a nanoparticle would take part in the photocatalytic reaction, increasing the TOF-values. However, for the sake of comparability with the lower loadings systems, in which a better atom utilization is expected, amounts of co-catalysts will be considered as the number of active sites throughout this work.

Furthermore, another important parameter to evaluate the stability of a catalyst is the turnover number (TON). This is a dimensionless number and is defined as: *"the number of the molecules produced per catalytic site before deactivation under given reaction conditions."* [75] In other words, the TON describes the total number of turnovers until the catalyst is completely used up, which ideally should be an infinitely large number for a perfect catalyst. In our case, the TON would be calculated as in equation **(11)**:

$$TON = \frac{number\ of\ produced\ H_2\ molecules\ (mol)}{number\ of\ active\ co-catalyst\ sites\ (mol)} \tag{11}$$

5. Experimental Part

5.1. Synthesis of phosphate-modified TiO_2

The phosphate modification of TiO_2 was performed through a wet impregnation process, similar to the ones reported by Davydov, Zhao and Liu.[76–78] TiO_2 (2 g, 25 mmol) was dispersed in 300 mL of DI water by sonicating for 10 minutes at room temperature. 200 mL of a 12.2 mM phosphoric acid solution was added onto the dispersion under stirring. The new concentration of phosphoric acid in this dispersion was 4.90 mM, which was the calculated amount of PO_4^{3-} ions (2.45 mmol) to get an excess coverage (200%) of the surface area (80 $m^2\ g^{-1}$) of the used TiO_2. The dispersion was stirred for 1 h at 500 rpm, then sonicated again for 10 minutes to homogenize the dispersion components and facilitate phosphate ions reaching the particles' surface. The dispersion was stirred for further 4 h at room temperature (RT) to ensure complete adsorption of phosphate ions onto the surface. Subsequently, the phosphate-modified TiO_2 was filtered and washed thoroughly with DI water until the filtrate was of neutral pH. The washing solutions were saved for further analysis. For drying, the wet filter cake was put into the oven overnight at 60 °C. Finally, the dry sample was mortared and labelled the named PO_4/TiO_2.

5.2. Co-catalyst modification of TiO_2 (impregnation process)

The precursors selected for the transition metal modification were metal acetate (Ac) hydrates ($Mn(Ac)_2{\cdot}4H_2O$, $Fe(Ac)_2$, $Co(Ac)_2{\cdot}4H_2O$, $Ni(Ac)_2{\cdot}4H_2O$ and $Cu(Ac)_2{\cdot}H_2O$) and for nickel, an additional acetylacetonate (AcAc) precursor was used: $Ni(AcAc)_2$. The precursors selected for the noble metal systems were chlorometallate acids or nitrates (H_2PtCl_6, $HAuCl_4$ and $AgNO_3$). Using the metal acetates and nitrates, stock precursor solutions (c = 10 g L^{-1}) were prepared in DI water. Due to solubility problems, the stock solution for $Ni(AcAc)_2$ was 0.2 g L^{-1}. The stock solutions for the chlorometallate acids were prepared under argon and kept under dark to prevent undesired nanoparticle formation. The concentrations were 0.8 and 1 g L^{-1} for H_2PtCl_6 and $HAuCl_4$, respectively.

For the impregnation process, 50 mg of the selected substrate material (TiO_2 or PO_4/TiO_2) was suspended in 50 mL of DI water by sonicating for 10 minutes to break down the eventually agglomerated nanoparticles and expose their surface area for easier accessibility of the precursors. The desired volume of the precursor solution was consequently added to the substrate suspension, calculated depending on which ideal loading was aimed for. The investigated metal loadings were between 0.008 and 5 wt.%. To secure a proper dispersion of the precursor, the suspension was sonicated again for further 5 minutes. The suspension with the precursor was then stirred for 1 h at 550 rpm to secure complete adsorption at the surface of the support. The impregnated product was then filtered and washed 3 times with 50 mL of DI water to remove weakly bound precursor species (both cations and anions). The washing solutions were saved for further elemental analysis. Finally, the wet filter cakes were dried overnight in the oven at 60 °C. A set of control samples of the bare supports were also prepared following the same procedure but not adding any precursor solution. The general naming of these "composite materials" works as follows: wt.%/Metal@Support. As an example, adding 5 wt.% of copper to the phosphate modified TiO_2 would result in a sample referred to as $5/Cu@PO_4/TiO_2$. It must be noted that real loadings vary from ideal ones, since precursor metal species are being washed away from the surface. However, the naming shall account for ideal aimed loadings, although in many cases real loadings are lower than stated by the sample name.

5.2.1. Estimation of the maximum loading

To achieve isolated single-sites of the metal co-catalyst, their dispersion on the substrate's surface becomes very important. Low loadings help to prevent the growth of co-catalyst nanoparticles on the surface and facilitate the stabilization of single-sites by the TiO_2 binding sites e.g. defects, step edges etc. To model the relation between the metal loading and the TiO_2 surface area coverage, calculations were conducted, taking into consideration the surface area of the TiO_2-batch (estimated by BET-measurements) and the size of the corresponding precursor atoms.[79]

Considering the maximum weight percent used in this work, e.g. 5 wt.%, and taking copper with a radius of r_{Cu} = 135 pm as an example, the surface area covered by these atoms – dispersed homogeneously resembling a monolayer fashion – would not surpass 43% of the TiO_2-nanoparticles' surface area (SA):

$$SA_{TiO_2} = 80\, m^2 g^{-1}$$

For preparing a batch of impregnated particles a mass of m_{batch} = 50 mg TiO_2 was taken, so the SA of the batch can be obtained through:

$$SA_{batch} = SA_{TiO_2} \cdot m_{Batch} = 80\, m^2 g^{-1} \cdot 0.05\, g = 4\, m^2 g^{-1} \quad \textbf{(12)}$$

The area that a copper atom would occupy can be obtained through its radius, when

$$A_{Cu} = (2 \cdot r_{Cu})^2 = (2 \cdot 135\, pm)^2 = 7.3 \cdot 10^{-20}\, m^2 \quad \textbf{(13)}$$

For 5 wt.% loading of a 50 mg batch, the loaded mass of copper is m_{Cu} = 2.5 mg. Using the molar mass of copper, M_{Cu} = 63.55 and **Formula 14** the number of moles of copper atoms n_{Cu} can be calculated:

$$n = \frac{m}{M} \quad \textbf{(14)}$$

$$n_{Cu} = 39.3\, nmol$$

By multiplying n_{Cu} with the Avogadro constant N_A = $6.022 \cdot 10^{-23}$, the total number of copper atoms for this loading is obtained. Subsequently multiplying this number by A_{Cu} results in the total area that all copper atoms occupy for this loading:

$$A_{Cu}^{all} = n_{Cu} \cdot N_A \cdot A_{Cu} = 1.73\, m^2 \quad \textbf{(15)}$$

For this example, the percentage of surface area covered, $\%_{SA}$ results from:

$$\%_{SA} = \frac{A_{Cu}^{all}}{SA_{batch}} \cdot 100\,\% = 43\,\% \quad \textbf{(16)}$$

All used transition-metals have similar radii, so this consideration can be qualitatively applied to all of them equally. As the wt.% goes down, so does the percentage of coverage of SA and so, the tendency to form isolated single-sites. The 0.008 wt.% samples have a maximum coverage of 0.07 %. Hence, isolation of the co-catalyst species is granted.

5.3. Temperature post-treatment = role of the ligand

Due to the possibility of remaining acetate groups at the surface of the composites, a temperature post-treatment was undertaken to strip the acetate groups off and eventually make the metal co-catalyst more easily accessible by the water molecules for enhanced photocatalytic activities. 11 mg of selected composite materials (0.008/Cu@TiO_2, 0.008/Au@TiO_2, 0.008/Pt@TiO_2 and 0.2/Ni@TiO_2) were put into the oven for 3 h at 250 °C under air atmosphere. The cooled down samples were weighed, whereby no mass difference could be observed, indicating that the prior repeated washing of the samples already removed the acetate groups. This hypothesis would then be further evaluated with HER-Experiments.

5.4. Synthesis in the dark = role of photodeposition

Light-triggered particle growth of the precursor species constitutes an issue when aiming towards well dispersed and isolated single-sites on the surface of the substrate. Hence, impregnation experiments under darkness were performed. The process for co-catalyst modification of TiO_2 was analogous to the one previously described in **Section 5.2**, but light was completely blocked by covering all the used vials completely with aluminium foil. These samples were added the suffix “dark”.

5.5. Photodeposition experiments

To evaluate the effect of light on the impregnation process and growth of co-catalyst nanoparticles during photocatalysis, photodeposition (PD) experiments were carried out. TiO_2 (10 mg, 125 nmol) was suspended in a 1:1 mixture of H_2O and MeOH by sonicating for 1 minute. This suspension was transferred to the HER-Reactor, which was bubbled with argon for 5 minutes. Before closing the reactor, the desired amount of co-catalyst precursor solution was added into the reactor, following the calculations mentioned in **Section 5.2.1**, to generate the composite material in-situ during the catalytical reaction. After further 5 minutes of bubbling, the HER-Experiment was started as explained in detail in **Section 4.2** The illumination time was of 30 minutes using a 365 nm LED-lamp. It must be noted that the whole amount of co-catalyst is taking part in the photocatalytic reaction for these experiments, which is why ideal loadings are taken as real ones. In comparison, the impregnation process renders composite materials, in which a significant amount of the precursor is being washed away from the sample before the HER-experiment. After the catalytic reaction, the suspension with the photodeposited composite of co-catalyst and TiO_2 was preserved for further analysis.

5.6. Sample Overview

As a result of the project, we have prepared a number of samples. **Table 3** is found at the **Appendix** and lists their internal and external names and gives a summary of important experimental conditions and observations relevant to the project outcome.

6. Results and Discussions

This section will present the obtained results. First, we will discuss the substrate modification, second, the composite materials resulting from the impregnation process of different co-catalysts on the two supports and third, the hydrogen evolution reaction (HER) experiments, the activities of the composite catalysts and theoretical models explaining their behavior. At the beginning of the project, a screening phase for HER-active materials was conducted. Only the catalysts with relevant HER-activity will be shown in this section.

6.1. Supports

As described in the introduction part, support plays a key role in the stabilization of single-site species and for light-harvesting. Hence, bare TiO_2 and phosphate-modified TiO_2 were investigated to elucidate if the formation and stabilization of more active single-site species could be facilitated through this surface modification. Results regarding the two supports used throughout this Thesis will be discussed in the following section.

6.1.1. TiO_2 vs. PO_4-modified TiO_2

The PO_4-modified TiO_2 was different from the normal TiO_2 upon observation since the particles were looser and had a “fluffier” nature. This was the first indicator for a modification as covering TiO_2 with phosphate ions is expected to render the surface more negatively charged, making the particles repel each other more than for the normal TiO_2. The successful functionalization was qualitatively confirmed through FTIR-measurements. **Figure 6** shows the FTIR-spectra of the as measured TiO_2 and PO_4/TiO_2 (**A**) and the baseline-subtracted PO_4/TiO_2 (**B**).

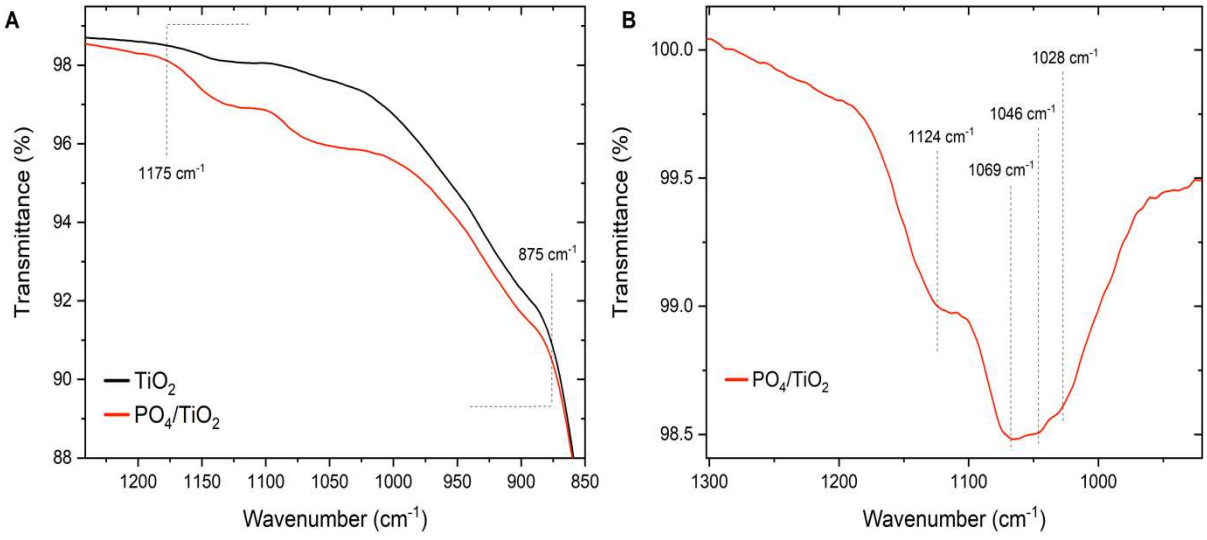

Figure 6 | **A**, Comparison of the FTIR-Spectra for TiO_2 (black) and PO_4/TiO_2 (red). Dashed corners mark the regime of interest. **B**, Baseline-subtracted spectrum of PO_4/TiO_2. Vertical dashed lines mark the peaks of interest.

As previous literature has reported, the shoulder appearing at the region between 1175 and 875 cm^{-1} is an indication for phosphate groups on the titania’s surface. Upon baseline-

subtraction, the specific modes are clearer to appreciate, as seen in **Figure 6B**. Three IR-absorption peaks are visible at 1028, 1046 and 1069 cm^{-1}, and a shoulder at 1124 cm^{-1}, which all correspond to phosphorus-oxygen stretching modes in the phosphate anion, according to previous reports.[76–78]

The comparison of both substrates' DRS profiles (**Figure 7**) shows how the absorption spectrum of the PO_4/TiO_2 has an increased visible light absorption at wavelengths greater than 400 nm. Using Kubelka-Munk calculations and the resulting Tauc plots, the bandgap energy, E_g, can also be obtained for both samples by linear extrapolation of the slope tangent to y-axis. This results in bandgap energies of 3.20 and 3.15 eV for bare TiO_2 and PO_4/TiO_2, respectively. This accounts for a slight narrowing of the bandgap of the modified support, which is potentially advantageous for visible-light applications, in which the light-harvesting process would be enhanced by an additional absorption of the visible range of the solar light.

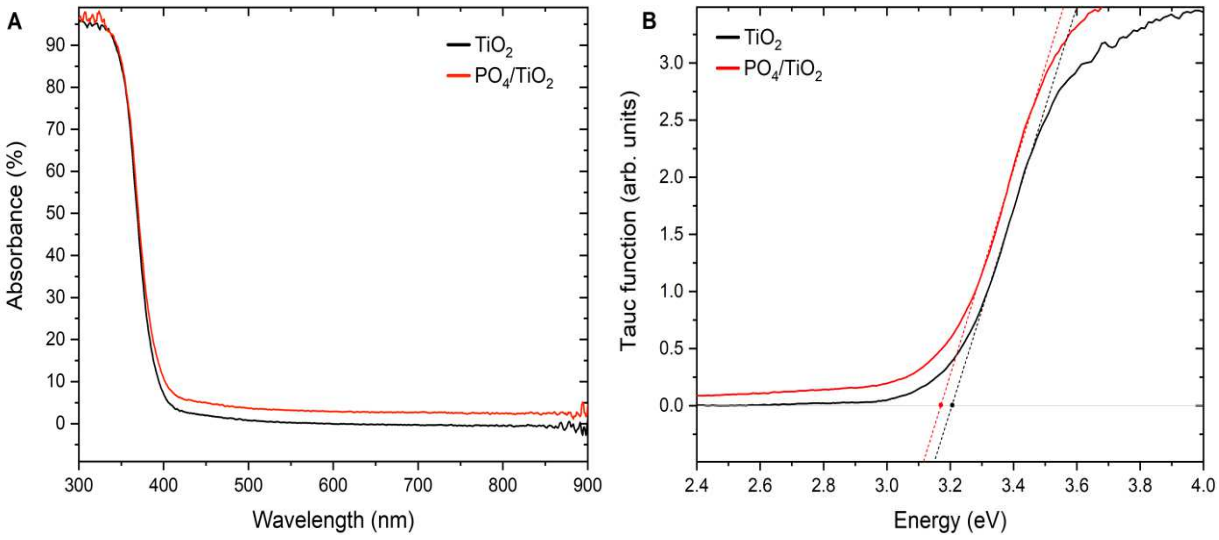

Figure 7 | **A**, Comparison of the DRS-Spectra for TiO_2 (black) and PO_4/TiO_2 (red). **B**, Tauc-Plots for TiO_2 (black) and PO_4/TiO_2 (red).

The quantitative TXRF-analysis of the PO_4/TiO_2-sample and its washing solution, followed by calculations considering the surface area, TiO_2 nanoparticles size and phosphate ion size, results in a surface coverage with PO_4 ions between 50 % (minimal value) and 72 % (maximal value) of the anatase support. This calculation accounts for a monolayer of phosphate ions at the surface.

Overall, the combination of three qualitative and quantitative methods strongly suggests that the surface of the TiO_2 NPs was successfully modified with PO_4 groups leading to a change in the surface characteristics (chemistry, surface charge, adsorption strength) and increased visible light absorption.

6.2. Co-catalysts on bare TiO_2: single-sites or nanoparticles?

The single-site photocatalysts' preparation method used in this work followed the so-called isolation strategy (synthetic details in Section 5.2.), which assumes that the formation of single-sites is more likely to be achieved by isolating the precursor species on the support's surface and by suppressing their movement and potential growth. To probe the effect of site isolation experimentally, we varied the initial precursor concentration within 3 orders of

magnitude, ranging from 0.008 to 5 wt. % loadings. Lower concentrations presumably facilitate single-site stabilization. Moreover, all samples were washed thoroughly (Section 5.2), to only allow strongly adsorbed defect-stabilized species to stay. This isolation strategy towards the single-sites is represented in **Figure 8**.

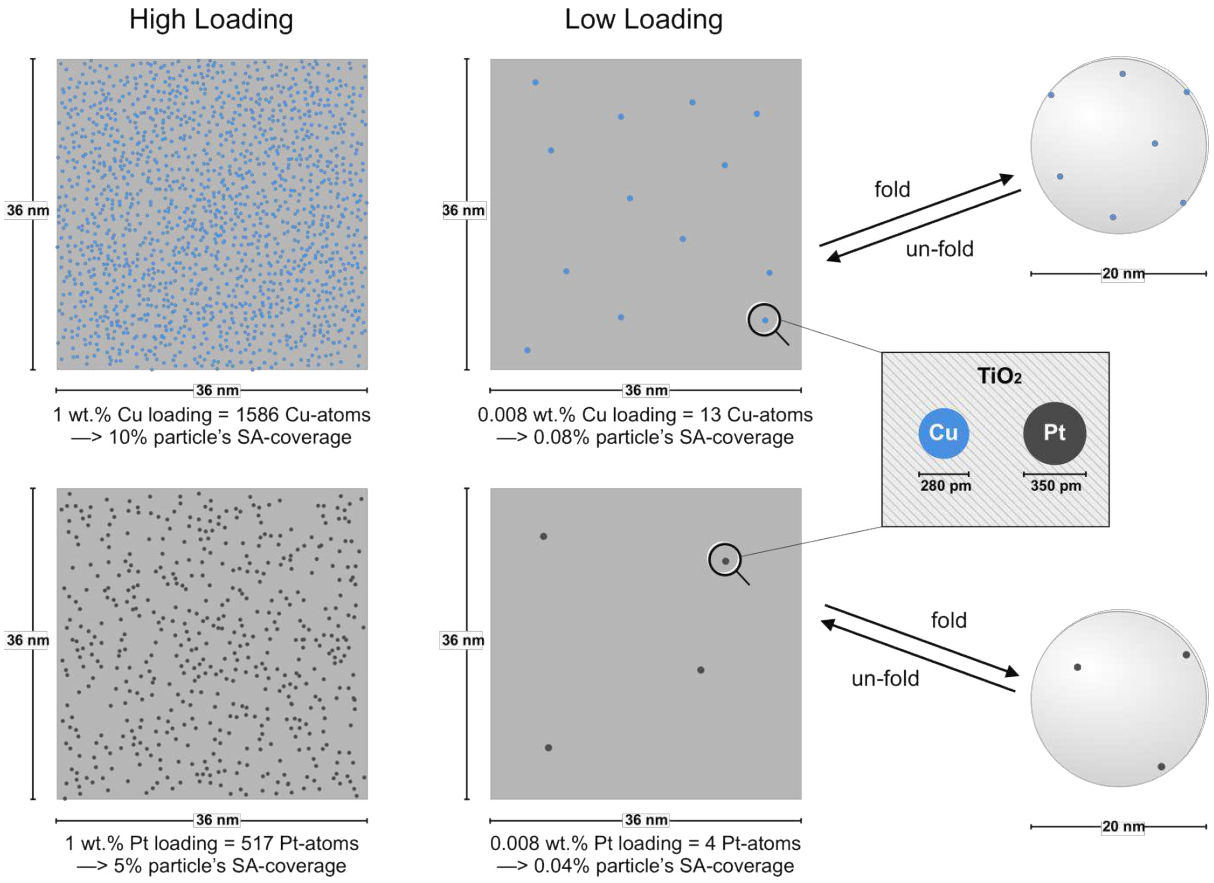

Figure 8 | Graphical representation of scaled atoms and TiO_2 nanoparticle's surface area (SA) for a high = 0.1 wt.% (left) and low = 0.008 wt.% (center) loadings of Cu (blue) and Pt (grey), respectively. Wrapped TiO_2 nanoparticle with low co-catalyst loadings (right).

As can be seen from the simulated schematics, high co-catalyst loadings allow the neighboring sites to interact, which could potentially lead to the nanoparticle formation. However, when going towards the lowest loadings, only a small number of atoms is deposited on each TiO_2 particle. As a result, such nanoparticle formation can be hindered, and only small clusters could be formed instead. Even in this case, however, such small clusters would satisfy our definition of single-sites, which was described in detail in Section 2.4.1, even if they were totally dispersed or agglomerated together.

6.2.1. TXRF in liquid and solid phase

To assure that the impregnated co-catalyst species were stabilized at the surface of TiO_2 and that a leaching process was not occurring, liquid washing solutions from the impregnation process, as well as the solid composite materials were investigated with regard to their elemental composition. As **Figure 9** shows, the amount of Cu found in the washing solutions is significantly reduced with each washing step.

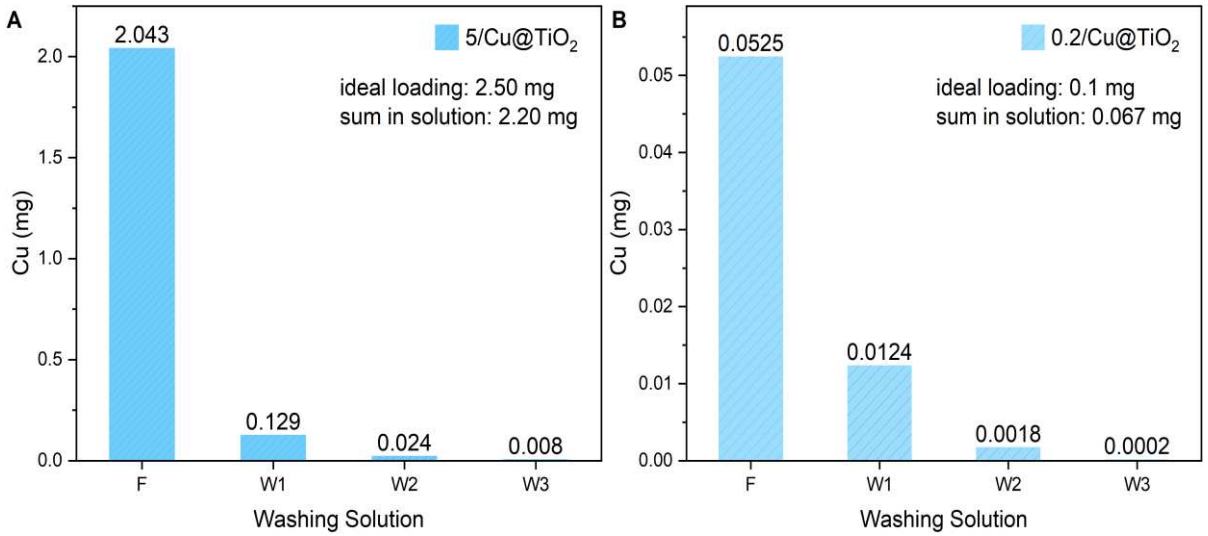

Figure 9 | Cu content in the Filtrate (F) and in the following solutions of every washing step (W1, W2 and W3) for **A**, 5/Cu@TiO_2 and **B**, 0.2/Cu@TiO_2. Ideal aimed loadings (2.5 and 0.1 mg, respectively) are not achieved due to the high amount of Cu found in the solutions.

This result shows that a substantial amount of the precursor species stays in the liquid phase during the impregnation process and co-catalyst gets washed away afterward in the washing steps, resulting in a lower "real" loading (0.30 mg) compared to the "ideal" loading (2.50 mg in the case of 5/Cu@TiO_2) that was aimed for. Nevertheless, after the third washing step, the amount of co-catalyst being washed away from the composite materials is negligible. At this point, only the substrate-stabilized co-catalyst species are left at the surface, which determined the number of washing-steps during the synthesis.

To complement this data, the real loadings of the solid samples were further confirmed directly in the solid-state using TXRF-spectroscopy. **Figure 10** shows the ideal vs. real loadings of the HER-active composite materials.

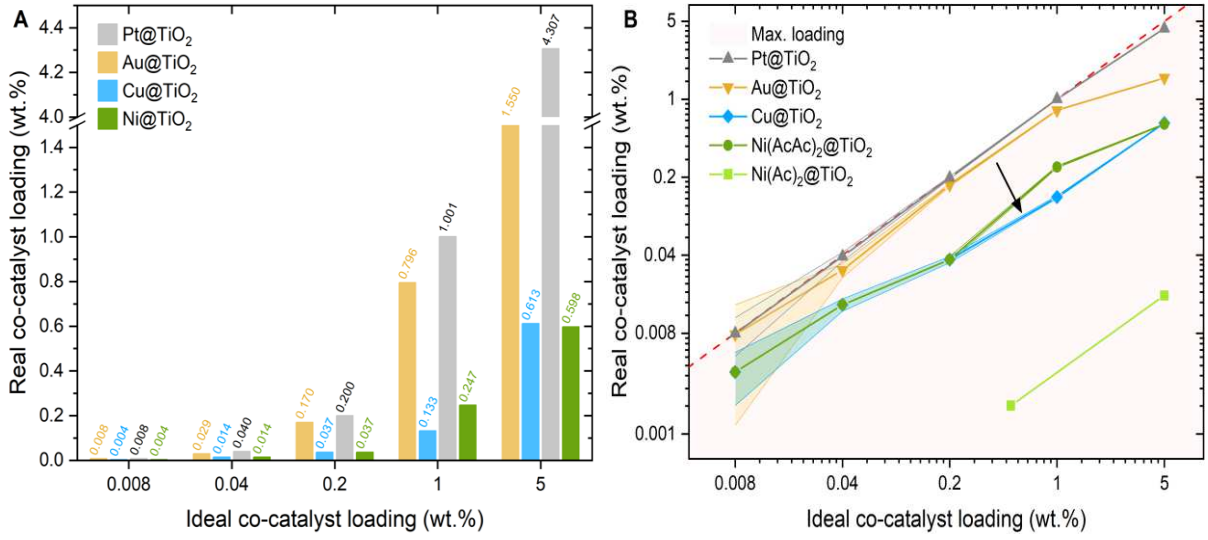

Figure 10 | **A**, Ideal vs real loadings of the different co-catalysts on TiO_2. The results were obtained through TXRF. **B**, double logarithmic scale and maximum ideal values represented by the red dashed line. Error bars are represented as colored areas above and below each point, if available. Some real loadings were below the detection limits and could not be detected.

The red dashed line in **Figure 10B** shows the maximum achievable loading values (ideal loadings). Deviating away from this value means that precursor species were removed from the TiO_2 during the washing process, resulting in lower loadings. Values above this line, especially for low loadings, represent an error due to the approaching of the detection limits of the equipment, or cross-contamination. Taking Au as an example (yellow), it can be understood that the real loadings were very close to the ideal values (proximity to the red dashed line), except for the highest loading, which was at around 1.5 wt.%, compared to 5 wt. that was aimed. The real loadings of Cu (blue) were, in comparison, further away from the ideal values and Ni loadings – when using the $Ni(Ac)_2$ precursor – show the strongest deviation from ideal values. This will be discussed further in the next section.

The data indicate that the impregnation process was less successful for the earth-abundant metals, Cu and Ni, where the real loadings varied strongly from the ideal values (see **Figure 10B**, black arrow). In contrast to that, the noble metals, Au and Pt, showed real loadings nearer to the ideal ones. This data suggests that Cu and Ni have a different adsorption/deposition mechanism than noble metals – probably due to weaker electrostatic interactions with the O-rich substrate surface – which would explain why their loadings were lower. Furthermore, detection limits need to be considered, especially for Ni, which was not detected at the lowest loadings. The reasons for this difference in adsorption will be discussed later in Section 6.2.3.

6.2.2. Precursor composition impact

In the case of nickel, two different precursors, nickel acetate and nickel acetylacetonate were investigated, since the one tested first, $Ni(Ac)_2{\cdot}4H_2O$, resulted in very low loadings and consequently showed practically zero HER-activity. Quantification of nickel in the washing solutions and in the solid samples using $Ni(Ac)_2{\cdot}4H_2O$ showed a maximum real loading of as low as 0.02 wt.% when the ideal value was supposed to be 5 wt.%. **Figure 11** shows that almost the entire precursor (99.6 %) added for the impregnation was found in the filtrate. In contrast to this, when $Ni(AcAc)_2$ was used for impregnation, a reasonably high loading value (similar to that of the comparable Cu system) could be achieved.

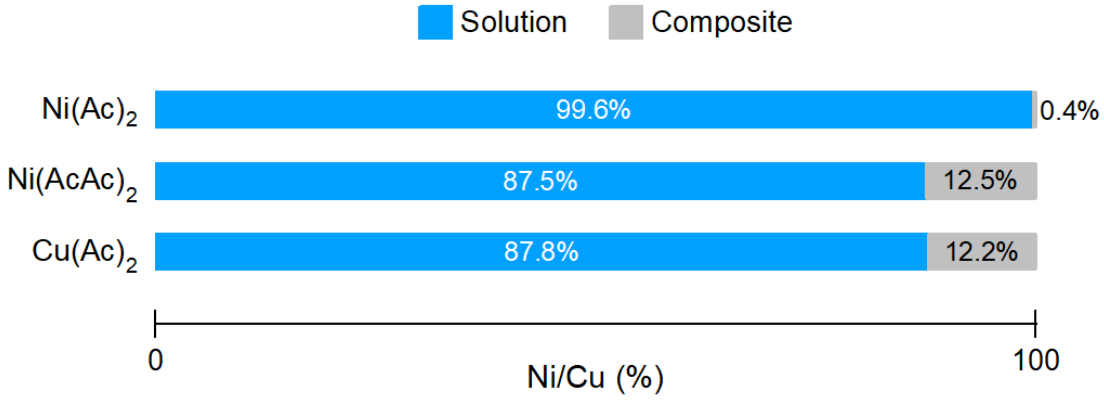

Figure 11 | Precursor metal species found in the solution (■) or on the solid (■) after the impregnation method for the 5/Ni@TiO_2 or 5/Cu@TiO_2 samples. 100 % refers to the whole amount of precursor added for this synthesis strategy.

The explanation to this difference in adsorption is that the complex formed in the aqueous solution of nickel acetate is structurally different from the one formed by nickel

acetylacetonate. $Ni(AcAc)_2$ is poorly soluble in water due to a stable trimer structure of its anhydrous solid form. In solution, it forms an octahedral complex, with two bidentate bonds from 2 acetylacetonate ligands in equatorial and 2 aqua ligands in axial positions, as shown in **Figure 12A**.[80] $Ni(Ac)_2 \cdot 4H_2O$, in turn, is highly soluble in water and forms an octahedral complex as well, but with 4 aqua ligands and only 2 monodentate-bounded acetate ligands, as shown in **Figure 12B**.[81]

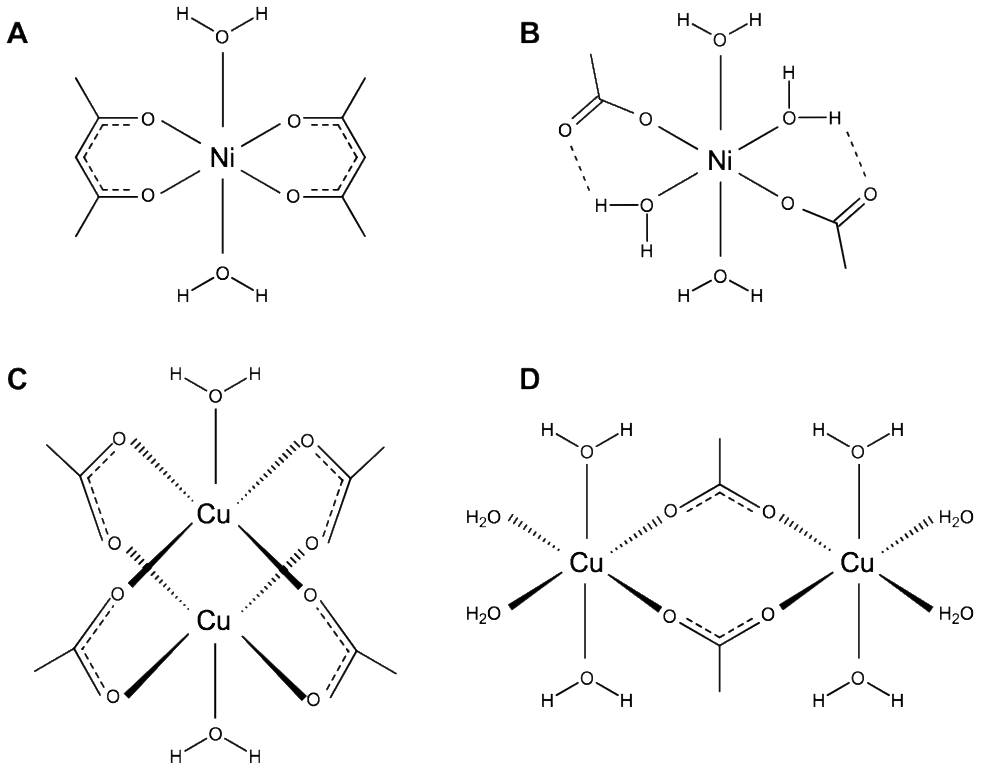

Figure 12 | Complexes built in aqueous solution by the precursors **A**, $[Ni(AcAc)_2(H_2O)_2]$. **B**, $[Ni(Ac)_2(H_2O)_4]$. **C**, binuclear lantern-structure of $Cu(Ac)_2 \cdot H_2O$ in solid-state **D**, lantern-structure of $Cu(Ac)_2$ in aqueous solution.

We assume that upon adsorption, both complexes anchor to the hydroxylated TiO_2 surface accompanied by partial ligand exchange. Here, however, it is important to consider the spectrochemical series that proposes that AcAc is a stronger ligand than Ac, while aqua ligands have an intermediate strength.[82] This suggests that the acetate can be more easily exchanged against an aqua ligand. Based on this assumption, it is likely that the adsorbed $Ni(Ac)_2$ will lose its Ac-ligands in the dynamic process and will be more prone to be washed away during the subsequent washing steps. The adsorbed $Ni(AcAc)_2$ complex, in comparison, is far less likely to lose its organic ligands so easily during washing due to its higher strength and the additional chelate effect of the bidentate binding. We thus suggest that the AcAc-ligands have a protecting effect against further ligand exchange with aqua-ligands and hence stabilize the adsorbed Ni-species better at the surface.

The choice of ligand thus plays an important role in defining the extent of the precursor adsorption, it is however not the only important factor. In fact, the data for $Cu(Ac)_2$ impregnation suggest that this compound does adsorb well despite the presence of the acetate in the composition. The complex structure of $Cu(Ac)_2 \cdot H_2O$ has been reported to have a binuclear nature, which is partially preserved in aqueous solutions.[83] Its lantern-type core is still composed of two Cu(II) central atoms, connected by four acetate bridges (see **Figure**

12C). Upon dissolution in water, aqua-ligands open up the lantern-structure with partial retention of bridging Ac-ligands, as shown in **Figure 12D**. As a result, the complex still holds its binuclear nature – in contrast to the mononuclear Ni acetate – which is likely to be preserved upon adsorption on TiO_2 surface. We suggest that this, along with the stronger bound bridging acetates, further stabilizes the Cu species during the washing steps. Hence, the precursor type and structure both have to be additionally considered as they have a great influence on the adsorption process, ultimate metal loadings and the resulting performance.

6.2.3. Effect of ambient light on the synthesis?

Absorption spectra acquired through DRS measurements help to elucidate on the nature of the impregnated co-catalyst species, because nanoparticles and ionic species – these can be potentially formed – often show distinct characteristic absorption features. Since the chosen precursors for the earth-abundant (Cu, Ni) and the noble metal (Au, Pt) systems were fundamentally different in their nature, we further needed to account for different adsorption and/or deposition processes. The noble metal precursors, based on chlorometallate acids ($HAuCl_4$ and H_2PtCl_6), were expected to have a strong tendency to photodeposit on the surface as nanoparticles even upon ambient light exposure. Earth-abundant precursors, in turn, were likely to be complexated by the hydroxyl-groups of the TiO_2's surface, staying in ionic form. These differences will be further discussed in the following sections.

The noble metals show very characteristic absorption spectra when present in nanoparticle form. Gold nanoparticles show an enhanced light absorption in the visible region, with a broad band peak centered at ~555 nm, which results from the localized surface plasmon resonance (LSPR) effect of Au NPs reported by Chen et al. and Shabman et al.[84,85] **Figure 13A** demonstrates DRS profiles of the as-prepared Au@TiO_2 composites that feature absorption max in the range between 548 and 569 nm, suggesting that generation of Au NPs takes place *in situ* during the impregnation. This is also reflected in the deep purple coloration of the composites, which gets more pronounced with increasing Au loadings. It is known that the formation of metallic nanoparticles in photocatalyst suspensions can take place via so-called photodepostion. To further elucidate on the reason for the Au NPs formation in our composites, experiments under dark conditions, described in **Section 5.4**, were performed. Indeed, the reference Au@TiO_2/dark composite powders obtained after filtration did not have the described coloration which confirms that the NP formation was indeed triggered by illumination and proceeded via photodeposition under ambient light.

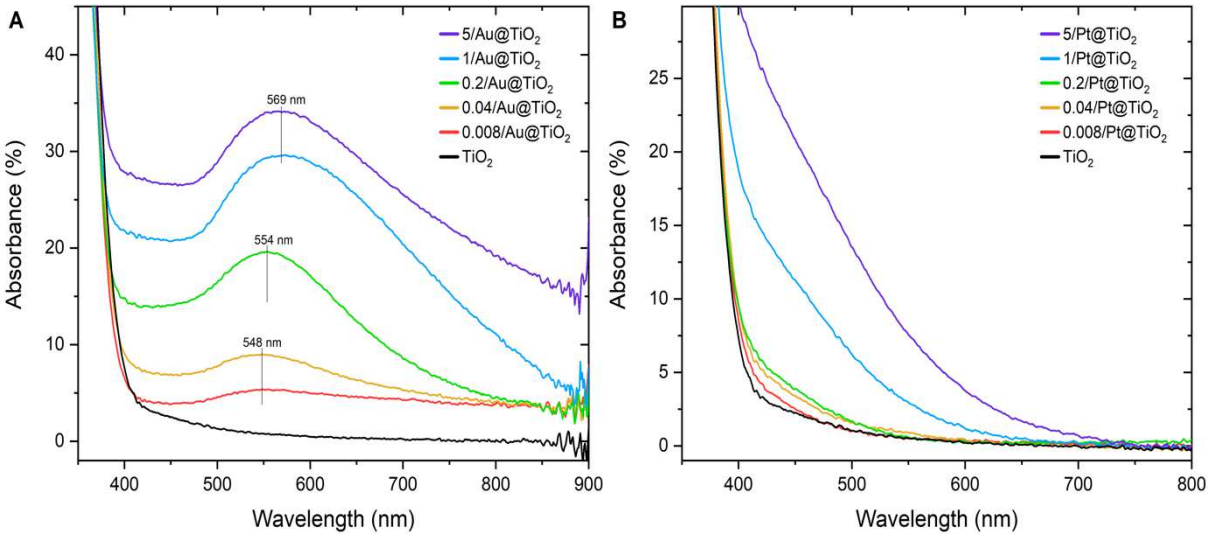

Figure 13 | DRS absorption spectra of **A**, Au@TiO_2 series. **B**, Pt@TiO_2 series

According to Shabnam et al., the absorption peak at 545 nm indicates particles between 5-20 nm. The size of the Au NPs can be obtained using the previous theoretical and experimental results of Haiss et al.[86] Comparing our results with Haiss's suggests 2 cases: *i)* large nanoparticles with diameters between d_L = 80-100 nm, or *ii)* small nanoparticles with diameters between d_S = 5-10 nm. **Table 2** summarizes the results determined through Haiss's calculations. Since the support's particle size is ~ 20 nm, it is not very likely to have such large Au NPs deposited on the surface of TiO_2. Therefore, we assume our particles follow case *ii)* and hence are in good agreement with Shabnam's observations and expected Au size obtained via photodeposition as reported elsewhere.[87] The impact of this photo-assisted deposition on photocatalytic performance will be discussed in detail in **Section 6.4****.**

Table 2 | Ratio of the absorbance of Au NPs at the surface plasmon resonance peak (A_{SPR}) to the absorbance at 450 nm (A_{450}) to determine the particles' diameter.

Sample	A_{450} (%)	A_{SPR} (%)	$\lambda_{SPR,\,max}$ (nm)	A_{SPR}/A_{450}	d_S (nm)	d_L (nm)
0.008/Au@TiO_2	3.8	5.3	548	1.40	7.5	80
0.04/Au@TiO_2	6.9	9.0	548	1.30	5.5	80
0.2/Au@TiO_2	14.1	19.6	554	1.39	7.3	86
1/Au@TiO_2	20.7	29.6	569	1.43	8.0	100
5/Au@TiO_2	26.6	34.0	569	1.28	5.3	100

The Pt@TiO_2 series, as seen in **Figure 13B**, shows a red shift of the absorption edge with increasing Pt loadings and an increased absorption in the visible range, but no LSPR effect in the visible spectrum due to d-d interband transitions, in line with literature.[84,88] This absorption behavior is common for Pt NPs and suggests that Pt is also being photodeposited onto the substrate's surface. The as-prepared composites exhibited an orange-yellow color, which decreased in intensity with decreasing loadings. This coloration can be explained through the increased absorption at the region 400-600 nm, which corresponds to violet-to-blue light. The material absorbs this light and appears to be of the complementary color.

Copper shows a rather different behavior. As reported by Qiu et al., Cu^{2+} complexes (be it aqua at 805 nm or acetate at 775 nm) absorb at higher wavelengths.[89] Moreover, the characteristic peak for Cu-NPs at 567 nm caused by SPR reported by Ramyadevi et al. was not found in the spectra of our Cu@TiO_2 composites.[90] As **Figure 14A** shows, the absorption of our Cu@TiO_2 composites corresponds to the expected absorption of Cu^{2+} complexes at higher wavelengths, which increases with increasing loadings, suggesting that Cu is likely to be present in the system in its Cu^{2+} form. An exception is found for the highest Cu loading, where a pronounced shoulder at 425 nm appears. This could be ascribed to the SPR-bands of Cu NPs.[91]

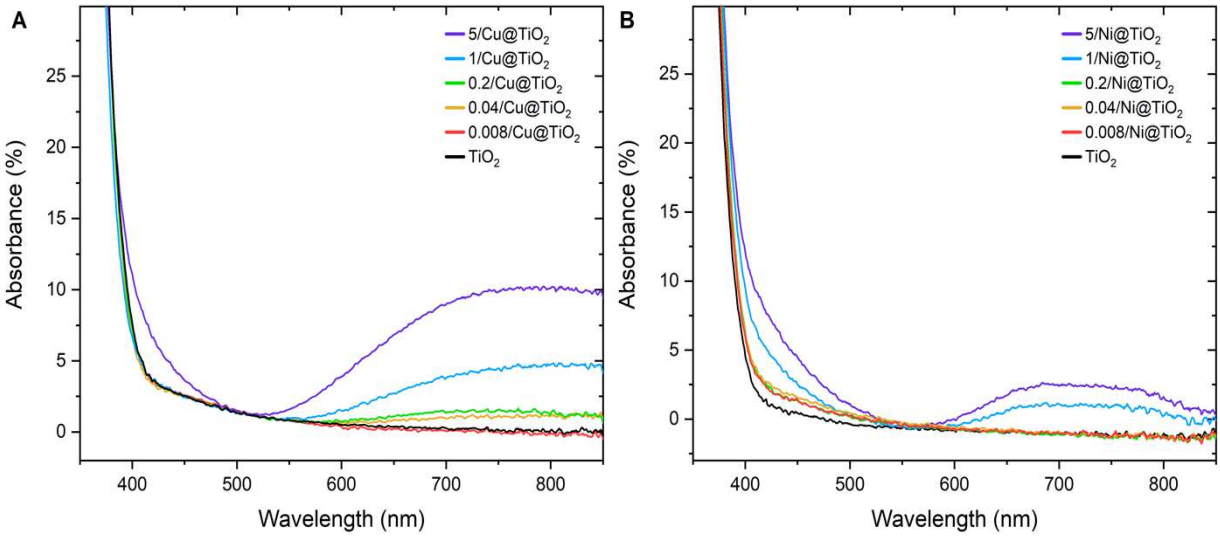

Figure 14 | DRS absorption spectra of **A**, Cu@TiO_2 series. **B**, Ni@TiO_2 series

The absorption spectra of the Ni@TiO_2 series shows a more complex situation. **Figure 14B** shows a red shift of the absorption edge of TiO_2 and the appearance of a shoulder at 410-520 nm, which gets more pronounced for higher loadings. This shift or shoulder has been previously observed by Chuang et al. upon Ni-doping of TiO_2.[92] Furthermore, Of et al. reported an absorption maximum of 395 nm for Ni NPs, which could also explain this shoulder.[93] The broad peak at around 590 to 860 nm should speak for Ni^{2+} species, which have been widely reported in literature and are known to appear in wavelengths between 600 and 840 nm.[80,94] Lewis et al. specifically report the absorption peak of $Ni(AcAc)_2$ at 644 nm.[95] Moreover, Zhu et al. reported a broad absorption band starting at 700 nm and onwards for Ni NPs of wide size distribution on rutile.[96] Hence, we assume that the Ni-systems produced through our impregnation process have a mixed nature, in which Ni-based nanoparticles (oxide or metallic) and ionic Ni-species may coexist, possibly driven by the heterogeneity of the TiO_2 surface structures.

In summary, the DRS data demonstrate that metallic nanoparticles are likely to be formed in the noble metal systems, however, we cannot exclude the additional existence of stabilized cationic precursor species. Cu@TiO_2 lack characteristic peaks for NPs (it may only be visible for the highest loading), which suggests the formation of mostly ionic species at the surface. The Ni@TiO_2 series, on the other hand, shows characteristic peaks for both, NPs and ionic species. For all systems, regardless of the structure and state of the generated co-catalysts, absorption increases with increasing co-catalyst loadings.

6.2.4. TEM-Images

The TEM-images for the 1/Pt@TiO_2 samples shown in **Figure 15A** and **B** clearly demonstrate the formation of Pt-nanoparticles with a diameter of 1-2 nm, homogeneously decorating the surface of TiO_2. Similarly sized NPs have been observed in previous reports by our group using the photodeposition method.[97] As seen in **Figure 15C** and **D**, the 1/Au@TiO_2 samples show larger NPs with a wider size distribution. Their diameters range from 5 to 13 nm and some NPs of up to 28 nm were also occasionally found. The Au NP size obtained for this sample through DRS in **Section 6.2.3** was of 8 nm, which goes well in line with the average size found from the micrographs. TEM-images for samples with lower loadings for both noble metals were also recorded (for 0.04/Au@TiO_2 and 0.04/Pt@TiO_2), but no co-catalyst NPs could be observed. This may indicate that sufficiently low co-catalyst concentration may indeed affect the final morphology and type of the generated co-catalyst species. Moreover, TEM images for 1/Au@TiO_2/PD and 1/Au@TiO_2/dark show that in both cases Au NPs are found with a similar size distribution of 5 – 10 nm (see **Appendix TEM** for further images).

As **Figure 15E** shows, TEM-images for the 5/Ni@TiO_2 sample show small foreign NPs between 2.2 and 2.5 nm decorating TiO_2 surface. Compared to the Au and Pt cases, these NPs were harder to find and they seemed to grow over time, which could be explained by the reduction of Ni^{2+} through the electron beam of the microscope. This goes in line with the conclusion of **Section 6.2.3**, in which a mixture of Ni NPs and cationic Ni species was suggested. For the 5/Cu@TiO_2 sample, no distinguishable NPs could be found, as exemplarily shown in **Figure 15F**. At best, a thin layer can be seen covering some anatase NPs. Hence, we assume that Cu stayed in a rather cationic form as Cu^{2+} or built very small surface-decorating clusters, not distinguishable with this instrument's resolution.

From TEM image analysis, we confirm that noble metal systems indeed formed NPs at rather high loadings. When going towards lower loadings, no NPs could be observed anymore, which could align well with the intended "isolation" strategy. Earth-abundant systems behave differently. In the case of Ni, in line with the DRS data, TEM also indicates the formation of small NPs. For the latter Cu@TiO_2 case, we did not observe any surface-decoration.

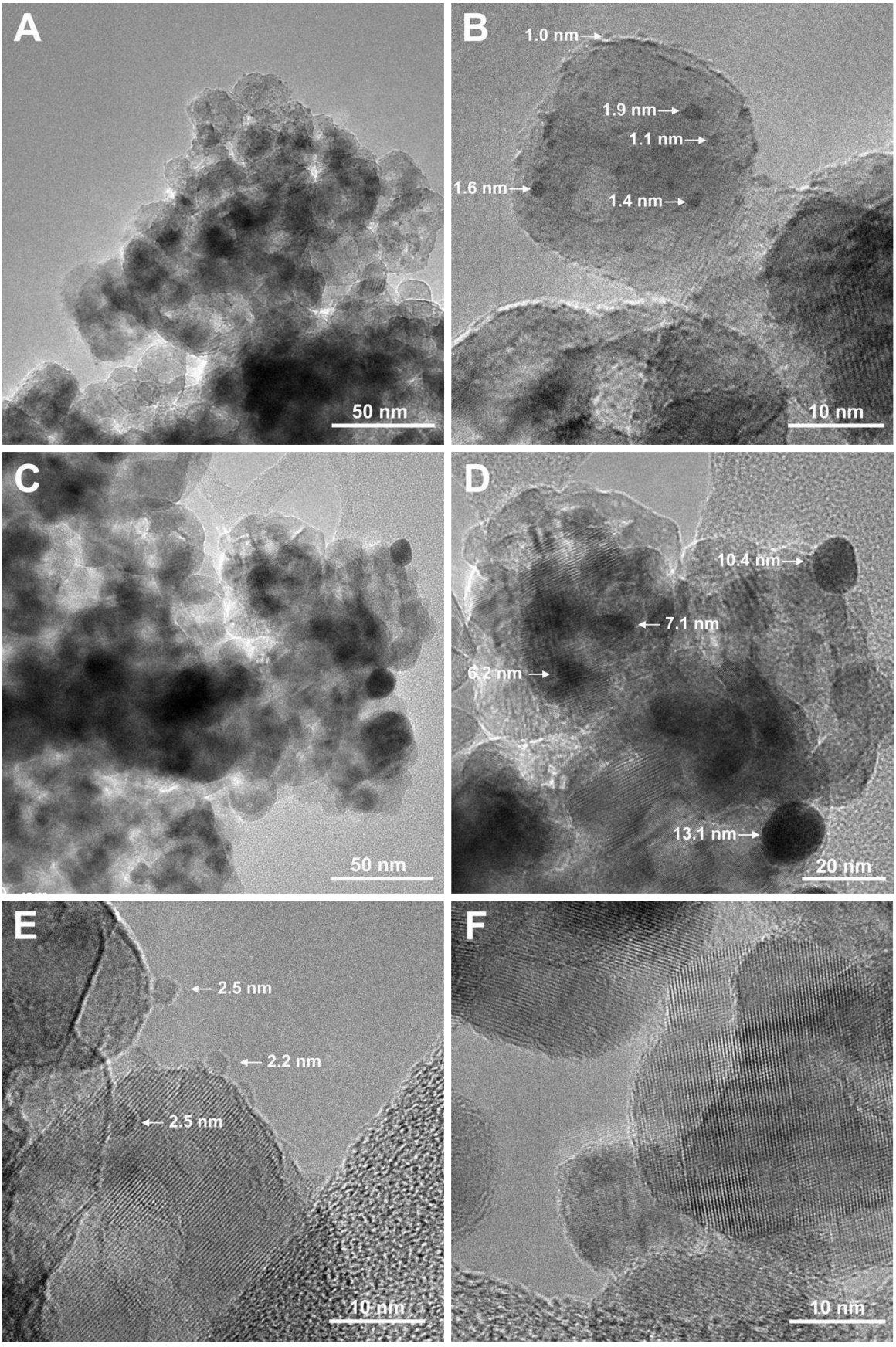

Figure 15 | TEM images for different composite materials. **A**, **B**, 1/Pt@TiO_2 at different magnifications. **C**, **D**, 1/Au@TiO_2 at different magnifications. **E**, 5/Ni@TiO_2 and **F**, 5/Cu@TiO_2.

6.3. Co-catalysts on PO_4-modified TiO_2 – single-sites or nanoparticles?

To further promote the stabilization of single-sites, composite materials were prepared using a phosphate modified substrate (synthetic details in **Section 5.1** and **Section 5.2**). The increased surface charge of this substrate should not only improve the adsorption process but is also believed to favor single-site formation due to stronger electrostatic interactions at the surface. Working synergistically with the isolation strategy described in **Section 6.2**, PO_4/TiO_2 should thus facilitate adsorption of the precursor species and prevent the active sites to interact with each other and/or to grow to larger clusters, resulting in more isolated sites and/or smaller clusters.[98] The same precursor concentration range between 0.008 and 5 wt. % was used following the identical impregnation-washing procedure as for the bare TiO_2.

The use of the PO_4 modification, however, implied that additional factors had to be considered. As previous reports show, the direct hole oxidation pathway can be suppressed through this modification, which in our case can hinder the charge transfer between co-catalyst species and TiO_2.[77,99] This, in turn, can affect the photodeposition of noble metal nanoparticles during the wet-impregnation synthesis that we observed before, which is a process dependent on the electron transfer from TiO_2 to the precursor. The phosphate groups block this electron transfer, resulting in fewer/smaller NPs formed, which can be confirmed through loadings determination and loading dependent HER experiments. Lower loadings for noble metals would speak for a declined nanoparticle deposition.

For the earth-abundant systems, Cu and Ni, the adsorption process does not involve a charge transfer mechanism with subsequent reduction of the precursor species, as our data in **Section 6.2.3** suggest. In contrast, we assume that ionic species are electrostatically attracted to the surface, which is why the increased negative surface charge of PO_4/TiO_2 should facilitate the anchoring of the positively charged metal-cations.

Moreover, the slower interfacial charge transfer dynamics caused by this modification will become relevant during the HER-experiments. Blocking the extraction of the photo-generated charge carriers (electrons and holes) at the surface of TiO_2 is likely to affect catalytic performances of the composites greatly. Suppressing the direct hole oxidation pathway results in a slower consumption of the sacrificial agent, MeOH. The holes, not being extracted efficiently, are now able to recombine with the electrons needed for the H^+ reduction reaction more effectively. Interfacial charge transfer processes are usually rate-limiting because they are slower (10 ps to 100 µs) than charge trapping (50 fs to 50 ps) or recombination (1 ps to >20 ns) processes.[20]

Hence, the PO_4 modification, while potentially able to promote the formation and stabilization of increased loadings of single-site species, might as well result in slower charge transfer dynamics during catalytic experiments and so, overall lower HER-rates.

6.3.1. TXRF in solid phase

The quantitative results of the solid-phase TXRF-analysis confirmed the enhanced loadings for Cu and Ni in the case of PO_4/TiO_2 substrate, especially when high loadings were originally desired. As for Pt and Au, this modification had no major effect on the real loadings except for the highest values, which showed a decrease. **Figure 16** shows the comparison of both substrates for all the studied co-catalysts.

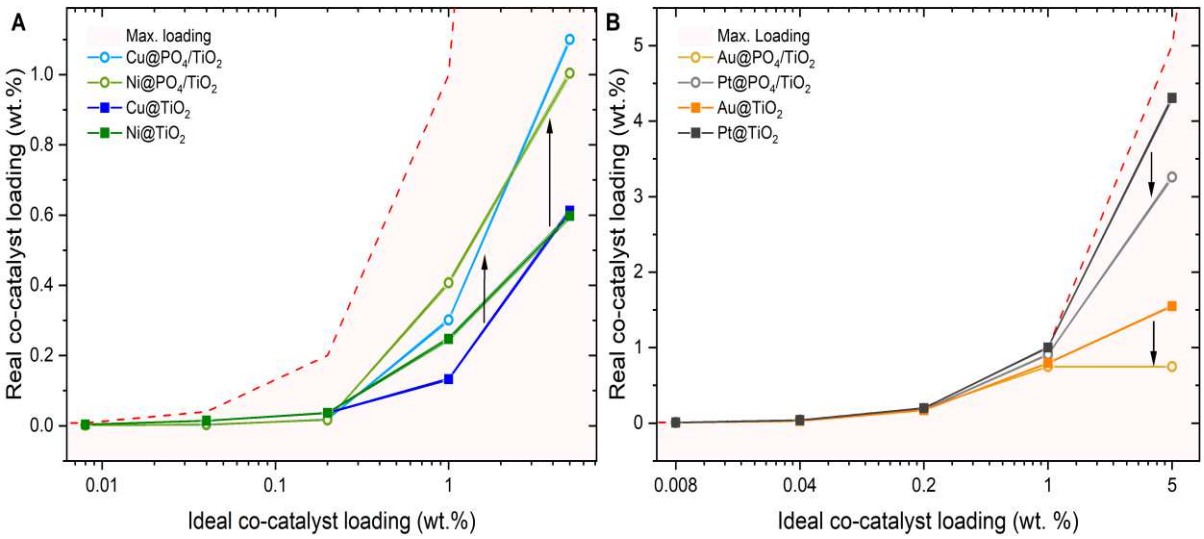

Figure 16 | Comparison of ideal vs. real loadings of the different HER-active co-catalysts for **A**, Earth-abundant systems on bare TiO_2 and PO_4/TiO_2. **B**, Noble metal systems on bare TiO_2 and PO_4/TiO_2. Data acquired through TXRF.

This further strengthens the hypothesis that the cationic earth-abundant species Cu^{2+} and Ni^{2+} are better adsorbed due to the more negative surface charge of the PO_4/TiO_2 support.

For the chlorometallate acids, which in solution are anionic species in the form of $[PtCl_6]^{2-}$ and $[AuCl_4]^{1-}$, the more negative surface charge of this substrate is counter-productive because it might repel these precursor species. Moreover, the deposition process likely involves both, adsorption via ion exchange and photo-assisted reduction by TiO_2 resulting in the deposition of metal nanoparticles. However, ionic and metallic species can coexist in the composite material. There is a slight influence of the phosphate modification towards lower loadings of noble metals, probably because of repulsion from the negatively charged surface and negative ions in the solution but also a reduced charge transfer, caused by the phosphate layer.

6.4. Hydrogen Evolution Reaction

This section will look into the catalytic performance of the as-prepared composite materials. The selected reaction to evaluate our systems was the H_2 evolution reaction (HER), because of its industrial relevance, good reproducibility, and comparability of our results with existing literature.

In a usual HER experiment, our online product detection system renders real-time H_2 evolution rates measured in situ in the gas flow. After waiting for a stable baseline signal (see Section 4.3) the UV-light (365 nm) was turned on at minute t = 5 min (see **Figure 17**). The delay in H_2 evolution, as well as the gradually increasing HER rates within the first 10 minutes, are both related to the reactor design and do not suggest that a certain catalyst activation takes place. Typically, HER rate reaches a plateau after ca. 15 min, which corresponds to a stable H_2 evolution rate. In a typical experiment, illumination was conducted for 30 minutes, after which time the test was terminated. The activity values were extracted from the HER rates reached after 30 minutes.

Figure 17A exemplarily demonstrates how the rates of H_2 evolution decreased with decreased ideal loadings of Cu or Ni in the respective @TiO_2 series. However, noble-metal-based

composites shown in **Figure 17B** indicate an optimal co-catalyst loading value at around 1 wt.%. Lower or unchanged HER rates achieved at higher loadings (e.g. 5 wt. % of Pt and Au) can, in this case, be attributed to the light-blocking effects of the excessive amounts of the surface-anchored nanoparticles that impede TiO_2 absorption.

Another important observation is that the Ni-systems do not reach a stable H_2 evolution rate after 30 min, but it continues to increase over time as shown in **Figure 17A** (green curves). The reason for the dynamic nature of Ni is a co-catalyst in-situ activation process, in which Ni^{2+} turns metallic upon illumination, becoming more active for the HER, as previously reported by our group.[100] Over time, the H_2 evolution rate for the Ni-systems is expected to increase linearly, which would result in a higher performance of the catalyst. This effect can be observed even for the lowest loadings. Due to the time constraint of this work, long run HER-experiments could not be performed, but are promising for further investigations.

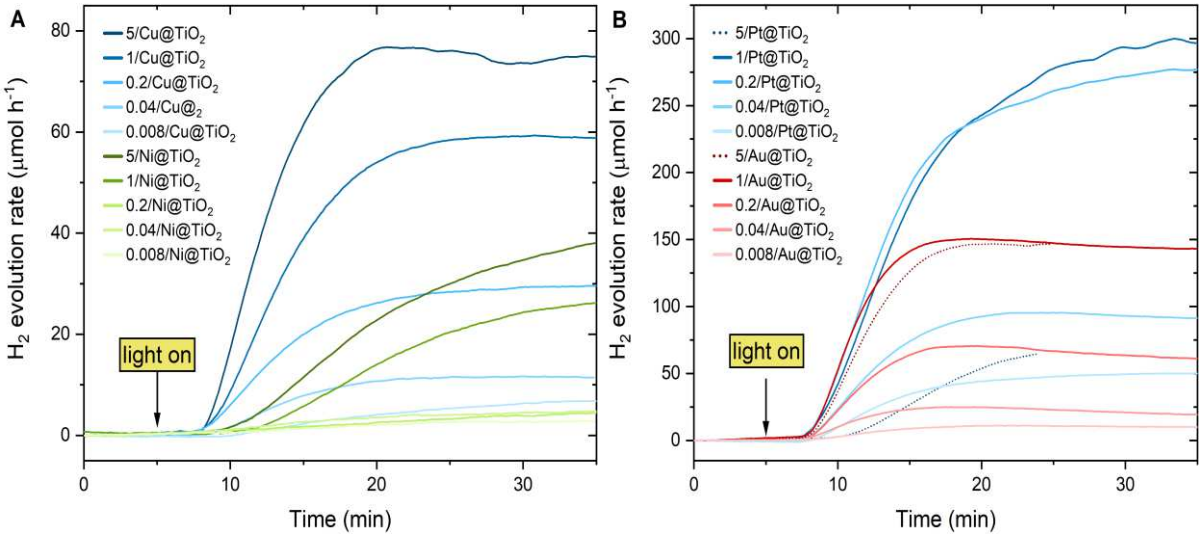

Figure 17 | Exemplary HER-experiments results for **A**, Earth-abundant systems and **B**, Noble metal systems.

Since the main motivation of this work was to evaluate various factors (site isolation and substrate modification) on the success of single-site co-catalyst formation and ultimately enhanced catalytical performance, the following sections will discuss these data in different contexts and for different systems. The turnover frequency (TOF) concept, described in **Section 4.3.1**, will gain relevance since it does not only account for the overall HER-activity of a certain composite material but relates the amount of H_2 produced to the amount of co-catalyst involved in the catalytic reaction. We assume that an exponential increase of TOFs for samples with low co-catalyst loadings will speak for single-sites formation and stabilization.

6.4.1 Models for data analysis

Mathematical models to predict and explain experimental HER data were developed in order to simulate the evolution of the co-catalyst species and thus gain more insights into the potential single-site stabilization following our isolation strategy. In other words, the models should help to understand the behavior of the photocatalysts by fitting our data points to these models and hence unravel the central question: “Is the isolation strategy exclusively reducing the amount of co-catalyst particle-like species or is it changing their size, shape and

morphology, approaching smaller species?" These two options are represented graphically in **Figure 18**.

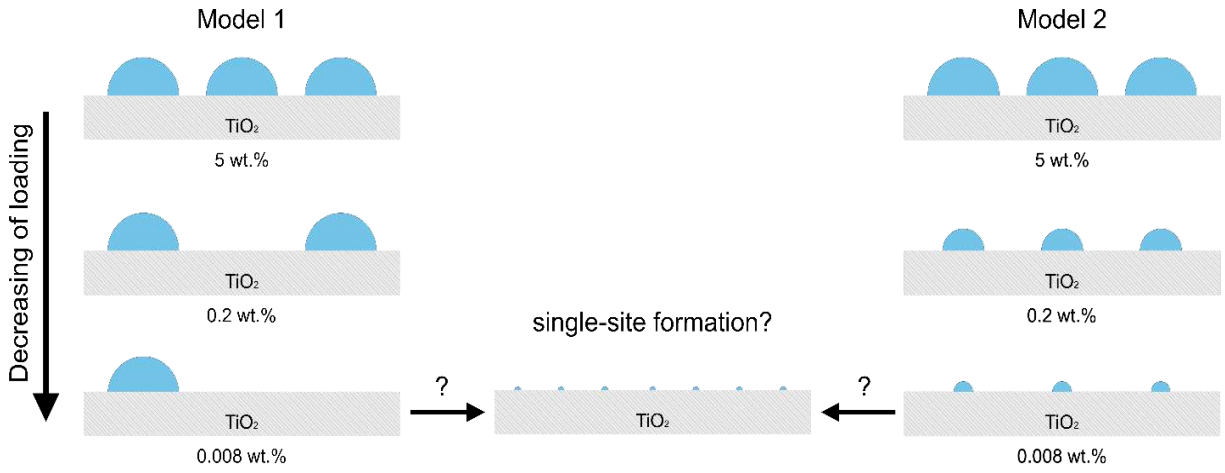

Figure 18 | Graphical representation of the modelling idea approaching lower loadings. **A**, **Model 1**: reduction of same-sized co-catalyst particles. **B**, **Model 2**: size reduction of co-catalyst particles.

General assumptions that underline these models in the first place are: *i)* the HER is not limited by photons: the amount of light and thus the number of photo-generated charge carriers (electrons and holes) is sufficient for any amount of catalytic conversions, that is, the reaction is limited by the catalyst's performance, and *ii)* shape, location or surrounding of the catalytic site does not influence its intrinsic activity, implying that the performance of a single-site atom or an atom at the surface of a co-catalyst's NP is the same.

Model 1 describes the behavior where the shape/morphology of the co-catalyst does not change upon decreasing the amount of precursor deposited. A lower catalyst deposition merely results in a proportionally lower number of catalytically active sites (e.g. surface atoms of NPs). Based on this model, we would expect **linearity** ($y = x$) when plotting co-catalyst loading vs. overall HER-activity and a **constant** trend for loading vs. TOF ($y = a$), as shown in **Figure 19A**.

Model 2 describes the scenario in which the co-catalyst size/shape changes upon a decrease of co-catalyst loading. In this case, going towards lower loadings would diminish the size of the co-catalyst NPs. Supposing the NPs are perfect spheres, the relationship between their surface and volume follows $S \sim \sqrt[3]{V^2}$. The number of surface atoms (e.g. number of atoms involved in the catalytic reaction, i.e. HER) is directly proportional to S, and the loading (total amount of atoms) is directly proportional to V. Following these assumptions, upon reducing the loading, we would expect the same non-linear proportionality, i.e. the co-catalyst loading vs. HER-activity would be proportional to $(x)^{2/3}$. The loading vs. TOF would follow the proportionality of $(x)^{-1/3}$, as shown in **Figure 19B**.

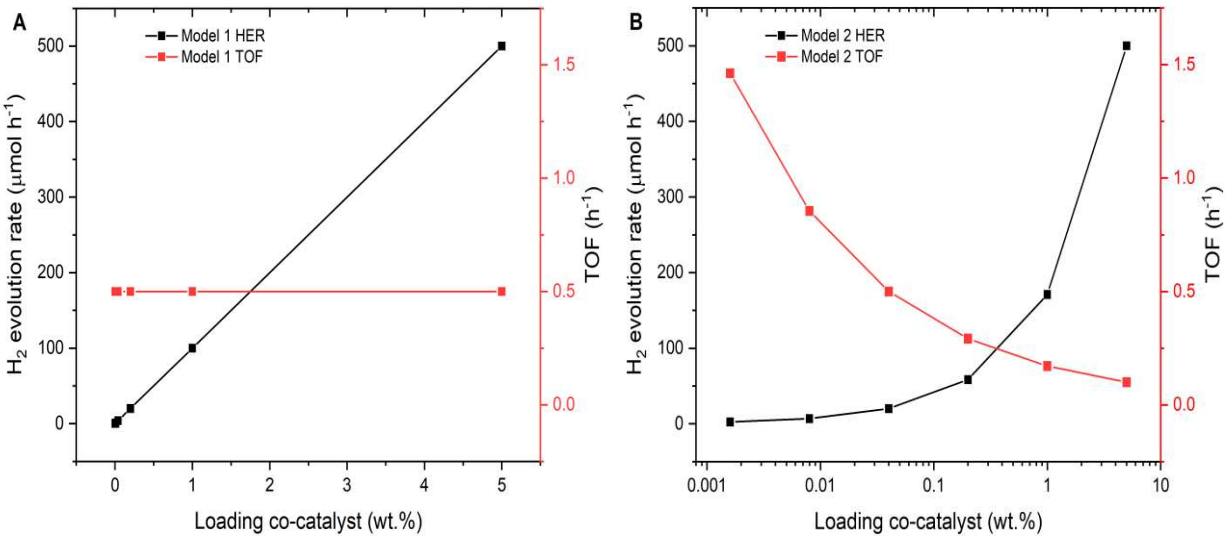

Figure 19 | Proportionality behavior of curves when plotting arbitrary values for **A**, **Model 1**: showing a linear slope ($y = x$) for the co-catalyst loading vs. the H_2 evolution rate (black) and a constant ($y = a$) for the co-catalyst loading vs. the TOF (red). **B**, **Model 2**: showing a proportionality of $(x)^{2/3}$ for the co-catalyst loading vs. the H_2 evolution rate (black) and a proportionality of $(x)^{-1/3}$ for the co-catalyst loading vs. the TOF (red).

Comparing our data to these models and observing similar behaviors or strong deviations from them should expand the understanding of the experimental trends. Hence, we would be able to qualitatively demonstrate if a size/morphology change takes place upon lowering the loadings (similarity of data trends to **Model 2**) or not. For detailed calculations and examples on the use of the models, see **Appendix Models**.

6.4.2. Noble metal series: activity trends for both substrates

By plotting the real loadings of the Pt and Au-based composites against the maximum HER-activity values, **Figure 20A** and **C** are obtained. Note that the co-catalyst loadings (X-axes) are presented on a logarithmic scale. The overall H_2 production in µmol h^{-1} can be appreciated in this way for the different series of as-prepared composite materials. For both metals, the graphs show that the more co-catalyst used, the more hydrogen will be produced. This tendency is less pronounced for the Au@PO_4/TiO_2 series, as expected by the lower HER activity of Au, due to the charge blocking effect discussed previously.[77,99] However, when the activity is normalized per amount of catalytically active species (i.e. the as-impregnated co-catalysts), **Figure 20B** and **D** can be constructed. These figures demonstrate that the TOF values (moles of produced H_2 per moles of co-catalyst per hour) grow strongly when lower co-catalyst loadings are used. The most suited model trends are also included in these graphs, in which the deviations from the model-derived "expected" TOF values are shown with arrows and numerical factors.

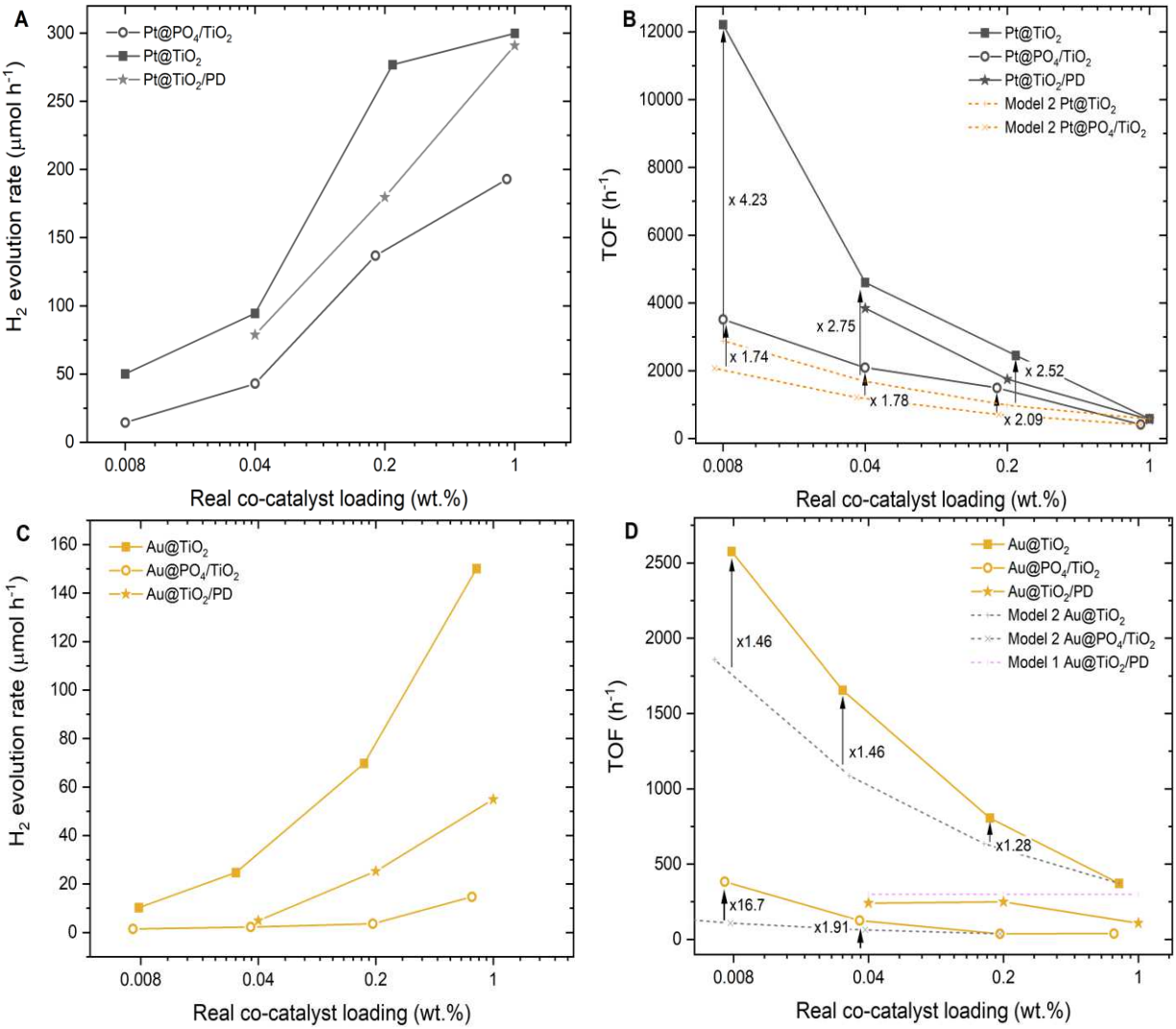

Figure 20 | **A**, Real Pt loadings against maximum HER-activity values. **B**, Real Pt loadings against maximum HER-activity per mmol co-catalyst (TOF). **C**, Real Au loadings against maximum HER-activity values. **D**, Real Au loadings against maximum HER-activity per mmol co-catalyst (TOF).

The overall data suggest that the use of the PO_4/TiO_2 substrate rendered lower absolute H_2 evolution rates for both noble metal systems. The reason for this is that the PO_4 groups may block the charge transfer process between TiO_2 and the co-catalyst, as previous reports have suggested.[77,99] This not only causes lower loadings of the deposited noble metals, but more importantly, hinders the charge transfer dynamics of the photocatalytic reaction. Moreover, the interfacial charge extraction (of holes) between TiO_2 and other reactants in the solution, e.g. the sacrificial agent, MeOH, will also be diminished, resulting in a decreased HER-performance. These results align well with the discussion and expectations of Section 6.3.

Next, following the individual trends from the **Figure 20B:** in the case of Pt, when going towards low co-catalyst loadings, the TOFs increase strongly and a non-linearly for TiO_2 and PO_4/TiO_2 substrates can be observed. This implies that the evolution of the co-catalyst species in both cases rather follows the **Model 2** prediction (i.e. involving a size/morphology change). Importantly, the relative increase of TOF is in the same order of magnitude for both substrates, which suggests that the phosphate modification did not affect the formation and state of Pt-based co-catalyst species. This can be explained due to the strong tendency of Pt to form NPs

under the conditions of a photocatalytic reaction on TiO_2, which apparently has not been strongly affected by the presence of PO_4 groups.

The trend obtained for the Pt@TiO_2/PD series in **Figure 20A** rather corresponds to a linear dependency with a non-zero slope. Thus, the TOF vs. loading trend is not following either **Model 1** or **2**. We assume that this TOF increase is not related to a change in morphology but can rather be related to another effect. As mentioned before, Pt is known for its strong tendency to form same-sized NPs via photodeposition. It has been proposed that a single Pt NP could act as a reduction site for a single TiO_2 nanoparticle of a few dozens of nanometers.[101] We assume that such a case would result in an utmost effective charge-extraction pathway. When going towards lower loadings (0.04 wt.% in this case), we might end up with such a scenario, where only one Pt NP decorates every single TiO_2 NP. This enhanced charge extraction through one co-catalyst NP might explain the deviation from the expected **Model 1** and the relatively higher TOF-values.

In the case of Au, shown in **Figure 20C** and **D** we see a similar trend: TOF values also boost when approaching the lowest loadings, in line with the prediction of **Model 2**. However, here we can see a strong influence of the phosphate modification: it can be noticed that the TOF for the lowest (0.072 wt.%) loading is **16.7** times higher than the value predicted by the model. This is the highest factor (greatest deviation from the prediction) among all investigated systems, which implies an even stronger change in the Au's size/morphology at the lowest loadings as a possible factor for the enhanced activity per site. Such a strong deviation from the prediction is not observed for the bare TiO_2, so we assume that the phosphate modification indeed helped to stabilize Au single-sites when sufficiently low overall Au loadings were used.

Interestingly, the TOF trend (**Figure 20D**, stars) of the reference PD-experiments for Au system differs clearly from that obtained for Pt, as the linearity in the TOF values can be observed when going towards low loadings. In fact, this trend of Au@TiO_2/PD follows closely the **Model 1** prediction (purple dashed line), which states that the shape and morphology of the co-catalyst are not being changed when decreasing the co-catalysts loading, suggesting that PD yields 5.8 – 10.6 nm Au NPs observed in TEM-images (See **Appendix TEM**) acquired for 1/Au@TiO_2/PD. The result and the correlation with Model 1 suggest that only the number of such Au co-catalyst NPs is decreasing at lower loadings, while their morphology stays unaffected.

Two main conclusions can be drawn from these results. First, both series of Au and Pt on both substrates follow **Model 2**, while the photodeposited samples for Au follow **Model 1** and Pt something between the two models. Hence, the isolation strategy did affect the morphology of the noble metal co-catalysts and promoted the formation of smaller species, enhancing the atom utilization efficiency at low loadings, especially for Pt.

Secondly, the PO_4 modification was successful for the lowest Au loadings, delivering the highest relative increase in the TOF-value. This speaks for the stabilization of smaller or more active species. Probably, there is a need of a more homogeneous (full coverage with PO_4 groups) or more specific surface modification to promote the stabilization of smaller species at higher Au loadings. In the case of Pt, the PO_4 modification was not advantageous.

Additionally, we need to account for other factors that might influence the TOF values as well, e.g. the number of Pt NPs per TiO_2 particle, light-blocking effects of too many particles and SPR-effects. The developed models, although simple and somehow limited in their parameters, seem to be able to describe these systems properly.

6.4.3. Noble metal series: Influence of light

Based on our previous data, which indicate that light plays a major role driving the deposition of noble metal precursor species and triggers a reduction of the co-catalyst precursor species into larger NPs, synthesis under dark conditions (**Section 5.4**) and *in-situ* photodeposition HER-experiments (**Section 5.5**) were carried out for these systems as well. As already discussed in **Section 6.2.1**, real loadings generally vary from ideal ones. The loss of added precursor species during the impregnation process is, however, less pronounced for the noble metal series, where real loadings almost reach the ideal values, implying that almost all of the precursor species are deposited during the impregnation under ambient light. This can, however, be different for the samples prepared under dark conditions, where light-induced deposition of particles is hindered and only a fraction of the precursor may stay adsorbed on the TiO_2 surface after multiple washing steps. For the photodeposition experiments, the entire amount of added precursor is taking part in the photocatalytic reaction and cannot be recovered, which is why ideal loadings are taken as real ones for the following considerations. As expected, the PD-experiments result in metal NPs (d_{Pt} ~ 2.5 nm and d_{Au} ~ 8.5 nm) decorating TiO_2 surface, as TEM-micrographs confirm (see **Appendix TEM**).

Figure 21 compares the performances in terms of TOFs of the same ideal loadings of noble metals (same colors) prepared under different light conditions to directly evaluate which method worked best. It is evident from **Figure 21A** that the Pt@TiO_2 performance profits from a lack of light during the impregnation synthesis. Synthesis in the dark is advantageous, probably because the amount of chloroplatinic acid adsorbed on titania during the impregnation gets effectively reduced during synthesis and subsequent washing steps, allowing only few and stable precursor species to stay at the surface. This remaining H_2PtCl_6 precursor is likely to generate Pt nanoclusters during the drying process (temperature-induced reduction) or during the photocatalytic reaction, which are much smaller than the NPs our previous reports have shown.[97] Moreover, the orange-yellow coloration of these samples (see **Section 6.2.3**) was not as strong as for the ones synthesized via the normal synthesis. In fact, the loading amounts (estimated through TXRF) of the dark samples was about 10 times less than for the normal impregnation. The H_2 evolution rates of Pt@TiO_2/dark samples were only 2.5 to 5 times less than for the normal series. Thus, the atom utilization efficiency was increased and the catalytic performance enhanced. The TOF of the sample prepared via *in-situ* photodeposition is generally lower than that of the Pt@TiO_2 composites prepared via standard impregnation. This might be attributed to the following: during the PD-experiment, the precursor forms 2-3 nm Pt NPs.[97,102] In turn, the wet-impregnation process might facilitate the formation of other structures, like better isolated Pt species or smaller NPs, similar to the samples prepared under dark conditions. This speaks for an optimal synthesis pathway using the dark impregnation method vs. the well-established *in-situ* photodeposition due to the higher H_2 evolution rates per co-catalyst amount observed herein.

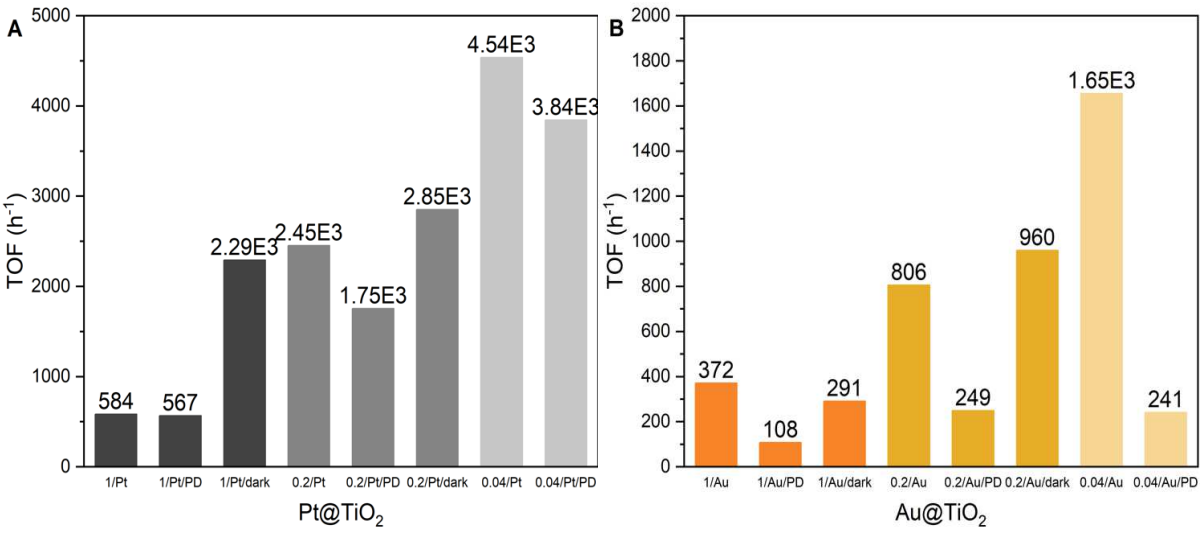

Figure 21 | Comparison of different synthesis methods for composite materials altering the light conditions (normal, photodeposition (PD) or dark) against TOF-values (H_2 evolution per co-catalyst amount per hour) for **A**, Pt@TiO_2 systems and **B**, Au@TiO_2 systems. TOF-values are also shown on top of each bar.

Figure 21B shows a very different set of results that were obtained for the Au-based systems: the normal composites have now much higher TOF values compared to the photodeposited samples. It is known that Au photodeposition typically results in the formation of Au NPs, which will only have a limited number of surface and triple-phase boundary atoms responsible for HER performance.[85] The close-to-constant TON trend already discussed in **Figure 20D** further confirms that Au particles in the same shape and size are being created independently on the precursor amount. The much higher TOF values obtained for the standard Au@TiO_2 samples suggest that the impregnation procedure may indeed facilitate the formation of smaller clusters or even single-sites during the synthesis. Considering the enhanced TOFs of the 0.2/Au/dark samples, synthesis under dark deviate more strongly from the PD-trend thus suggesting that the tendency of forming stable ionic or smaller Au-NP species is apparently even stronger when photodeposition is hindered. Dark synthesis for Au might work as follows: ionic species are adsorbed by TiO_2, whereby no color change is observed. After drying, they change their color to purple, due to a heat-induced reduction that might form some NPs, which are responsible for the deep purple coloration already discussed in **Section 6.2.3**. Since forming large ~ 8 nm NPs is more difficult than the well-known 2 nm Pt NPs, some Au-species might still stay ionic and more isolated, since our impregnation method restricts the migration of surface-adsorbed cations. A small amount of NPs account for the coloration, but we assume that they should be smaller than 8 nm. DRS theoretical calculations and TEM images (see **Appendix DRS** and **Appendix TEM**) confirm that the Au NPs in the 1/Au@TiO_2/dark samples were indeed smaller d_{DRS} = 5 nm and d_{TEM} = 4.2-9.5 nm than the ones found for the normal synthesis. Moreover, the large 28 nm NPs found in the normal synthesis (see **Section 6.2.4**) could not be found in the dark samples. Hence, the suppression of the photodeposition mechanism seems advantageous and should be studied further in the future.

In conclusion, light has a high impact on the noble metals deposition because of the fundamental mechanism of photodeposition that Pt and Au have. Regardless of the metal, dark conditions suppress the light-induced deposition, changing the size/morphology of the NPs to smaller sizes or even nanoclusters that show higher activities per site. Since Pt readily forms smaller particles (2-3 nm) under normal conditions, we assume that this particle formation is happening at even smaller sizes when using dark conditions. In contrast,

Au@TiO_2 build larger NPs under normal impregnation conditions, which is harder to achieve without the assistance of ambient light. Hence, the so-prepared Au composites might render more ionic, smaller and more active Au-sites.

6.4.4. Earth-abundant series: activity trends for both substrates

Analogously to the noble metal systems, **Figure 22** shows the relationships between the real loadings of earth-abundant metals and the maximum H_2 evolution rates and TOF-values for Cu and Ni. **Figure 22A** and **C** show that the PO_4 modification rendered lower overall activities for both metal series, even though their loadings were higher than for the normal support. This is attributed to the aforementioned reason, discussed in **Section 6.3**: the charge-blocking effect induced by PO_4 groups hinders the ultimate photocatalytic reaction. Interestingly, upon reaching lower loadings, this effect is less pronounced.

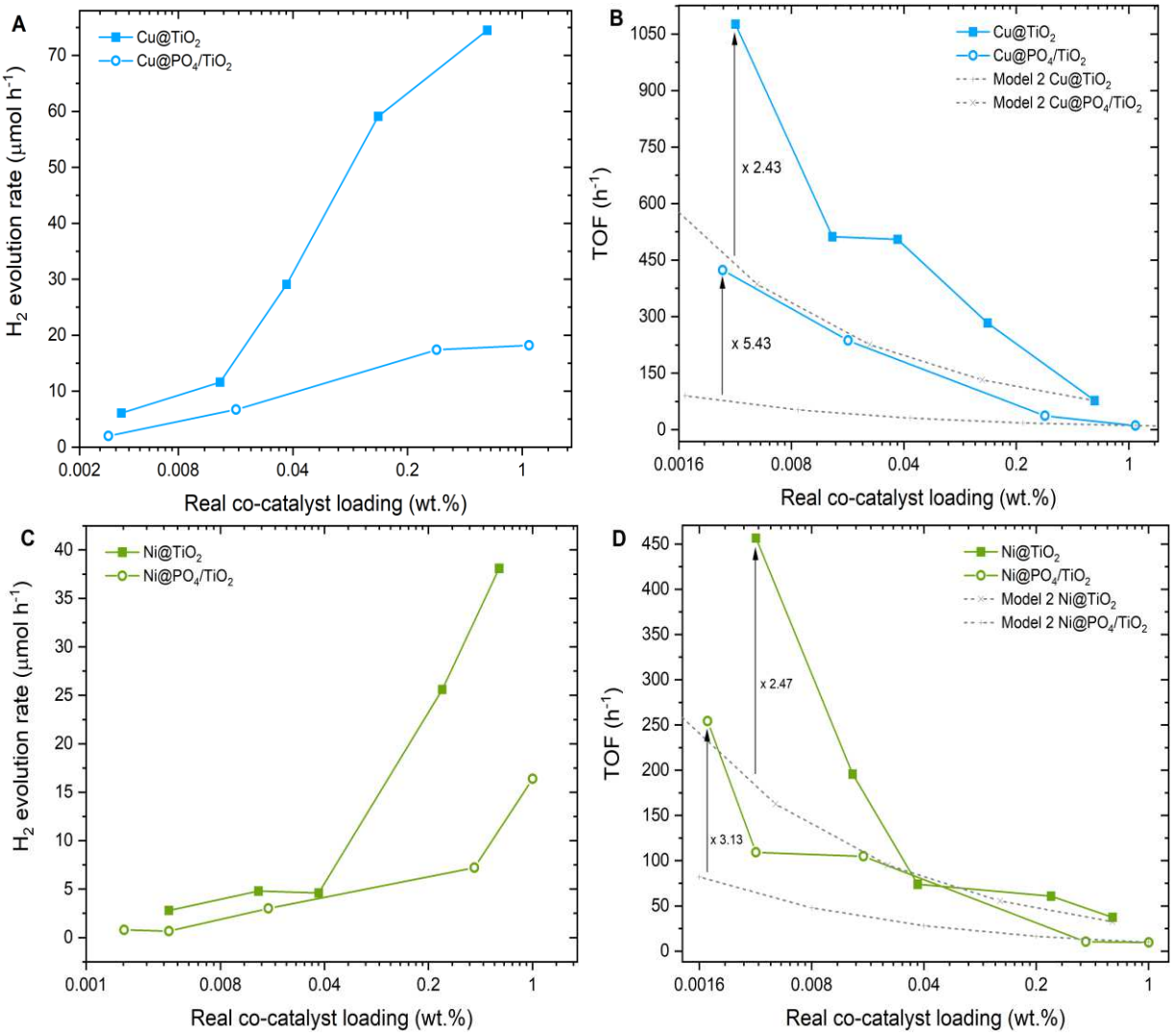

Figure 22 | **A**, Real Cu loadings against maximum HER-activity values. **B**, Real Cu loadings against maximum HER-activity per mmol co-catalyst (TOF). **C**, Real Ni loadings against maximum HER-activity values. **D**, Real Ni loadings against maximum HER-activity per mmol co-catalyst (TOF).

The general trend seen from **Figure 22B** and **D** is that lower loadings – as was already observed for the noble metal systems – also result in a major increase in the TOF-values, regardless of the substrate. This can also be attributed to the enhanced atom utilization efficiency discussed before. However, the trends do not follow **Model 2** as closely as in the case of the noble metals: the stronger increase of TOF-values for low loadings speaks for a strong morphology change and a stabilization of eventual smaller metal clusters. The relative increase of expected TOF values between the highest and the lowest loadings is higher for the PO_4-modified support compared to that of the bare TiO_2, with a factor of **5.43** and **3.13** for $Cu@PO_4/TiO_2$ and $Ni@PO_4/TiO_2$, respectively. As DRS results highlighted (see **Section 6.2.3**), Cu is found in a rather ionic form and – based on TEM observations (see **Section 6.2.4**) – the tendency to form particles is not very strong. The phosphate groups have a stronger interaction with ionic Cu-precursor species, which explains the higher relative TOF increase of the Cu-systems. In the case of Ni, DRS and TEM results indicated a different situation. $Ni@TiO_2$ was found to have an ionic nature, but also a tendency to form Ni nanoparticles on TiO_2 (presumably upon UV light). The PO_4 groups do stabilize the ionic species, but since there is also the tendency to form NPs, this effect is not as pronounced for $Ni@PO_4/TiO_2$ as it is for $Cu@PO_4/TiO_2$.

In conclusion, the earth-abundant co-catalysts' series do not show any linearity (**Model 1**), but rather follow **Model 2** to a certain extent. Hence, we assume that a change in the morphology's nature is also taking place for these systems, proving the success of the isolation strategy. The relative TOF increase was stronger for the PO_4/TiO_2 substrate, which also speaks for the contribution of the surface modification strategy to facilitate the formation of more active co-catalyst sites on PO_4/TiO_2 than on TiO_2. However, absolute TOF values are always higher for the bare TiO_2, due to the charge-blocking effect of the PO_4 groups.

6.4.5. Earth-abundant series: Influence of light during synthesis

Based on the results discussed in **Section 6.4.3**, in which a high influence of light on the deposition and, therefore, on the activity of the noble metal systems was observed, analogous experiments were carried out for the Cu- and Ni-based systems. Experimental details for the dark synthesis and *in-situ* photodeposition (PD) experiments can be found in **Section 5.4** and **Section 5.5**, respectively.

Figure 23 compares the TOF values of the differently prepared (normal, PD and dark) earth-abundant photocatalysts on bare TiO_2. It becomes apparent from **Figure 23A** that the Cu's HER-activity gets significantly decreased (by a factor of almost 10) when the catalyst is prepared via *in-situ* photodeposition. This can be ascribed to a different deposition mechanism than that of the noble metal systems. The added Cu-precursor might not adsorb as strongly onto TiO_2 during the photodeposition and much of it might not be taking part during the HER reaction. However, this precursor, cannot be recovered through this synthesis path and can be considered to be used up in the procedure. Compared to the PD-sample, our normal impregnation method seems to be the most effective and delivers the highest activity. The TOF for the 1/Cu/dark sample is in the same order of magnitude and decreased only slightly. However, the real loadings of the $1/Cu@TiO_2$/dark was lower than for $1/Cu@TiO_2$ (estimated through TXRF: 0.098 vs. 0.133 wt.%, respectively) but delivered almost the same TOF-value. This result suggests that ambient light does affect the Cu-impregnation procedure, however to a small extent only, and that the Cu species generated by photodeposition are generally less active compared to those obtained via impregnation. One can further suggest that *in-situ*

PD-experiments may result in larger species (i.e. NPs or aggregates) while the dark impregnation process is likely to stabilize more individual species, thus increasing the TOF value.

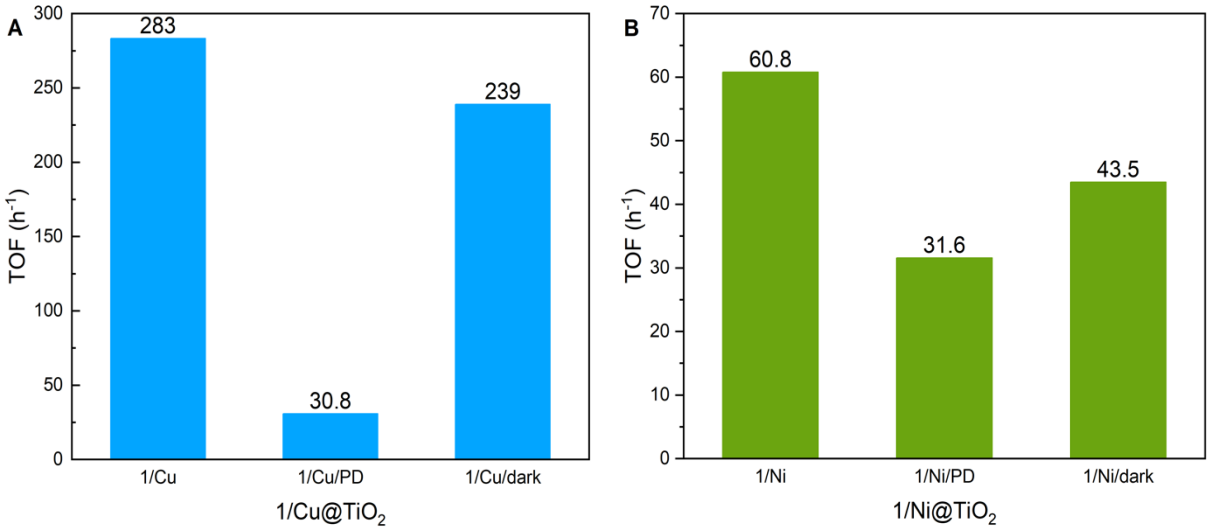

Figure 23 | Comparison of different synthesis methods for composite materials altering the light conditions against TOF-value (H_2 evolution per co-catalyst amount per hour) for **A**, 1/Cu@TiO_2 systems and **B**, 1/Ni@TiO_2 systems.

The photodeposition experiments have a less pronounced effect on the TOF-activity of 1/Ni@TiO_2, as shown in **Figure 23B**. We assume that the Ni-precursor is affected by light to a certain extent and active Ni species can be generated under UV light, similar to the Pt-systems, which were discussed in Section 6.4.3. The ionic Ni-species obtained through the normal impregnation procedure – which should also contribute to the HER-activity – seem to be unstable under PD-conditions, as a result, light-assisted Ni reduction and subsequent particle growth might be taking place. Hence, the TOF of the photodeposited Ni-samples is roughly half as high as for the normal impregnation. Previous studies by Rodríguez et al.[103] have shown that larger Ni NPs (7-15 nm) grow through photodeposition on TiO_2 and they reported the existence of metallic Ni NPs, as well as nickel oxide in their composite materials. We assume to have a similar situation for our PD-experiments. DFT calculations suggest that Ni is likely to become metallic and grow to larger particles, which further explains this behavior for the Ni-systems.

Dark conditions also showed a TOF-decrease of approximately 30%, which suggests that Ni does benefit from partial interaction with light. In this case, a reduction of the real loadings of 1/Ni@TiO_2 vs. 1/Ni@TiO_2/dark from 0.25 to 0.15 wt.% was observed, respectively. Moreover, dark conditions probably allowed ionic Ni species to form but hindered the formation of the Ni NPs observed in the TEM-images of the Ni@TiO_2 samples, which also take part in the photocatalytic reaction, hence reducing the TOF. These results align well with the DRS observations, which stated a mixed situation for the Ni@TiO_2, in which ionic species and NPs coexist.

To sum up, the earth-abundant systems have quite different behaviors when it comes to light interaction. A significant decrease in the loadings is observed for the samples prepared under dark conditions. Cu's activity suffers under PD-conditions, whereas normal and dark conditions appear to render very similar TOFs. This is because more ionic and potentially

single-site species are generated, instead of NPs or other forms of aggregates, which formation is promoted in the presence of ambient or UV light. In any case, the TEM-images of the impregnation process did not show particles for the Cu-systems. Nickel, on the other hand, benefits slightly from light, which can suggest that so-generated Ni NPs, in synergy with Ni ionic species, provide optimal catalytic performance for HER compared to exclusively particles (photodeposition) or more ionic (dark conditions) species. This is in good agreement with our previous findings that Ni^0 is generated *in-situ* through light activation, which shows improved catalytical performance.[100] TEM-results discussed before also confirm the formation of ~ 2.5 nm Ni NPs.

6.4.6. Overall HER-performance assessment

Considering that the most active systems are of utmost interest to industrial applications, this sub-chapter will be dedicated to compare all investigated systems, i.e. noble metals and earth-abundant metals for both support materials. Plotting the TOF-values against the real loadings in double-logarithmic scale results in **Figure 24** and allows us to compare all the different composite materials prepared in this Thesis. As it becomes clearer through this representation, all trends on bare TiO_2 rather follow **Model 2** (red dashed line) and not **Model 1** (grey dashed line). This becomes more complex for PO_4/TiO_2, but the same trend can be observed in general.

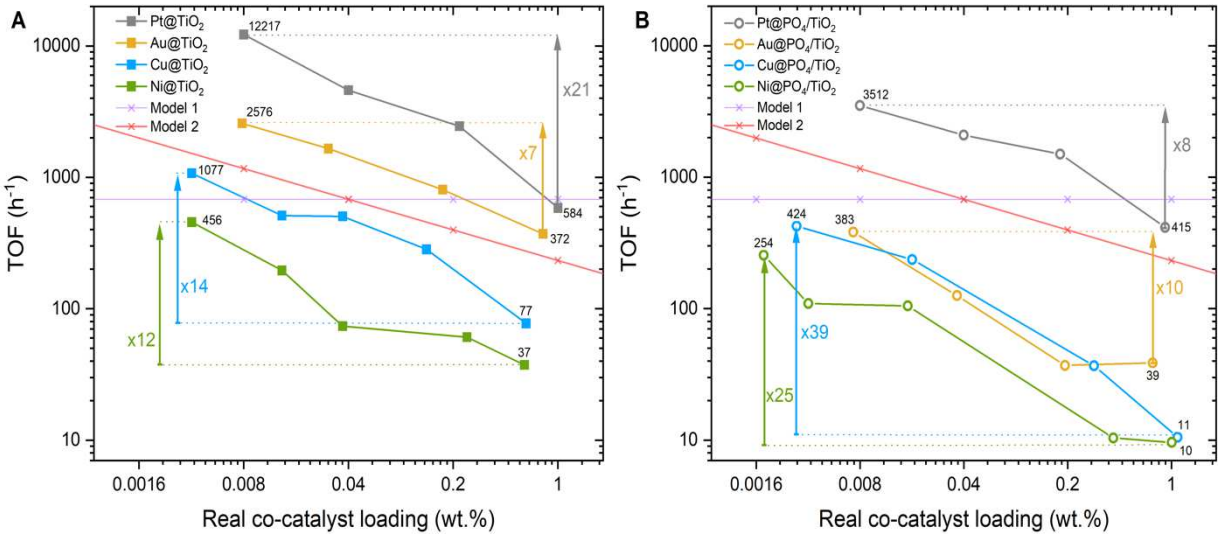

Figure 24 | Double logarithmic representation of all the Pt, Au, Cu and Ni real loadings against TOF values for **A**, bare TiO_2 and **B**, PO_4-modified TiO_2. **Model 1** (grey dashed line) is a straight line parallel to the X-axes and **Model 2** (red dashed line) is a straight line with a non-zero slope. Arrows show the factor by which the TOF is increased between the highest and lowest loadings.

First, looking at the bare TiO_2 support, the performance trend for all employed co-catalysts, shown in **Figure 24A** goes as follows: Pt > Au > Cu > Ni. At the lowest loadings, however, Cu approaches the order of magnitude of the Au's TOF, which is an attractive result considering that Cu is a much more desirable co-catalyst component, due to its abundance. The relative TOF increase from highest to lowest loadings is the strongest for Pt (x21), showing that the isolation strategy worked best for this noble metal.

Considering the trends for the PO_4/TiO_2 support, shown in **Figure 24B**, a strong deviation from **Model 2** can be appreciated, especially for $Au@PO_4/TiO_2$ and $Ni@PO_4/TiO_2$. As has already been discussed in Section 6.4.2 and Section 6.4.4, this may indicate a stronger structural change of the co-catalyst that takes place in these systems compared to the assumption of **Model 2**. In the case of PO_4/TiO_2 support, Pt outperforms all the other co-catalysts in an even more prominent way, delivering around 10 times higher TOFs than the next best system. Interestingly, the performance trend for these series changes slightly to Pt > Cu ≈ Au > Ni. The Cu-series outperformed or was very similar to the Au-series on PO_4/TiO_2. The Ni-series also becomes comparable to Au using this support. Moreover, the relative TOF increase between the highest and lowest loadings was considerably greater for earth-abundant metals than for noble metals in this case. The factors for Cu and Ni are x39 and x25, respectively, the highest values observed in this Thesis, confirming an even greater success of the isolation strategy for these systems.

Nevertheless, the overall trend is that the PO_4 modification rendered lower photocatalytic activities under UV-light (365 nm) than the bare TiO_2. However, the PO_4/TiO_2 support showed a narrowing of its band gap (see Section 6.1.1), which makes it promising for visible-light applications. We hypothesize that visible-light experiments for the composite materials on both supports could potentially result in more equal catalytic performances between TiO_2 and PO_4/TiO_2 or even a more advantageous situation for PO_4/TiO_2.

6.4.7. Economic considerations

Based on the reasonings in the introduction of this Thesis, especially from Section 2.3.1, in which a shift towards more abundant co-catalysts was emphasized, considerations in this regard will also be accounted for. Abundance or scarcity can be directly translated to the prices of the employed co-catalysts. Taking the prices of the metal-precursors (from commercial suppliers) used for the synthesis of the composite materials into consideration, a new "turn-over frequency" arises. The TOF is defined as moles of H_2 evolved per hour per mole of co-catalyst. If the price of such co-catalyst precursors is taken into account, i.e. how much the immobilized co-catalyst costs for each particular composite, then a H_2 evolution rate per hour per $€_{co\text{-}cat}$ can be constructed. After plotting this new activity per € against the real loadings (**Figure 25**) of the composite materials, a very different representation can be seen. Strikingly, the earth-abundant systems show an increased HER-performance per € compared to the noble metals. For both investigated supports, the performance trends change from the common Pt > Au > Cu > Ni to the new **Cu** > **Ni** > **Pt** > **Au**.

This goes well in line with Gray's argument, who stated that future photocatalysts should be as cheap as "*literally a rock*".[1] In order to implement photo-catalysts for high-scale applications, they should not only be highly active, but also affordable and robust. Being slightly less active but significantly cheaper seems to be a convenient trade-off for the earth-abundant-based photo-catalysts prepared in this work.

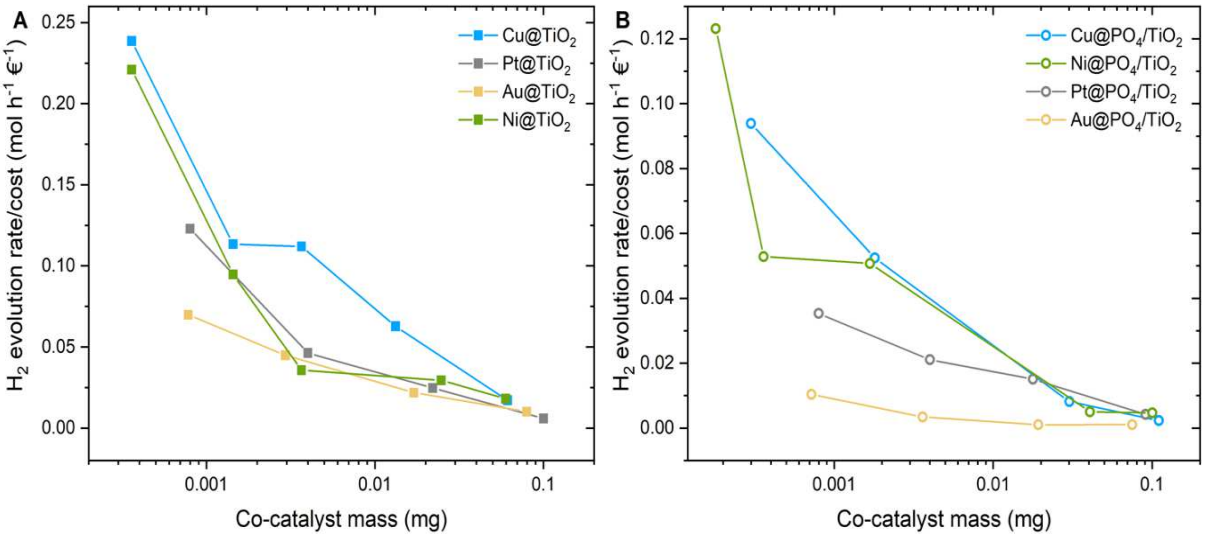

Figure 25 | HER-activity per € of co-catalyst against real loadings for **A**, Pt, Au, Cu and Ni on bare TiO_2 and **B**, Pt, Au, Cu and Ni on PO_4/TiO_2.

Our wet impregnation synthesis approach (under ambient light or dark conditions) also proves to be beneficial from an economic point of view, when comparing it to the well-established *in-situ* photodeposition. During the PD-experiments, the whole amount of metal precursor is being added to the reactor, and it cannot be recovered. However, elemental analysis (TXRF) results have shown that the amount of co-catalyst loaded on TiO_2 after the photocatalytic reaction for such experiments is only around half of the added amount. Hence, we believe that a significant part of the precursor gets wasted in using this deposition method. Contrastingly, the composite materials prepared through the wet impregnation process preserve only the strongly absorbed precursor species, which are taking part in the photocatalytic reaction in their totality. As our results **in Section 6.2.2** have shown, a significant part of the precursor used in the impregnation-synthesis stayed in the solution. After filtration, the unused precursor stays intact and it can be easily recovered and used for further impregnations, maximizing the utilization of the precious precursor species (especially considering Pt and Au) and making our impregnation procedure more advantageous to the common photodeposition approach.

Summing up, the general trend for the catalytic performance in terms of TOFs (moles of H_2 per hour per moles of co-catalyst) for the most active support, i.e. bare TiO_2, is Pt > Au > Cu > Ni. Taking prices of used co-catalysts into consideration, the performance per cost of co-catalyst gets almost inverted, and the earth-abundant systems appear to be surpassing the noble metal ones in the following order: Cu > Ni > Pt > Au. In addition to this, for all investigated systems, following the isolation strategy does increase the TOF numbers significantly, reflecting the increased atom-utilization efficiency and potential stabilization of co-catalyst with single-site nature.

7. Conclusions

The implementation of suitable protocols for the synthesis and evaluation of heterogeneous single-metal-site photocatalysts – being this work's main motivation – was achieved successfully. HER-active earth-abundant and noble metal-based co-catalysts were prepared through the wet impregnation process and the use of the isolation strategy increased the catalytical activity for all investigated systems significantly, which, aided by theoretical models, proves a tendency towards the single-site's formation.

The precursor's type and structure had major effects on the adsorption and deposition process, reflected on the final loadings at the support. Earth-abundant precursors showed lower real loadings compared to noble metals, which is attributed to the different deposition mechanisms. Noble metal precursors – aided by light – photo-reduce and form nanoparticles with real loadings similar to the ideal ones. In contrast, the impregnation of earth-abundant metal precursors is not strongly affected by ambient light. In their case, only the substrate-stabilized co-catalyst species were left at the surface, resulting in lower real loadings. The DRS spectra showed NP-characteristic peaks for Pt and Au co-catalysts, while Cu demonstrated ionic complexed species adsorbed on the substrate's surface. In the case of Ni, a mixed situation could be seen, in which NPs and other ionic species coexist. Further confirmation was obtained through TEM-micrographs, in which 1-2, 5-13 and 2-3 nm NPs were detected on the surface of TiO_2 for Pt, Au and Ni, respectively. Cu samples, in turn, did not exhibit any surface decoration. However, the formation of small clusters and/or ionic species cannot be excluded due to the TEM-instrument's resolution limits.

The surface of TiO_2 was functionalized with phosphate groups, which narrowed the semiconductor's bandgap from 3.20 to 3.15 eV, estimated through DRS-measurements and subsequent extrapolation using Tauc-plots. Furthermore, the change in the surface chemistry and surface charge caused by the PO_4 groups resulted in enhanced adsorption of the metal precursor and therefore an increased loading of the earth-abundant metals was successfully achieved. However, the composite materials prepared with PO_4-modified TiO_2 invariably exhibited lower H_2 evolution rates and TOF-values compared to the bare TiO_2 counterpart. This was ascribed to the slower charge transfer dynamics and charge blocking effect of the PO_4 layer during the photocatalytic reactions. This same effect also decreased the light-dependent deposition of noble metal systems, resulting in lower loadings. Hence, while potentially enabling the formation and better stabilization of more single-site species, this modification diminished the catalytic performance under UV-illumination.

The prepared composites based on two different substrates (TiO_2 and PO_4-modified TiO_2), four different metal precursors (Cu, Ni, Pt and Au), and different co-catalyst loadings (ranging from 0.008 to 5 wt.%) have been next evaluated towards photocatalytic HER.

The experimental HER data for earth-abundant and noble metal systems was consistently in line with our non-linear **Model 2**, describing an alteration in the co-catalyst's size/morphology upon decreased loadings. This comparison strongly suggests that the proposed isolation strategy did facilitate the formation and stabilization of smaller, perhaps even single-site-like co-catalyst species. Furthermore, they were more active (per atom), which speaks for an enhanced atom utilization efficiency, reflected in the increased TOF-values for the lowest loadings, especially in the case of Pt. The PO_4/TiO_2 support contributed more strongly to the size/morphology change towards smaller species for the Au and Cu systems, thus confirming the beneficial structural effect of surface modification to single-site stabilization.

Moreover, differently to well-established photodeposition protocols, our findings show that “synthesis under dark” conditions have a strong impact during synthesis and indeed promote the formation of more active co-catalyst species. This effect was especially pronounced in the case of Pt and Au, where the photodeposition of 2-3 and 5-11 nm nanoparticles, respectively, was suppressed, resulting in the formation of smaller and more active co-catalysts.

The general trend for the catalytic performance in terms of H_2 evolution rates and TOF numbers for all investigated co-catalysts holds the expected sequence Pt > Au > Cu > Ni. At low loadings and when using PO_4/TiO_2 however, earth-abundant systems reach HER activities comparable to that of Au-based samples. Relative increase factors for TOF values between the highest and lowest loadings show that the isolation strategy was most successful for $Pt@TiO_2$ (x21) and for $Cu@PO_4/TiO_2$ (x39).

Finally, the economic considerations of the prepared catalysts have been considered. Taking the prices of the precursor species into consideration, the performance of the systems normalized per cost gets inverted, and the earth-abundant systems surpass the noble-based: Cu > Ni > Pt > Au, thus suggesting that this single-site photocatalysis strategy can open up new prospects towards some of the practical applications of photocatalysis.

8. Outlook

A series of promising experiments and measurements had to be left out due to the time constraint of this project. Regarding the PO_4/TiO_2 substrate, synthesis parameters need to be adjusted, in terms of pH-buffers and reaction times, to obtain full/controlled coverage of TiO_2 with phosphate groups. We believe this would not only allow us to control the adsorption of precursors but would further enable us to narrow the bandgap even more. In this line, we strongly presume that visible-light HER-experiments on the PO_4/TiO_2 composite materials are likely to outperform bare TiO_2 and can be pursued in the future. Moreover, the behavior of all composite materials in photocatalytic experiments without the use of sacrificial agents could help further elucidating the charge-blocking effect of the phosphate layer.

For improving the loadings but suppressing the growth of nanoparticles, optimal conditions need to be found during the wet impregnation process. Using dark conditions, longer impregnation times and avoiding high temperatures while drying – by using reduced pressures (Schlenk-line) – could potentially facilitate the formation of more ionic and better-stabilized single-sites even further. This hypothesis stands on two observations: *i)* the loadings of the dark impregnation samples were consistently lower than those of the normally prepared composites, and *ii)* the $Au@TiO_2$/dark sample was white right after washing and only got a deep purple coloration – a clear sign for the SPR-effect of Au-NPs – after the oven-drying.

Long-run HER-experiments, especially for the Ni-systems, which never reached a steady-state H_2 evolution rate in our short-term experiments, are of great interest as well, since Ni's activity seemed to be increasing with time. Such investigations, also for the other metals, would additionally provide insights in terms of robustness and stability of the photocatalysts, important qualities that could not be investigated during this work. Furthermore, other catalytic reactions, as the OER and CO_2-reduction reaction would be worth investigating too.

As stated in the **Introduction**, characterization of single-sites is very challenging. Although X-ray photoelectron spectroscopy was used during this work to determine the oxidation state of the catalytically active species, the sensitivity of the employed instrument (SPECS XPS-spectrometer) was not high enough to obtain satisfactory data. Hence, more powerful synchrotron techniques would be an essential aid to understand our systems more deeply. With XANES and EXAFS measurements, the bonding situation in the catalyst (existence/absence of metal-metal bonds) or the average oxidation states of the co-catalyst could be understood more in detail and the single-site structure could be proven further, not only in a phenomenological way.

9. List of References

(1) Gray, H. B. Powering the Planet with Solar Fuel. *Nature Chemistry* **2009**, *1* (1), 7–7. https://doi.org/10.1038/nchem.141.

(2) Hunter, B. M.; Gray, H. B.; Müller, A. M. Earth-Abundant Heterogeneous Water Oxidation Catalysts. *Chem. Rev.* **2016**, *116* (22), 14120–14136. https://doi.org/10.1021/acs.chemrev.6b00398.

(3) Rogelj, J.; McCollum, D. L.; Riahi, K. The UN's "Sustainable Energy for All" Initiative Is Compatible with a Warming Limit of 2 °C. *Nature Climate Change* **2013**, *3* (6), 545–551. https://doi.org/10.1038/nclimate1806.

(4) Caldeira, K.; Wickett, M. E. Anthropogenic Carbon and Ocean PH. *Nature* **2003**, *425* (6956), 365–365. https://doi.org/10.1038/425365a.

(5) Bp-Stats-Review-2019-Full-Report.Pdf.

(6) World Energy Balances 2019 – Analysis https://www.iea.org/reports/world-energy-balances-2019 (accessed Apr 6, 2020).

(7) Xu, D.; Dong, L.; Ren, J. Chapter 2 - Introduction of Hydrogen Routines. In *Hydrogen Economy*; Scipioni, A., Manzardo, A., Ren, J., Eds.; Academic Press, 2017; pp 35–54. https://doi.org/10.1016/B978-0-12-811132-1.00002-X.

(8) Bossel, U.; Eliasson, B.; Taylor, G. The Future of the Hydrogen Economy: Bright or Bleak? *Cogeneration and Competitive Power Journal* **2003**, *18* (3), 29–70. https://doi.org/10.1080/15453660309509023.

(9) Liu, H.; Almansoori, A.; Fowler, M.; Elkamel, A. Analysis of Ontario's Hydrogen Economy Demands from Hydrogen Fuel Cell Vehicles. *International Journal of Hydrogen Energy* **2012**, *37* (11), 8905–8916. https://doi.org/10.1016/j.ijhydene.2012.03.029.

(10) Ren, J.; Gao, S.; Liang, H.; Tan, S.; Dong, L. Chapter 1 - The Role of Hydrogen Energy: Strengths, Weaknesses, Opportunities, and Threats. In *Hydrogen Economy*; Scipioni, A., Manzardo, A., Ren, J., Eds.; Academic Press, 2017; pp 1–33. https://doi.org/10.1016/B978-0-12-811132-1.00001-8.

(11) Bhat, S. A.; Sadhukhan, J. Process Intensification Aspects for Steam Methane Reforming: An Overview. *AIChE Journal* **2009**, *55* (2), 408–422. https://doi.org/10.1002/aic.11687.

(12) Wagner, N. J.; Coertzen, M.; Matjie, R. H.; van Dyk, J. C. Chapter 5 - Coal Gasification. In *Applied Coal Petrology*; Suárez-Ruiz, I., Crelling, J. C., Eds.; Elsevier: Burlington, 2008; pp 119–144. https://doi.org/10.1016/B978-0-08-045051-3.00005-1.

(13) Liao, C.-H.; Huang, C.-W.; Wu, J. C. S. Hydrogen Production from Semiconductor-Based Photocatalysis via Water Splitting. *Catalysts* **2012**, *2* (4), 490–516. https://doi.org/10.3390/catal2040490.

(14) Mohtasham, J. Review Article-Renewable Energies. *Energy Procedia* **2015**, *74*, 1289–1297. https://doi.org/10.1016/j.egypro.2015.07.774.

(15) Ni, M.; Leung, D. Y. C.; Leung, M. K. H.; Sumathy, K. An Overview of Hydrogen Production from Biomass. *Fuel Processing Technology* **2006**, *87* (5), 461–472. https://doi.org/10.1016/j.fuproc.2005.11.003.

(16) Millet, P.; Grigoriev, S. Chapter 2 - Water Electrolysis Technologies. In *Renewable Hydrogen Technologies*; Gandía, L. M., Arzamendi, G., Diéguez, P. M., Eds.; Elsevier: Amsterdam, 2013; pp 19–41. https://doi.org/10.1016/B978-0-444-56352-1.00002-7.

(17) Parida, B.; Iniyan, S.; Goic, R. A Review of Solar Photovoltaic Technologies. *Renewable and Sustainable Energy Reviews* **2011**, *15* (3), 1625–1636. https://doi.org/10.1016/j.rser.2010.11.032.

(18) Yang, Y.; Ri, K.; Mei, A.; Liu, L.; Hu, M.; Liu, T.; Li, X.; Han, H. The Size Effect of TiO2 Nanoparticles on a Printable Mesoscopic Perovskite Solar Cell. *J. Mater. Chem. A* **2015**, *3* (17), 9103–9107. https://doi.org/10.1039/C4TA07030E.

(19) Baykara, S. Z. Experimental Solar Water Thermolysis. *International Journal of Hydrogen Energy* **2004**, *29* (14), 1459–1469. https://doi.org/10.1016/j.ijhydene.2004.02.011.

(20) Li, X.; Yu, J.; Jiang, C. Chapter 1 - Principle and Surface Science of Photocatalysis. In *Interface Science and Technology*; Yu, J., Jaroniec, M., Jiang, C., Eds.; Surface Science of Photocatalysis; Elsevier, 2020; Vol. 31, pp 1–38. https://doi.org/10.1016/B978-0-08-102890-2.00001-4.
(21) Zhang, B.; Sun, L. Artificial Photosynthesis: Opportunities and Challenges of Molecular Catalysts. *Chem. Soc. Rev.* **2019**, *48* (7), 2216–2264. https://doi.org/10.1039/C8CS00897C.
(22) Ahmad, H.; Kamarudin, S. K.; Minggu, L. J.; Kassim, M. Hydrogen from Photo-Catalytic Water Splitting Process: A Review. *Renewable and Sustainable Energy Reviews* **2015**, *43*, 599–610. https://doi.org/10.1016/j.rser.2014.10.101.
(23) Yang, J.; Wang, D.; Han, H.; Li, C. Roles of Cocatalysts in Photocatalysis and Photoelectrocatalysis. *Acc. Chem. Res.* **2013**, *46* (8), 1900–1909. https://doi.org/10.1021/ar300227e.
(24) Li, X.; Yu, J.; Low, J.; Fang, Y.; Xiao, J.; Chen, X. Engineering Heterogeneous Semiconductors for Solar Water Splitting. *J. Mater. Chem. A* **2015**, *3* (6), 2485–2534. https://doi.org/10.1039/C4TA04461D.
(25) Ran, J.; Zhang, J.; Yu, J.; Jaroniec, M.; Zhang Qiao, S. Earth-Abundant Cocatalysts for Semiconductor-Based Photocatalytic Water Splitting. *Chemical Society Reviews* **2014**, *43* (22), 7787–7812. https://doi.org/10.1039/C3CS60425J.
(26) Li, X.; Yu, J.; Jaroniec, M. Hierarchical Photocatalysts. *Chem. Soc. Rev.* **2016**, *45* (9), 2603–2636. https://doi.org/10.1039/C5CS00838G.
(27) Chu, S.; Li, W.; Yan, Y.; Hamann, T.; Shih, I.; Wang, D.; Mi, Z. Roadmap on Solar Water Splitting: Current Status and Future Prospects. *Nano Futures* **2017**, *1* (2), 022001. https://doi.org/10.1088/2399-1984/aa88a1.
(28) Li, X.; Yu, J.; Wageh, S.; Al-Ghamdi, A. A.; Xie, J. Graphene in Photocatalysis: A Review. *Small* **2016**, *12* (48), 6640–6696. https://doi.org/10.1002/smll.201600382.
(29) Trasatti, S. Work Function, Electronegativity, and Electrochemical Behaviour of Metals. *Journal of Electroanalytical Chemistry and Interfacial Electrochemistry* **1972**, *39* (1), 163–184. https://doi.org/10.1016/S0022-0728(72)80485-6.
(30) Xiao, N.; Li, S.; Li, X.; Ge, L.; Gao, Y.; Li, N. The Roles and Mechanism of Cocatalysts in Photocatalytic Water Splitting to Produce Hydrogen. *Chinese Journal of Catalysis* **2020**, *41* (4), 642–671. https://doi.org/10.1016/S1872-2067(19)63469-8.
(31) Weng, B.; Qi, M.-Y.; Han, C.; Tang, Z.-R.; Xu, Y.-J. Photocorrosion Inhibition of Semiconductor-Based Photocatalysts: Basic Principle, Current Development, and Future Perspective. *ACS Catal.* **2019**, *9* (5), 4642–4687. https://doi.org/10.1021/acscatal.9b00313.
(32) Xiao, J.-D.; Han, L.; Luo, J.; Yu, S.-H.; Jiang, H.-L. Integration of Plasmonic Effects and Schottky Junctions into Metal–Organic Framework Composites: Steering Charge Flow for Enhanced Visible-Light Photocatalysis. *Angewandte Chemie International Edition* **2018**, *57* (4), 1103–1107. https://doi.org/10.1002/anie.201711725.
(33) Mooiman, M. B.; Sole, K. C.; Dinham, N. The Precious Metals Industry. In *Metal Sustainability*; John Wiley & Sons, Ltd, 2016; pp 361–396. https://doi.org/10.1002/9781119009115.ch16.
(34) Bardi, U.; Jakobi, R.; Hettiarachchi, H. Mineral Resource Depletion: A Coming Age of Stockpiling? *Biophys Econ Resour Qual* **2016**, *1* (1), 4. https://doi.org/10.1007/s41247-016-0004-x.
(35) Bardi, U.; Caporali, S. Precious Metals in Automotive Technology: An Unsolvable Depletion Problem? *Minerals* **2014**, *4* (2), 388–398. https://doi.org/10.3390/min4020388.
(36) Tran, P. D.; Xi, L.; Batabyal, S. K.; Wong, L. H.; Barber, J.; Loo, J. S. C. Enhancing the Photocatalytic Efficiency of TiO2 Nanopowders for H2 Production by Using Non-Noble Transition Metal Co-Catalysts. *Phys. Chem. Chem. Phys.* **2012**, *14* (33), 11596–11599. https://doi.org/10.1039/C2CP41450C.
(37) Lee, B.-H.; Park, S.; Kim, M.; Sinha, A. K.; Lee, S. C.; Jung, E.; Chang, W. J.; Lee, K.-S.; Kim, J. H.; Cho, S.-P.; Kim, H.; Nam, K. T.; Hyeon, T. Reversible and Cooperative

Photoactivation of Single-Atom Cu/TiO 2 Photocatalysts. *Nature Materials* **2019**, *18* (6), 620–626. https://doi.org/10.1038/s41563-019-0344-1.
(38) Takata, T.; Jiang, J.; Sakata, Y.; Nakabayashi, M.; Shibata, N.; Nandal, V.; Seki, K.; Hisatomi, T.; Domen, K. Photocatalytic Water Splitting with a Quantum Efficiency of Almost Unity. *Nature* **2020**, *581* (7809), 411–414. https://doi.org/10.1038/s41586-020-2278-9.
(39) Wang, D.; Astruc, D. The Recent Development of Efficient Earth-Abundant Transition-Metal Nanocatalysts. *Chem. Soc. Rev.* **2017**, *46* (3), 816–854. https://doi.org/10.1039/C6CS00629A.
(40) Petrucci, M. G. L.; Kakkar, A. K. Heterogenizing Homogeneous Catalysis. *Advanced Materials* **1996**, *8* (3), 251–253. https://doi.org/10.1002/adma.19960080315.
(41) Shelke, Y. G.; Yashmeen, A.; Gholap, A. V. A.; Gharpure, S. J.; Kapdi, A. R. Homogeneous Catalysis: A Powerful Technology for the Modification of Important Biomolecules. *Chemistry – An Asian Journal* **2018**, *13* (20), 2991–3013. https://doi.org/10.1002/asia.201801020.
(42) Cui, X.; Li, W.; Ryabchuk, P.; Junge, K.; Beller, M. Bridging Homogeneous and Heterogeneous Catalysis by Heterogeneous Single-Metal-Site Catalysts. *Nat Catal* **2018**, *1* (6), 385–397. https://doi.org/10.1038/s41929-018-0090-9.
(43) Wang, A.; Li, J.; Zhang, T. Heterogeneous Single-Atom Catalysis. *Nat Rev Chem* **2018**, *2* (6), 65–81. https://doi.org/10.1038/s41570-018-0010-1.
(44) Zecchina, A.; Bordiga, S.; Groppo, E. The Structure and Reactivity of Single and Multiple Sites on Heterogeneous and Homogeneous Catalysts: Analogies, Differences, and Challenges for Characterization Methods. In *Selective Nanocatalysts and Nanoscience*; Zecchina, A., Bordiga, S., Groppo, E., Eds.; Wiley-VCH Verlag GmbH & Co. KGaA: Weinheim, Germany, 2011; pp 1–27. https://doi.org/10.1002/9783527635689.ch1.
(45) Liu, J. Catalysis by Supported Single Metal Atoms. *ACS Catal.* **2017**, *7* (1), 34–59. https://doi.org/10.1021/acscatal.6b01534.
(46) Wang, B.; Cai, H.; Shen, S. Single Metal Atom Photocatalysis. *Small Methods* **2019**, 1800447. https://doi.org/10.1002/smtd.201800447.
(47) Li, Y. H.; Xing, J.; Yang, X. H.; Yang, H. G. Cluster Size Effects of Platinum Oxide as Active Sites in Hydrogen Evolution Reactions. *Chemistry – A European Journal* **2014**, *20* (39), 12377–12380. https://doi.org/10.1002/chem.201402989.
(48) Xing, J.; Chen, J. F.; Li, Y. H.; Yuan, W. T.; Zhou, Y.; Zheng, L. R.; Wang, H. F.; Hu, P.; Wang, Y.; Zhao, H. J.; Wang, Y.; Yang, H. G. Stable Isolated Metal Atoms as Active Sites for Photocatalytic Hydrogen Evolution. *Chemistry – A European Journal* **2014**, *20* (8), 2138–2144. https://doi.org/10.1002/chem.201303366.
(49) Li, X.; Bi, W.; Zhang, L.; Tao, S.; Chu, W.; Zhang, Q.; Luo, Y.; Wu, C.; Xie, Y. Single-Atom Pt as Co-Catalyst for Enhanced Photocatalytic H2 Evolution. *Advanced Materials* **2016**, *28* (12), 2427–2431. https://doi.org/10.1002/adma.201505281.
(50) Fang, X.; Shang, Q.; Wang, Y.; Jiao, L.; Yao, T.; Li, Y.; Zhang, Q.; Luo, Y.; Jiang, H.-L. Single Pt Atoms Confined into a Metal–Organic Framework for Efficient Photocatalysis. *Advanced Materials* **2018**, *30* (7), 1705112. https://doi.org/10.1002/adma.201705112.
(51) Peters, A. W.; Li, Z.; Farha, O. K.; Hupp, J. T. Toward Inexpensive Photocatalytic Hydrogen Evolution: A Nickel Sulfide Catalyst Supported on a High-Stability Metal–Organic Framework. *ACS Appl. Mater. Interfaces* **2016**, *8* (32), 20675–20681. https://doi.org/10.1021/acsami.6b04729.
(52) Cao, Y.; Chen, S.; Luo, Q.; Yan, H.; Lin, Y.; Liu, W.; Cao, L.; Lu, J.; Yang, J.; Yao, T.; Wei, S. Atomic-Level Insight into Optimizing the Hydrogen Evolution Pathway over a Co $_1$ -N $_4$ Single-Site Photocatalyst. *Angew. Chem. Int. Ed.* **2017**, *56* (40), 12191–12196. https://doi.org/10.1002/anie.201706467.
(53) Huang, P.; Huang, J.; Pantovich, S. A.; Carl, A. D.; Fenton, T. G.; Caputo, C. A.; Grimm, R. L.; Frenkel, A. I.; Li, G. Selective CO $_2$ Reduction Catalyzed by Single Cobalt Sites on Carbon Nitride under Visible-Light Irradiation. *J. Am. Chem. Soc.* **2018**, *140* (47), 16042–16047. https://doi.org/10.1021/jacs.8b10380.

(54) Gao, G.; Jiao, Y.; Waclawik, E. R.; Du, A. Single Atom (Pd/Pt) Supported on Graphitic Carbon Nitride as an Efficient Photocatalyst for Visible-Light Reduction of Carbon Dioxide. *J. Am. Chem. Soc.* **2016**, *138* (19), 6292–6297. https://doi.org/10.1021/jacs.6b02692.
(55) Gao, C.; Chen, S.; Wang, Y.; Wang, J.; Zheng, X.; Zhu, J.; Song, L.; Zhang, W.; Xiong, Y. Heterogeneous Single-Atom Catalyst for Visible-Light-Driven High-Turnover CO2 Reduction: The Role of Electron Transfer. *Advanced Materials* **2018**, *30* (13), 1704624. https://doi.org/10.1002/adma.201704624.
(56) Zhang, H.; Wei, J.; Dong, J.; Liu, G.; Shi, L.; An, P.; Zhao, G.; Kong, J.; Wang, X.; Meng, X.; Zhang, J.; Ye, J. Efficient Visible-Light-Driven Carbon Dioxide Reduction by a Single-Atom Implanted Metal-Organic Framework. *Angew. Chem.* **2016**, *128* (46), 14522–14526. https://doi.org/10.1002/ange.201608597.
(57) Wang, F.; Wang, Y.; Li, Y.; Cui, X.; Zhang, Q.; Xie, Z.; Liu, H.; Feng, Y.; Lv, W.; Liu, G. The Facile Synthesis of a Single Atom-Dispersed Silver-Modified Ultrathin g-C3N4 Hybrid for the Enhanced Visible-Light Photocatalytic Degradation of Sulfamethazine with Peroxymonosulfate. *Dalton Trans.* **2018**, *47* (20), 6924–6933. https://doi.org/10.1039/C8DT00919H.
(58) An, S.; Zhang, G.; Wang, T.; Zhang, W.; Li, K.; Song, C.; Miller, J. T.; Miao, S.; Wang, J.; Guo, X. High-Density Ultra-Small Clusters and Single-Atom Fe Sites Embedded in Graphitic Carbon Nitride (g-C3N4) for Highly Efficient Catalytic Advanced Oxidation Processes. *ACS Nano* **2018**, *12* (9), 9441–9450. https://doi.org/10.1021/acsnano.8b04693.
(59) Liu, W.; Cao, L.; Cheng, W.; Cao, Y.; Liu, X.; Zhang, W.; Mou, X.; Jin, L.; Zheng, X.; Che, W.; Liu, Q.; Yao, T.; Wei, S. Single-Site Active Cobalt-Based Photocatalyst with a Long Carrier Lifetime for Spontaneous Overall Water Splitting. *Angewandte Chemie International Edition* **2017**, *56* (32), 9312–9317. https://doi.org/10.1002/anie.201704358.
(60) Li, P.; Wang, M.; Duan, X.; Zheng, L.; Cheng, X.; Zhang, Y.; Kuang, Y.; Li, Y.; Ma, Q.; Feng, Z.; Liu, W.; Sun, X. Boosting Oxygen Evolution of Single-Atomic Ruthenium through Electronic Coupling with Cobalt-Iron Layered Double Hydroxides. *Nat Commun* **2019**, *10* (1), 1–11. https://doi.org/10.1038/s41467-019-09666-0.
(61) Qiao, B.; Liu, J.; Wang, Y.-G.; Lin, Q.; Liu, X.; Wang, A.; Li, J.; Zhang, T.; Liu, J. (Jimmy). Highly Efficient Catalysis of Preferential Oxidation of CO in H2-Rich Stream by Gold Single-Atom Catalysts. *ACS Catal.* **2015**, *5* (11), 6249–6254. https://doi.org/10.1021/acscatal.5b01114.
(62) Qiao, B.; Wang, A.; Yang, X.; Allard, L. F.; Jiang, Z.; Cui, Y.; Liu, J.; Li, J.; Zhang, T. Single-Atom Catalysis of CO Oxidation Using Pt_1/FeO_x. *Nature Chemistry* **2011**, *3* (8), 634–641. https://doi.org/10.1038/nchem.1095.
(63) Isomura, N.; Wu, X.; Watanabe, Y. Atomic-Resolution Imaging of Size-Selected Platinum Clusters on TiO2(110) Surfaces. *J. Chem. Phys.* **2009**, *131* (16), 164707. https://doi.org/10.1063/1.3251786.
(64) Li, J.; Li, X.; Zhai, H.-J.; Wang, L.-S. Au20: A Tetrahedral Cluster. *Science* **2003**, *299* (5608), 864–867. https://doi.org/10.1126/science.1079879.
(65) Johansson, M. P.; Sundholm, D.; Vaara, J. Au32: A 24-Carat Golden Fullerene. *Angewandte Chemie International Edition* **2004**, *43* (20), 2678–2681. https://doi.org/10.1002/anie.200453986.
(66) Chen; Cai, Y.; Yan, Z.; Goodman, D. W. On the Origin of the Unique Properties of Supported Au Nanoparticles. *J. Am. Chem. Soc.* **2006**, *128* (19), 6341–6346. https://doi.org/10.1021/ja0557536.
(67) Valden, M.; Lai, X.; Goodman, D. W. Onset of Catalytic Activity of Gold Clusters on Titania with the Appearance of Nonmetallic Properties. *Science* **1998**, *281* (5383), 1647–1650. https://doi.org/10.1126/science.281.5383.1647.
(68) Bruix, A.; Lykhach, Y.; Matolínová, I.; Neitzel, A.; Skála, T.; Tsud, N.; Vorokhta, M.; Stetsovych, V.; Ševčíková, K.; Myslivecek, J.; Fiala, R.; Václavů, M.; Prince, K. C.; Bruyère, S.; Potin, V.; Illas, F.; Matolín, V.; Libuda, J.; Neyman, K. M. Maximum Noble-Metal Efficiency in Catalytic Materials: Atomically Dispersed Surface Platinum.

Angewandte Chemie International Edition **2014**, *53* (39), 10525–10530. https://doi.org/10.1002/anie.201402342.
(69) Jones, J.; Xiong, H.; DeLaRiva, A. T.; Peterson, E. J.; Pham, H.; Challa, S. R.; Qi, G.; Oh, S.; Wiebenga, M. H.; Hernández, X. I. P.; Wang, Y.; Datye, A. K. Thermally Stable Single-Atom Platinum-on-Ceria Catalysts via Atom Trapping. *Science* **2016**, *353* (6295), 150–154. https://doi.org/10.1126/science.aaf8800.
(70) Ramer, G.; Lendl, B. Attenuated Total Reflection Fourier Transform Infrared Spectroscopy. In *Encyclopedia of Analytical Chemistry*; American Cancer Society, 2013. https://doi.org/10.1002/9780470027318.a9287.
(71) Hummel, R. E. Differential Reflectance Spectroscopy in Analysis of Surfaces. In *Encyclopedia of Analytical Chemistry*; American Cancer Society, 2006. https://doi.org/10.1002/9780470027318.a2504.
(72) Wobrauschek, P. Total Reflection X-Ray Fluorescence Analysis—a Review. *X-Ray Spectrometry* **2007**, *36* (5), 289–300. https://doi.org/10.1002/xrs.985.
(73) Chapter 4. Characterization techniques for nanomaterials | Elsevier Enhanced Reader https://reader.elsevier.com/reader/sd/pii/B9780128133378000047?token=4925D823D07D3633DF58CFBDA04D97FA95B5266577BEE2553EB8F87016F95E2736BD2B757DBD9AFC6A243C2A91E32FB5 (accessed Jun 15, 2020). https://doi.org/10.1016/B978-0-12-813337-8.00004-7.
(74) Kozuch, S.; Martin, J. M. L. "Turning Over" Definitions in Catalytic Cycles. *ACS Catal.* **2012**, *2* (12), 2787–2794. https://doi.org/10.1021/cs3005264.
(75) Ye, S.; Ding, C.; Li, C. Chapter One - Artificial Photosynthesis Systems for Catalytic Water Oxidation. In *Advances in Inorganic Chemistry*; van Eldik, R., Hubbard, C. D., Eds.; Water Oxidation Catalysts; Academic Press, 2019; Vol. 74, pp 3–59. https://doi.org/10.1016/bs.adioch.2019.03.007.
(76) Hadjiivanov, K. I.; Klissurski, D. G.; Davydov, A. A. Study of Phosphate-Modified TiO2 (Anatase). *Journal of Catalysis* **1989**, *116* (2), 498–505. https://doi.org/10.1016/0021-9517(89)90116-4.
(77) Zhao, D.; Chen, C.; Wang, Y.; Ji, H.; Ma, W.; Zang, L.; Zhao, J. Surface Modification of TiO2 by Phosphate: Effect on Photocatalytic Activity and Mechanism Implication. *J. Phys. Chem. C* **2008**, *112* (15), 5993–6001. https://doi.org/10.1021/jp712049c.
(78) Liu, X.; Li, Y.; Peng, S.; Lu, G.; Li, S. Modification of TiO2 with Sulfate and Phosphate for Enhanced Eosin Y-Sensitized Hydrogen Evolution under Visible Light Illumination. *Photochem. Photobiol. Sci.* **2013**, *12* (10), 1903–1910. https://doi.org/10.1039/C3PP50167A.
(79) Bondi, A. van der Waals Volumes and Radii https://pubs.acs.org/doi/pdf/10.1021/j100785a001 (accessed Apr 25, 2020). https://doi.org/10.1021/j100785a001.
(80) Mikuriya, M.; Schumacher, M.; Kawano, C.; Akihara, T.; Ono, K.; Yoshioka, D.; Sakiyama, H.; Handa, M. Dinuclear Nickel(II) Pivalate with M-Aqua and Di-M-Pivalato Bridges Showing a Ferromagnetic Interaction. *ChemJMold* **2014**, *9* (2), 62–66. https://doi.org/10.19261/cjm.2014.09(2).09.
(81) Bullen, G. J.; Mason, R.; Pauling, P. Octahedral Co-Ordination of Nickel in Nickel(II) Bis Acetylacetone. *Nature* **1961**, *189* (4761), 291–292. https://doi.org/10.1038/189291a0.
(82) Atkins, P.; Overton, T. *Shriver and Atkins' Inorganic Chemistry*; OUP Oxford, 2010.
(83) Zenkovets, G. A.; Shutilov, R. A.; Gavrilov, V. Yu. The State of Copper Ions in Aqueous and Aqueous Ammonia Solutions of Copper Acetate. *Russ. J. Inorg. Chem.* **2018**, *63* (11), 1511–1518. https://doi.org/10.1134/S0036023618110219.
(84) Chen, Y.; Wang, Y.; Li, W.; Yang, Q.; Hou, Q.; Wei, L.; Liu, L.; Huang, F.; Ju, M. Enhancement of Photocatalytic Performance with the Use of Noble-Metal-Decorated TiO2 Nanocrystals as Highly Active Catalysts for Aerobic Oxidation under Visible-Light Irradiation. *Applied Catalysis B: Environmental* **2017**, *210*, 352–367. https://doi.org/10.1016/j.apcatb.2017.03.077.

(85) Shabnam, N.; Pardha-Saradhi, P. Photosynthetic Electron Transport System Promotes Synthesis of Au-Nanoparticles. *PLOS ONE* **2013**, *8* (8), e71123. https://doi.org/10.1371/journal.pone.0071123.
(86) Haiss, W.; Thanh, N. T. K.; Aveyard, J.; Fernig, D. G. Determination of Size and Concentration of Gold Nanoparticles from UV−Vis Spectra. *Anal. Chem.* **2007**, *79* (11), 4215–4221. https://doi.org/10.1021/ac0702084.
(87) Dozzi, M. V.; Candeo, A.; Marra, G.; D'Andrea, C.; Valentini, G.; Selli, E. Effects of Photodeposited Gold vs Platinum Nanoparticles on N,F-Doped TiO2 Photoactivity: A Time-Resolved Photoluminescence Investigation. *J. Phys. Chem. C* **2018**, *122* (26), 14326–14335. https://doi.org/10.1021/acs.jpcc.8b02997.
(88) Almeida, L. C.; Zanoni, M. V. B. Decoration of Ti/TiO2 Nanotubes with Pt Nanoparticles for Enhanced UV-Vis Light Absorption in Photoelectrocatalytic Process. *Journal of the Brazilian Chemical Society* **2014**, *25* (3), 579–588. https://doi.org/10.5935/0103-5053.20140034.
(89) Qiu, S. R.; Wood, B. C.; Ehrmann, P. R.; Demos, S. G.; Miller, P. E.; Schaffers, K. I.; Suratwala, T. I.; Brow, R. K. Origins of Optical Absorption Characteristics of Cu2+ Complexes in Aqueous Solutions. *Phys. Chem. Chem. Phys.* **2015**, *17* (29), 18913–18923. https://doi.org/10.1039/C5CP01688F.
(90) Ramyadevi, J.; Jeyasubramanian, K.; Marikani, A.; Rajakumar, G.; Rahuman, A. A.; Santhoshkumar, T.; Kirthi, A. V.; Jayaseelan, C.; Marimuthu, S. Copper Nanoparticles Synthesized by Polyol Process Used to Control Hematophagous Parasites. *Parasitol Res* **2011**, *109* (5), 1403–1415. https://doi.org/10.1007/s00436-011-2387-3.
(91) Wang, K.; Yang, L.; Zhao, W.; Cao, L.; Sun, Z.; Zhang, F. A Facile Synthesis of Copper Nanoparticles Supported on an Ordered Mesoporous Polymer as an Efficient and Stable Catalyst for Solvent-Free Sonogashira Coupling Reactions. *Green Chem.* **2017**, *19* (8), 1949–1957. https://doi.org/10.1039/C7GC00219J.
(92) Chuang, C.-C.; Lin, C.-K.; Wang, T. T.; Srinivasadesikan, V.; Raghunath, P.; Lin, M. C. Computational and Experimental Studies on the Effect of Hydrogenation of Ni-Doped TiO $_2$ Anatase Nanoparticles for the Application of Water Splitting. *RSC Adv.* **2015**, *5* (99), 81371–81377. https://doi.org/10.1039/C5RA16119C.
(93) Of, A.; Polyaniline, N. N.; Meftah, A. M.; Saion, E.; Maarof, M.; Hj, B.; Moksin, A.; Zainuddin, H. B. *Composite Films Prepared by Radiation Technique*.
(94) González, E.; Rodrigue-Witchel, A.; Reber, C. Absorption Spectroscopy of Octahedral Nickel(II) Complexes: A Case Study of Interactions between Multiple Electronic Excited States. *Coordination Chemistry Reviews* **2007**, *251* (3), 351–363. https://doi.org/10.1016/j.ccr.2006.08.011.
(95) Lewis, F. D.; Salvi, G. D.; Kanis, D. R.; Ratner, M. A. Electronic Structure and Spectroscopy of Nickel(II), Palladium(II), and Platinum(II) Acetylacetonate Complexes. *Inorg. Chem.* **1993**, *32* (7), 1251–1258. https://doi.org/10.1021/ic00059a037.
(96) Zhu, S.; Wang, L. M.; Zu, X. T.; Xiang, X. Optical and Magnetic Properties of Ni Nanoparticles in Rutile Formed by Ni Ion Implantation. *Appl. Phys. Lett.* **2006**, *88* (4), 043107. https://doi.org/10.1063/1.2168037.
(97) Haselmann, G. M.; Baumgartner, B.; Wang, J.; Wieland, K.; Gupta, T.; Herzig, C.; Limbeck, A.; Lendl, B.; Eder, D. In Situ Pt Photodeposition and Methanol Photooxidation on Pt/TiO2: Pt-Loading-Dependent Photocatalytic Reaction Pathways Studied by Liquid-Phase Infrared Spectroscopy. *ACS Catal.* **2020**, *10* (5), 2964–2977. https://doi.org/10.1021/acscatal.9b05588.
(98) Pelletier, J. D. A.; Basset, J.-M. Catalysis by Design: Well-Defined Single-Site Heterogeneous Catalysts. *Acc. Chem. Res.* **2016**, *49* (4), 664–677. https://doi.org/10.1021/acs.accounts.5b00518.
(99) Akimov, A. V.; Asahi, R.; Jinnouchi, R.; Prezhdo, O. V. What Makes the Photocatalytic CO2 Reduction on N-Doped Ta2O5 Efficient: Insights from Nonadiabatic Molecular Dynamics. *J. Am. Chem. Soc.* **2015**, *137* (35), 11517–11525. https://doi.org/10.1021/jacs.5b07454.

(100) Schubert, J. S.; Popovic, J.; Haselmann, G. M.; Nandan, S. P.; Wang, J.; Giesriegl, A.; Cherevan, A. S.; Eder, D. Immobilization of Co, Mn, Ni and Fe Oxide Co-Catalysts on TiO_2 for Photocatalytic Water Splitting Reactions. *J. Mater. Chem. A* **2019**, 10.1039.C9TA05637H. https://doi.org/10.1039/C9TA05637H.

(101) Ohtani, B.; Iwai, K.; Nishimoto, S.; Sato, S. Role of Platinum Deposits on Titanium(IV) Oxide Particles: Structural and Kinetic Analyses of Photocatalytic Reaction in Aqueous Alcohol and Amino Acid Solutions. *J. Phys. Chem. B* **1997**, *101* (17), 3349–3359. https://doi.org/10.1021/jp962060q.

(102) Haselmann, G. M.; Eder, D. Early-Stage Deactivation of Platinum-Loaded TiO2 Using In Situ Photodeposition during Photocatalytic Hydrogen Evolution. *ACS Catal.* **2017**, *7* (7), 4668–4675. https://doi.org/10.1021/acscatal.7b00845.

(103) Rodríguez, J. L.; Valenzuela, M. A.; Pola, F.; Tiznado, H.; Poznyak, T. Photodeposition of Ni Nanoparticles on TiO2 and Their Application in the Catalytic Ozonation of 2,4-Dichlorophenoxyacetic Acid. *Journal of Molecular Catalysis A: Chemical* **2012**, *353–354*, 29–36. https://doi.org/10.1016/j.molcata.2011.11.001.

Acknowledgements

First and foremost, I would like to thank Prof. Dominik Eder for granting me the opportunity of working in his innovative and exciting research group. Especially, I would like to highlight the trust he placed in me, his fair handling and his attentiveness not only towards me, but towards all of the group's members. Out of our thrilling conversations and his undoubted creativity, fantastic ideas came to be, which enriched this work in a great matter.

Then, I would like to express my deepest gratitude to my direct supervisor, Dr. Alexey Cherevan. He guided me through the research, experimental and writing process in an exceptional way, always surpassing my expectations. The availability and engagement he offered me still astonish me and I couldn't be happier to have gotten the privilege of working under the wing of such a passionate scientist and great human being.

Special thanks go to the X-ray Physics Team at the Atominstitut. Prof. Peter Wobrauschek, Prof. Christina Streli and Dr. Peter Kregsamer made it possible for me to acquire key elemental analysis results with their fantastic TXRF instruments. I am much grateful for the time all of you took in organising my access to the facilities, giving me invaluable training and spreading your contagious enthusiasm whenever faced with challenging samples.

I would also like to thank the whole AK-Eder group for their willingness to help me in anything I needed. All of you made this last year a wonderful one for me. Especially, I would like to mention and thank Ariane Giesriegl, for her amazing TEM skills; Jasmin Schubert, for the XPS experiments and proof-reading of this Thesis; and Dr. Jia Wang, for everything.

My friends, near and far, should know I couldn't have done this without your constant caring and support throughout my life. I thank you all, from the bottom of my heart.

Finally, I would also like to thank my family for their unconditional love. Hanna and baby Mateo, who always brighten difficult days. My brothers, Diego and Rodrigo, whom I have always admired and continue to be my role models in uncountable ways. And most importantly, my dearest and loving parents, Rony Ayala and Mireya Leiva, to whom I dedicate this Thesis. Both of you are living examples of dedication and perseverance but also of kindness, love, good-will and fairness towards others. You are one of my greatest inspirations in life and I thank you for everything you have done and still do for me.

¡Gracias a todos!

Appendix

Table 3 | A summary of the prepared samples.

Sample name	Experimental procedure	Modifications	Post-treatment	Characterization performed	Other tests performed	HER-active	Interesting
PO_4/TiO_2	as prepared according to 5.1	Phosphate-modified TiO_2	-	IR, TXRF, DRS	HER	✓	Fluffy
5/Mn@TiO_2	as prepared according to 5.2	5 wt.% loading of Mn on TiO_2	-	DRS	HER	✗	-
5/Fe@TiO_2	as prepared according to 5.2	5 wt.% loading of Fe on TiO_2	-	DRS	HER	✗	Reddish
5/Co@TiO_2	as prepared according to 5.2	5 wt.% loading of Co on TiO_2	-	DRS	HER	✗	-
5/Ni@TiO_2	as prepared according to 5.2	5 wt.% loading of Ni on TiO_2	-	DRS, TXRF, TEM	HER	✓	-
5/Cu@TiO_2	as prepared according to 5.2	5 wt.% loading of Cu on TiO_2	-	DRS, TXRF, TEM	HER	✓	Greenish
5/Ag@TiO_2	as prepared according to 5.2	5 wt.% loading of Ag on TiO_2	-	DRS	HER	✗	-
5/Au@TiO_2	as prepared according to 5.2	5 wt.% loading of Au on TiO_2	-	DRS, TXRF	HER	✓	Purple
5/Pt@TiO_2	as prepared according to 5.2	5 wt.% loading of Pt on TiO_2	-	DRS, TXRF	HER	✓	Orange
0.5/Mn@TiO_2	as prepared according to 5.2	0.5 wt.% loading of Mn on TiO_2	-	-	HER	✗	-
0.5/Fe@TiO_2	as prepared according to 5.2	0.5 wt.% loading of Fe on TiO_2	-	-	HER	✗	Reddish
0.5/Co@TiO_2	as prepared according to 5.2	0.5 wt.% loading of Co on TiO_2	-	-	HER	✗	-
0.5/Ni@TiO_2	as prepared according to 5.2	0.5 wt.% loading of Ni on TiO_2	-	-	HER	✓	-
0.5/Cu@TiO_2	as prepared according to 5.2	0.5 wt.% loading of Cu on TiO_2	-	-	HER	✓	Greenish
0.5/Ag@TiO_2	as prepared according to 5.2	0.5 wt.% loading of Ag on TiO_2	-	-	HER	✗	-

Sample name	Experimental procedure	Modifications	Post-treatment	Characterization performed	Other tests performed	HER-active	Interesting
0.5/Au@TiO_2	as prepared according to 5.2	0.5 wt.% loading of Au on TiO_2	-	-	HER	✓	Purple
0.5/Pt@TiO_2	as prepared according to 5.2	0.5 wt.% loading of Pt on TiO_2	-	-	HER	✓	Orange
1/Ni@TiO_2	as prepared according to 5.2	1 wt.% loading of Ni on TiO_2	-	DRS, TXRF	HER	✓	-
0.2/Ni@TiO_2	as prepared according to 5.2	0.2 wt.% loading of Ni on TiO_2	-	DRS, TXRF	HER	✓	-
0.04/Ni@TiO_2	as prepared according to 5.2	0.04 wt.% loading of Ni on TiO_2	-	DRS, TXRF	HER	✓	-
0.008/Ni@TiO_2	as prepared according to 5.2	0.008 wt.% loading of Ni on TiO_2	-	DRS, TXRF	HER	✓	-
1/Cu@TiO_2	as prepared according to 5.2	1 wt.% loading of Cu on TiO_2	-	DRS, TXRF	HER	✓	Greenish
0.2/Cu@TiO_2	as prepared according to 5.2	0.2 wt.% loading of Cu on TiO_2	-	DRS, TXRF	HER	✓	Greenish
0.04/Cu@TiO_2	as prepared according to 5.2	0.04 wt.% loading of Cu on TiO_2	-	DRS, TXRF	HER	✓	Greenish
0.008/Cu@TiO_2	as prepared according to 5.2	0.008 wt.% loading of Cu on TiO_2	-	DRS, TXRF	HER	✓	Greenish
1/Au@TiO_2	as prepared according to 5.2	1 wt.% loading of Au on TiO_2	-	DRS, TXRF, TEM	HER	✓	Purple
0.2/Au@TiO_2	as prepared according to 5.2	0.2 wt.% loading of Au on TiO_2	-	DRS, TXRF	HER	✓	Purple
0.04/Au@TiO_2	as prepared according to 5.2	0.04 wt.% loading of Au on TiO_2	-	DRS, TXRF	HER	✓	Purple
0.008/Au@TiO_2	as prepared according to 5.2	0.008 wt.% loading of Au on TiO_2	-	DRS, TXRF	HER	✓	Purple
1/Pt@TiO_2	as prepared according to 5.2	1 wt.% loading of Pt on TiO_2	-	DRS, TXRF, TEM	HER	✓	Orange

Sample name	Experimental procedure	Modifications	Post-treatment	Characterization performed	Other tests performed	HER-active	Interesting
0.2/Pt@TiO_2	as prepared according to 5.2	0.2 wt.% loading of Pt on TiO_2	-	DRS, TXRF	HER	✓	Orange
0.04/Pt@TiO_2	as prepared according to 5.2	0.04 wt.% loading of Pt on TiO_2	-	DRS, TXRF	HER	✓	Orange
0.008/Pt@TiO_2	as prepared according to 5.2	0.008 wt.% loading of Pt on TiO_2	-	DRS, TXRF	HER	✓	Orange
5/Ni@PO_4/TiO_2	as prepared according to 5.2	5 wt.% loading of Ni on PO_4/TiO_2	-	TXRF	HER	✓	-
1/Ni@PO_4/TiO_2	as prepared according to 5.2	1 wt.% loading of Ni on PO_4/TiO_2	-	TXRF	HER	✓	-
0.2/Ni@PO_4/TiO_2	as prepared according to 5.2	0.2 wt.% loading of Ni on PO_4/TiO_2	-	TXRF	HER	✓	-
0.04/Ni@PO_4/TiO_2	as prepared according to 5.2	0.04 wt.% loading of Ni on PO_4/TiO_2	-	TXRF	HER	✓	-
0.008/Ni@PO_4/TiO_2	as prepared according to 5.2	0.008 wt.% loading of Ni on PO_4/TiO_2	-	TXRF	HER	✓	-
5/Cu@PO_4/TiO_2	as prepared according to 5.2	5 wt.% loading of Cu on PO_4/TiO_2	-	TXRF	HER	✓	Greenish
1/Cu@PO_4/TiO_2	as prepared according to 5.2	1 wt.% loading of Cu on PO_4/TiO_2	-	TXRF	HER	✓	Greenish
0.2/Cu@PO_4/TiO_2	as prepared according to 5.2	0.2 wt.% loading of Cu on PO_4/TiO_2	-	TXRF	HER	✓	Greenish
0.04/Cu@PO_4/TiO_2	as prepared according to 5.2	0.04 wt.% loading of Cu on PO_4/TiO_2	-	TXRF	HER	✓	Greenish
0.008/Cu@PO_4/TiO_2	as prepared according to 5.2	0.008 wt.% loading of Cu on PO_4/TiO_2	-	TXRF	HER	✓	Greenish
5/Au@PO_4/TiO_2	as prepared according to 5.2	5 wt.% loading of Au on PO_4/TiO_2	-	TXRF	HER	✓	Purple

Sample name	Experimental procedure	Modifications	Post-treatment	Characterization performed	Other tests performed	HER-active	Interesting
1/Au@PO_4/TiO_2	as prepared according to 5.2	1 wt.% loading of Au on PO_4/TiO_2	-	TXRF	HER	✓	Purple
0.2/Au@PO_4/TiO_2	as prepared according to 5.2	0.2 wt.% loading of Au on PO_4/TiO_2	-	TXRF	HER	✓	Purple
0.04/Au@PO_4/TiO_2	as prepared according to 5.2	0.04 wt.% loading of Au on PO_4/TiO_2	-	TXRF	HER	✓	Purple
0.008/Au@PO_4/TiO_2	as prepared according to 5.2	0.008 wt.% loading of Au on PO_4/TiO_2	-	TXRF	HER	✓	Purple
5/Pt@PO_4/TiO_2	as prepared according to 5.2	5 wt.% loading of Pt on PO_4/TiO_2	-	TXRF	HER	✓	Orange
1/Pt@PO_4/TiO_2	as prepared according to 5.2	1 wt.% loading of Pt on PO_4/TiO_2	-	TXRF	HER	✓	Orange
0.2/Pt@PO_4/TiO_2	as prepared according to 5.2	0.2 wt.% loading of Pt on PO_4/TiO_2	-	TXRF	HER	✓	Orange
0.04/Pt@PO_4/TiO_2	as prepared according to 5.2	0.04 wt.% loading of Pt on PO_4/TiO_2	-	TXRF	HER	✓	Orange
0.008/Pt@PO_4/TiO_2	as prepared according to 5.2	0.008 wt.% loading of Pt on PO_4/TiO_2	-	TXRF	HER	✓	Orange
0.2/Ni@TiO_2/250	as prepared according to 5.2, modification according to 5.3	0.2 wt.% loading of Ni on TiO_2	Heated up to 250 °C for 3 h	-	HER	✓, no change from normal	-
0.008/Cu@TiO_2/250	as prepared according to 5.2, modification according to 5.3	0.008 wt.% loading of Cu on TiO_2	Heated up to 250 °C for 3 h	-	HER	✓, no change from normal	-
0.008/Au@TiO_2/250	as prepared according to 5.2, modification according to 5.3	0.008 wt.% loading of Au on TiO_2	Heated up to 250 °C for 3 h	-	HER	✓, no change from normal	-

Sample name	Experimental procedure	Modifications	Post-treatment	Characterization performed	Other tests performed	HER-active	Interesting
0.008/Pt@TiO_2/250	as prepared according to 5.2, modification according to 5.3	0.008 wt.% loading of Pt on TiO_2	Heated up to 250 °C for 3 h	-	HER	✓, no change from normal	-
1/Ni@TiO_2/dark	as prepared according to 5.4	1 wt.% loading of Ni on TiO_2	-	TXRF, DRS	HER	✓	-
1/Cu@TiO_2/dark	as prepared according to 5.4	1 wt.% loading of Cu on TiO_2	-	TXRF, DRS	HER	✓	Greenish
1/Au@TiO_2/dark	as prepared according to 5.4	1 wt.% loading of Au on TiO_2	-	TXRF, DRS, TEM	HER	✓	Purple
0.2/Au@TiO_2/dark	as prepared according to 5.4	0.2 wt.% loading of Au on TiO_2	-	TXRF, DRS	HER	✓	Purple
1/Pt@TiO_2/dark	as prepared according to 5.4	1 wt.% loading of Pt on TiO_2	-	TXRF, DRS	HER	✓	Orange
0.2/Pt@TiO_2/dark	as prepared according to 5.4	0.2 wt.% loading of Pt on TiO_2	-	TXRF, DRS	HER	✓	Orange
1/Ni@TiO_2/PD	as prepared according to 5.5	1 wt.% loading of Ni on TiO_2	-	-	HER	✓	Grey after HER
1/Cu@TiO_2/PD	as prepared according to 5.5	1 wt.% loading of Cu on TiO_2	-	-	HER	✓	Greenish after HER
1/Au@TiO_2/PD	as prepared according to 5.5	1 wt.% loading of Au on TiO_2	-	DRS, TEM	HER	✓	Purple after HER
0.2/Au@TiO_2/PD	as prepared according to 5.5	0.2 wt.% loading of Au on TiO_2	-	DRS	HER	✓	Purple after HER
0.04/Au@TiO_2/PD	as prepared according to 5.5	0.04 wt.% loading of Au on TiO_2	-	DRS	HER	✓	Purple after HER
1/Pt@TiO_2/PD	as prepared according to 5.5	1 wt.% loading of Pt on TiO_2	-	DRS	HER	✓	Grey after HER
0.2/Pt@TiO_2/PD	as prepared according to 5.5	0.2 wt.% loading of Pt on TiO_2	-	TEM	HER	✓	Grey after HER
0.04/Pt@TiO_2/PD	as prepared according to 5.5	0.04 wt.% loading of Pt on TiO_2	-	-	HER	✓	Grey after HER

Appendix | Exemplary TXRF spectra

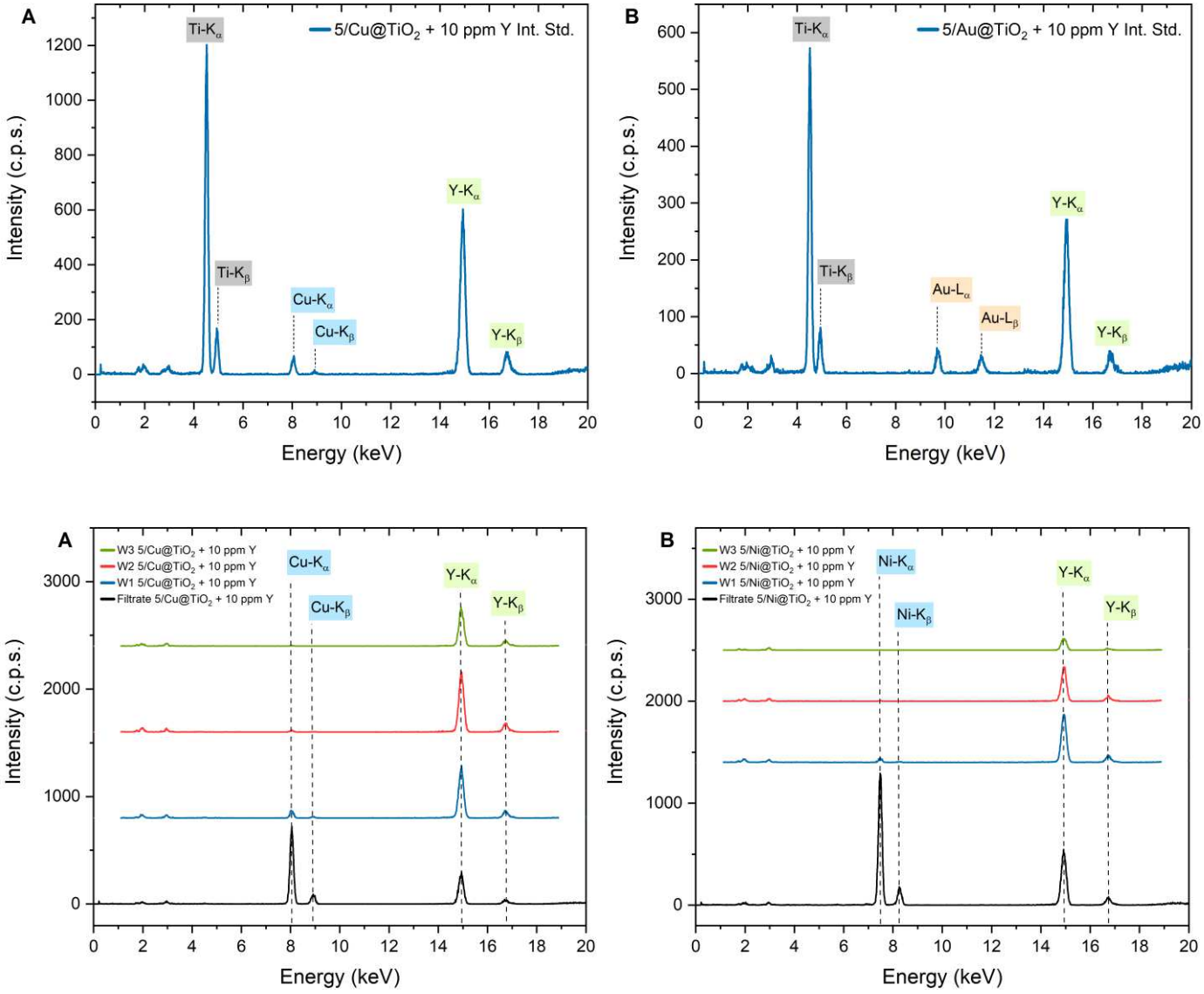

Exemplary TXRF spectra composite materials in the solid phase | Excitation conditions: Rh(Kα), at V = 50 kV and I = 0.7 mA, t = 200s. Addition of 10 ppm Y internal standard for quantification. **A**, 5/Cu@TiO_2 showing characteristic K-lines of Ti, Cu and Y. **B**, 5/Au@TiO_2 showing characteristic K-lines of Ti, Y and L-lines of Au.

Exemplary TXRF spectra for liquid phase | Excitation conditions: Rh(Kα), at V = 50 kV and I = 0.7 mA, t = 200s. Addition of 10 ppm Y internal standard for quantification. **A**, Filtrate and washing solutions (WX) of the impregnation process for 5/Cu@TiO_2. **B**, Filtrate and washing solutions (WX) of the impregnation process for 5/Ni@TiO_2. Intensities for the metal of interest decrease with every washing step.

Appendix | Additional DRS spectra

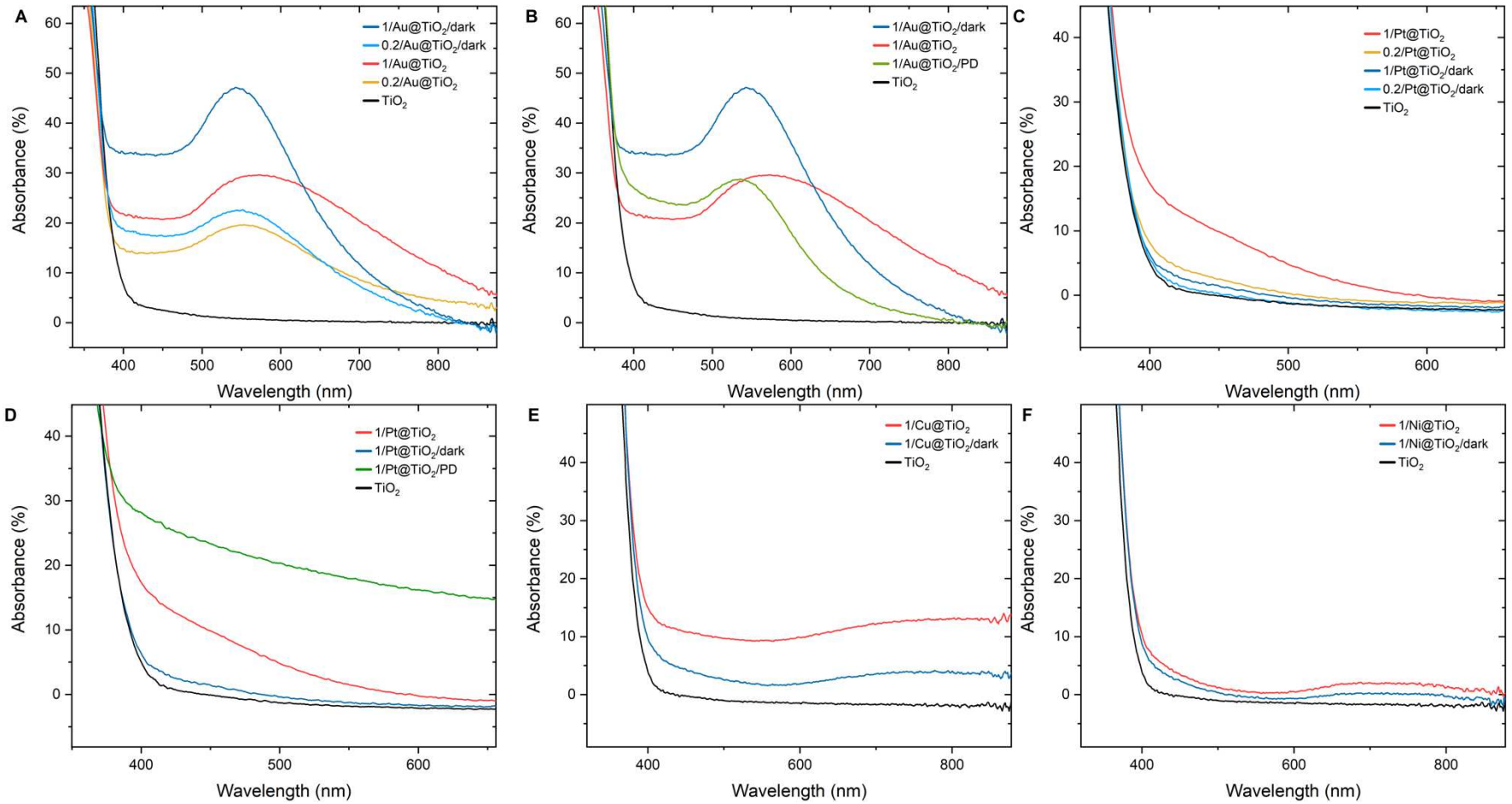

Comparison of different DRS spectra | **A**, Au/dark shows different spectra compared to normal synthesis. NP sizes from theoretical calculations result in d = 4-5 nm. **B**, Au/normal, Au/dark and Au/PD. Theoretical size of Au/PD also 4 nm. **C**, Pt/dark showing very little absorbance vs. Pt/normal due to lower loadings of co-catalyst. **D**, Pt/PD showing increased absorption in the visible range, due to NP-formation. **E**, Cu/dark showing very little absorbance vs. Cu/normal due to lower loadings of co-catalyst. **F**, Ni/dark showing very little absorbance vs. Ni/normal due to lower loadings of co-catalyst.

Appendix | Additional TEM images

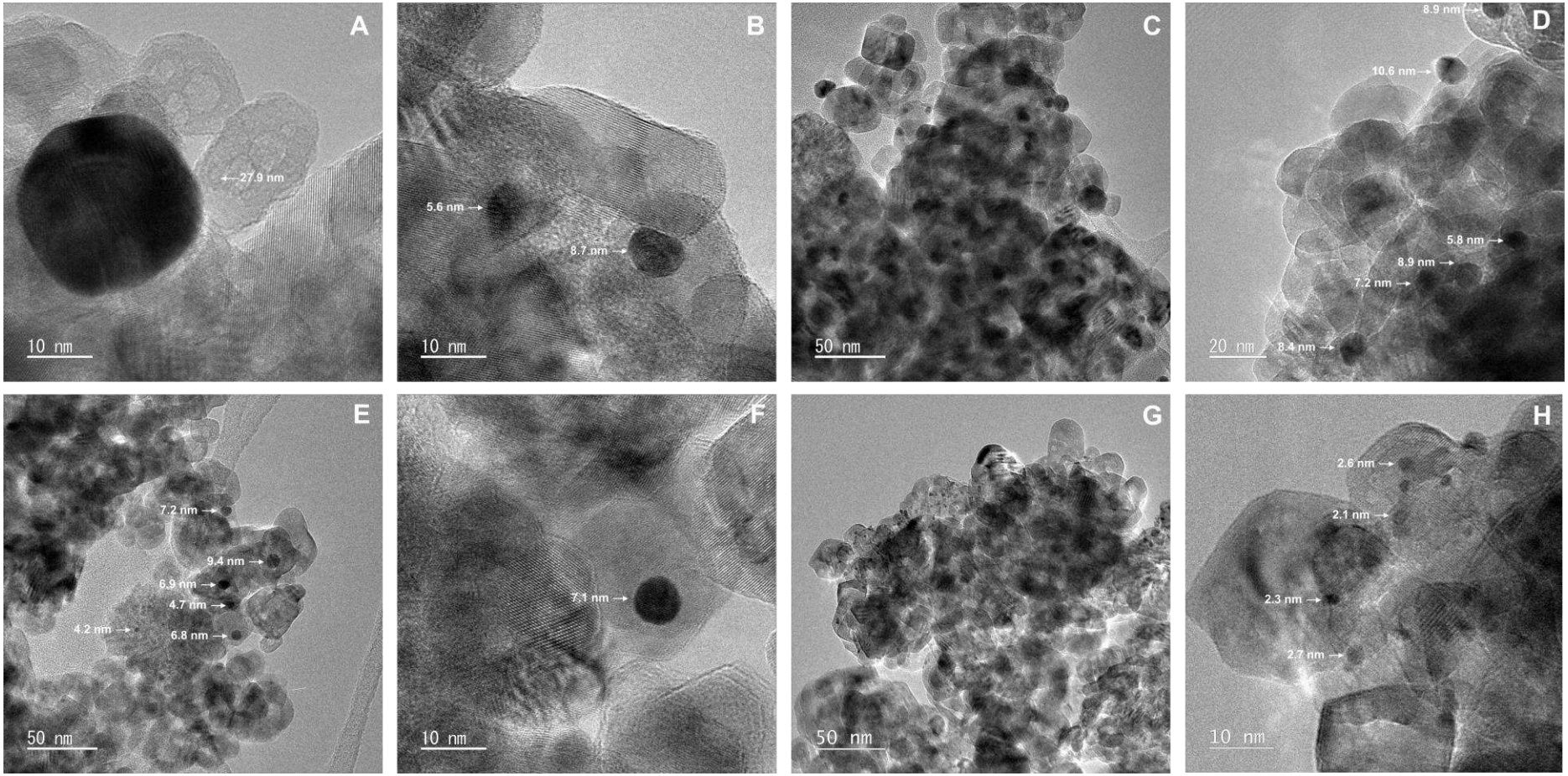

Additional TEM images | **A**, **B**, 1/Au@TiO_2 showing major differences in the size distribution. **C**, **D**, 1/Au@TiO_2/PD at different magnifications, sizes of Au NP between 5 and 11 nm. **E**, **F**, 1/Au@TiO_2/dark at different magnifications, sizes of Au NP between 4 and 10 nm. **G**, **H**, 0.2/Pt@TiO2/PD at different magnifications, sizes of Pt NP between 2 and 3 nm.

Appendix | Model Calculations

The mathematical reasoning behind **Model 1** are the following: The H_2 evolution rate is directly proportional to the surface atoms of the co-catalyst NPs that are involved in the catalytical reaction. Decreasing the co-catalyst's loading without changing the size/shape of the NPs results in a linear decrease of the number of particles, i.e. a linear decrease of the surface atoms and therefore a linear dependency ($y = x$) of the loading vs. the HER.

If: $$H_2\ evolution\ rate \sim surface$$

and: $$surface \sim co\text{-}catalyst\ loading$$

then: $$H_2\ evolution\ rate \sim co\text{-}catalyst\ loading$$

The turnover frequency, defined as:

$$TOF = \frac{H_2\ evolution\ rate}{co\text{-}catalyst\ moles}$$

will be a constant, since:

$$H_2\ evolution\ rate \sim co\text{-}catalyst\ loading$$

Subsequently, the HER will be divided by the loading, hence

$$TOF\ =\ constant$$

As an example, arbitrary initial values will be taken for showing the behavior of **Model 1** graphically: a loading of 5 wt.% (supposing it is 1000 µmol atoms at the surface of the particle that are catalytically involved in the reaction) would give an activity of 500 µmolh^{-1}.

Decreasing the loading by a factor of 5 would result in a decreased number of surface atoms involved in the HER (black) by the same factor. Since the size/morphology of the co-catalyst particle stays unchanged, but its number gets reduced (linear decrease of surface atoms with the loading). This means for 1 wt.% (200 µmol) the H_2 evolution rate will also decrease by a factor of 5, i.e. 100 µmol h^{-1}. The TOF (red), in this case, is a constant, since:

$$TOF = \frac{H_2\ evolution\ rate}{co\text{-}catalyst\ moles} = \frac{500\ \mu mol\ h^{-1}}{1000\ \mu mol} = \frac{100\ \mu mol\ h^{-1}}{200\ \mu mol} = 0.5\ h^{-1}$$

The same reasoning applies when going towards lower loadings.

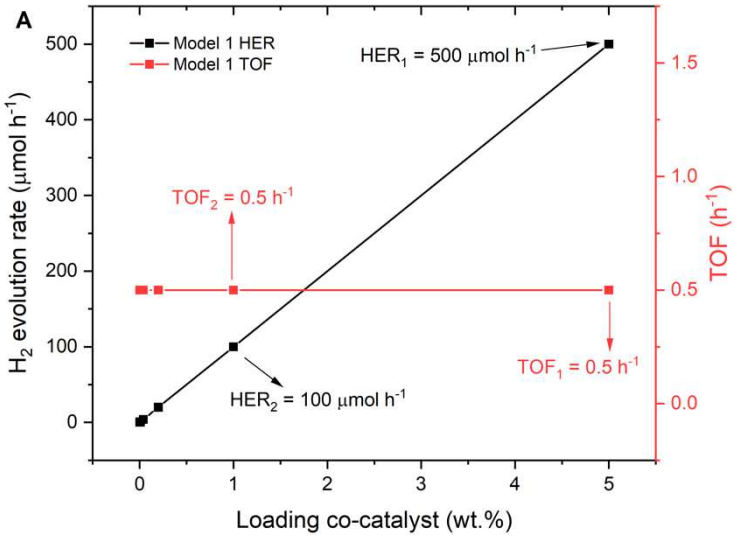

Graphical representation of Model 1 | Loading vs. HER (black slope, $y = x$) and loading vs. TOF (red constant, $y = a$)

In the case of **Model 2**, we assume that the size/morphology of the co-catalyst NPs changes. The surface (S) and volume (V) of a sphere with a radius (r) are:

$$S = 4\,\pi\,r^2 \quad \text{and} \quad V = \frac{4}{3}\,\pi\,r^3$$

Setting S as a function of V (i.e. loading) and substituting r results in the following equation:

$$S_{(V)} = 4\pi \left(\frac{3V}{4\pi}\right)^{2/3}$$

Upon simplifying we obtain:

$$S_{(V)} = \left(6\sqrt{\pi}\,V\right)^{2/3} \quad \rightarrow \quad S_{(V)} \sim V^{2/3}$$

Since

$$HER \sim S \quad \text{and} \quad loading \sim V$$

then, the same relation as for S and V follows for HER and $Loading$:

$$H_2\ evolution\ rate \sim loading^{2/3}$$

The TOF, as a function of the loading follows a different proportionality due to its definition:

$$TOF = \frac{H_2\ evolution\ rate}{co\text{-}catalyst\ moles} \sim \frac{loading^{2/3}}{loading} \sim \frac{1}{loading^{1/3}}$$

$$\rightarrow \quad TOF \sim loading^{-1/3}$$

For example: assuming a sample with 5 wt.% (1000 µmol atoms) and an initial HER_1 value of 100 µmolh^{-1}. A decrease by a factor 5 in the loading would then have a decrease in the HER by a factor of $(x)^{2/3}$, i.e. we expect that 1 wt.% (200 µmol atoms) would render a HER_2 of

$$HER_2 = 100\ \mu molh^{-1} \div (5)^{2/3} = 34.2\ \mu mol\ h^{-1}$$

The TOF, in turn, would follow the proportionality of $(x)^{-1/3}$. Differently to **Model 1**, where the TOF was a constant, in the case of **Model 2** we observe an increase of the TOF with decreasing loadings:

$$TOF_1 = \frac{100\ \mu mol\ h^{-1}}{1000\ \mu mol} = 0.10\ h^{-1} \neq TOF_2 = \frac{34.2\ \mu mol\ h^{-1}}{200\ \mu mol} = 0.17\ h^{-1}$$

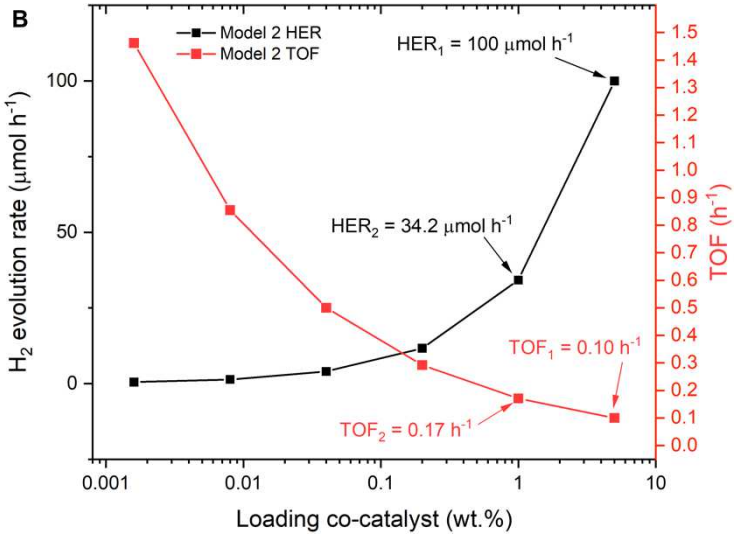

Graphical representation of Model 2 | Loading vs. HER (black line, $y = x^{2/3}$) and loading vs. TOF (red line, $y = x^{-1/3}$)